NTNU – Trondheim
Norwegian University of
Science and Technology

Comparison of numerical schemes for nonlinear 1-D arterial blood flow modeling

Fredrik Eikeland Fossan

Mechanical Engineering
Submission date: June 2015
Supervisor: Leif Rune Hellevik, KT

Norwegian University of Science and Technology
Department of Structural Engineering

Department of Structural Engineering
Faculty of Engineering Science and Technology
NTNU- Norwegian University of Science and Technology

ACCESSIBILITY

Open

MASTER THESIS 2015

SUBJECT AREA: Biomechanics	DATE: 9/6/15	NO. OF PAGES: 71 + 34

TITLE:

Comparison of numerical schemes for nonlinear 1-D arterial Blood flow modeling

City: Trondheim

Fredrik Eikeland Fossan

SUMMARY:

In this Thesis, the numerical methods used in STARFiSh (MacCormack or McC) have been tested and compared with five other state of the art flow-solvers: discontinuous Galerkin (DCG), locally conservative Galerkin (LCG), Galerkin least-squares finite element method (FEM), finite volume method (FVM), and a simplified trapezium rule method (STM). Comparisons are made in a series of six benchmark test cases with an increasing degree of complexity. The tests revealed limitations in the original implementation of STARFiSh. The original MacCormack scheme was not implemented correctly, which resulted in discontinuities between boundary and field nodes. The scheme also proved to be non-conservative in cases with big relative weight on the convective term. The original linear bifurcation model gave rise to discrepancies in networks with big changes in dynamic pressure. As a result a new conservative solving scheme, and a new bifurcation model was implemented. The implementations have been validated in the comparison with the five other flow solvers, and in additional cases where analytical solutions exist.

The thesis has evolved around a joint project to form the article "Comparison1D-scheme". The tests, results and findings have been conducted to contribute with STARFiSh's part of the article. The accuracy of the numerical schemes is assessed by comparison against theoretical results, 3-D data in compatible domains with distensible walls, or experimental data in a network of silicone tubes. Results show a good agreement among all numerical schemes and their ability to capture the main features of pressure, flow and area waveforms in large arteries.

Grid tests show that for the physiological cases where the wave length is long comparing with each vessel segment, low CFL numbers can be tolerated without introduction of significant diffusive and dispersive errors for STARFiSh solutions.

A model which integrates Womersley theory for pulsatile pipe flow with One-dimensional (1-D) compliant vessel flow, have been established. The solutions using Womersley theory for estimating the velocity profile, and it's subsequent effect on convective- and friction term have been compared with solutions using an assumed velocity profile. The solution using Womersley theory did not yield better results comparing with 3-D numerical data, in a single vessel test replicating blood flow in the upper thoracic aorta.

SUPERVISOR: Leif Rune Hellevik

CARRIED OUT AT: NTNU

Declaration of Authorship

Hereby I certify that the thesis I am submitting is my personal work, or that performed as a part of the joint project "Comparison1-DScheme", except where otherwise indicated. I am aware of the University's regulations concerning plagiarism and the related disciplinary actions. The use of the works of other authors, in any form, is properly acknowledged at their point of use.

Name:

Signature:

Date:

Assignment

One-dimensional models are currently the models of choice for the investigation of wave phenomena in the arterial tree. STARFiSh, which stands for STochastic ARterial Flow Simulations, is a code that is currently in development at the Norwegian University of Science and Technology (NTNU) and uses 1-D models of the arterial tree.
This thesis has been focused around a joint project with five other groups to form the article "Comparison of numerical schemes for nonlinear 1-D arterial blood flow modeling". The assignment was suggested by Prof. Leif Rune Hellevik, as he was invited to join the project. The comparison of STARFiSh with five other state of the art flow solvers formed a fine arena for checking the current state of STARFiSh.

Suggested topics for the thesis are:

- Perform the test cases suggested in the article
- Compare with the other solvers
- Do appropriate changes in implementations
- rerun tests
- write MacCormacks contributions to the article
- Validation of new implementations

Optional topics could then be:

- Womersleytheory

Preface

"Every Problem is an opportunity in disguise." Benjamin Franklin

This thesis is the result of the research project, which concludes my studies towards the M. Sc. degree in Mechanical Engineering at NTNU in Trondheim.

The research project leading to this thesis was carried out in the Division of Biomechanics at Norwegian University of Science and Technology in Trondheim. The thesis builds up on the STARFiSh (Stochastic Arterial Flow Simulations) code, which was previously developed at NTNU with contributions of Paul Roger Leinan, Vinzenz Gregor Eck, Knut Petter Maråk, Yvan Gugler and Professor Leif Rune Hellevik. The subject of this thesis is a comparison of the numerical methods used to solve the equations that govern 1-D pressure and flow propagation. It has evolved around a joint project with five other state of the art solvers. However as it turned out, there were some limitations in the current implementations of STARFiSh. This Thesis has been a dynamic process of setting up tests, comparing, doing mistakes, finding promblems and fixing them.

I would like to point out that parts of this Thesis have been adapted more or less directly from the article "Comparison1Dscheme". As a CoAuthor I have taken this liberty. Where plural form is used (we), refers to work performed by the group that make out the authors of the article. Elsewhere singular form have been used (I).

The application of engineering science to human physiology and medicine might not be an obvious topic to many people. The same was true for me. The fourth year of my studies was carried out on exchange in Vancouver, Canada. Here I attended a very interesting course on the "Fundamentals of Injury Biomechanics." This was indeed what made me contact the Division of Biomechanics at Norwegian University of Science and Technology in Trondheim. Hopefully the research conducted here at NTNU, and in collaboration with the other participants of "Comparison1D-scheme" will result in better understanding of the hemodynamics system. Ideally it will one day form the basis for diagnostic tools and treat illness associated with the hemodynamics system.

Abstract

In this Thesis, the numerical methods used in STARFiSh (MacCormack or McC) have been tested and compared with five other state of the art flow-solvers: discontinuous Galerkin (DCG), locally conservative Galerkin (LCG), Galerkin least-squares finite element method (FEM), finite volume method (FVM), and a simplified trapezium rule method (STM). Comparisons are made in a series of six benchmark test cases with an increasing degree of complexity. The tests revealed limitations in the original implementation of STARFiSh. The original MacCormack scheme was not implemented correctly, which resulted in discontinuities between boundary and field nodes. The scheme also proved to be non-conservative in cases with big relative weight on the convective term. The original linear bifurcation model gave rise to discrepancies in networks with big changes in dynamic pressure. As a result a new conservative solving scheme, and a new bifurcation model was implemented. The implementations have been validated in the comparison with the five other flow solvers, and in additional cases where analytical solutions exist.

The thesis has evolved around a joint project to form the article "Comparison1D-scheme". The tests, results and findings have been conducted to contribute with STARFiSh's part of the article. The accuracy of the numerical schemes is assessed by comparison against theoretical results, 3-D numerical data in compatible domains with distensible walls, or experimental data in a network of silicone tubes. Results show a good agreement among all numerical schemes and their ability to capture the main features of pressure, flow and area waveforms in large arteries.

Grid tests show that for the physiological cases where the wave length is long comparing with each vessel segment, low CFL numbers can be tolerated without introduction of significant diffusive and dispersive errors for STARFiSh solutions.

A model which integrates Womersley theory for pulsatile pipe flow with One-dimensional (1-D) compliant vessel flow have been established. The solutions using Womersley theory for estimating the velocity profile, and it's subsequent effect on convective- and friction term have been compared with solutions using an assumed velocity profile. The solution using Womersley theory did not yield better results comparing with 3-D numerical data in a single vessel test replicating blood flow in the upper thoracic aorta.

Keywords: 1-D wave propagation model, STARFiSh, Conservative, Non-Conservative, 1-D Numerical Schemes, Benchmark Tests Cases, Womersley Theory.

Sammendrag

I denne oppgaven har de numeriske metodene brukt i STARFiSh (MacCormack eller McC), blitt testet og sammenlignet med fem andre metoder for løsning av blodstrøm og blodtrykk: diskontinuerlig Galerkin (DCG), lokalt konservative Galerkin (LCG), Galerkin minste kvadrats element metode (FEM), endelig-volum metode (FVM), og en forenklet trapesium metode (STM). Sammenligningen er utført i seks tester med gradvis økning av kompleksitet. Testene avslørte noen feil og begrensninger i den originale implementeringen av STARFiSh. MacCormack skjemat inneholdt en implementeringsfeil, noe som gav opphav til diskontinuitet mellom løsning av grense- og felt-noder. I tillegg viste skjemaet seg å være ikke-konservativt i tester med stor relativ vekt på det konvektive leddet. Den originale metoden for løsning av link og bifurkasjoner introduserte avvik i tester med store endringer i dynamisk trykk. Dette resulterte i implementering av ett nytt konservativt skjema for løsning av felt-noder, samt en ny bifurkasjonsmodell. De nye implementeringene har blitt validert i sammenligning med de andre numeriske skjemaene, samt i ytterligere tester hvor analytisk løsning finnes.
Oppgaven er utført med utgangspunkt i samarbeidsprosjektet om å publisere artikkelen "Comparsion1Dscheme". Testene, resultatene og nye implementeringer har blitt utført for å levere best mulig resultater som STARFiSh sitt bidrag. Nøyaktigheten til de numeriske metodene har blitt bestemt i sammenligning med teoretisk løsning, 3-Dnumerisk data med kompatibel geometri, grensebetingelser og vegg-modell, samt eksperimentelle data fra nettverk med silikonrør. Resultatene viser veldig godt samsvar mellom alle numeriske metoder, og deres evne til å modellere blodtrykk og blodstrøm.
For fysiologiske tilfeller, med tilhørende lange bølgelengder, viser tester at lave CFL tall kan tolereres uten å introdusere betydelige feil (amplitude og fase) for STARFiSh.
En modell som knytter sammen Womersley teori for oscillerende strømning i rør med Endimensjonal (1-D) blodstrømning i bevegelige rør har blitt etablert. Løsninger med Womersley teori for estimering av hastighetsprofil og dens anvendelse på konvektivt- og friksjonsledd har blitt sammenlignet med løsning basert på antatt hastighetsprofil. Løsning med Womersley teori gav ikke bedre løsning sammenlignet med 3-D data i en test som simulerer blodstrømning i aorta.

Keywords: 1-D wave propagation model, STARFiSh, Conservative, Non-Conservative, 1-D Numerical Schemes, Benchmark Tests Cases, Womersley Theory.

Acknowledgments

I would like to thank professor Leif Rune Hellevik at NTNU for supervising my thesis and for letting me take part in the project Comparison1Dscheme. I am grateful for all meetings and guidance through my Thesis.
Many thanks go to Vinzenz Gregor Eck and Jacob Sturdy, Phd students in the Division of Biomechanics, for their willingness to answer my questions and to discuss new ideas, which I appreciated very much.
I would also like to thank Yvan Gugler, fellow student in the Division of Biomechanics, for the exchange of ideas and the nice working atmosphere.
Finally, I would like to thank all the fellow participants in the project Comparison1Dscheme. A special thanks go to Jordi Alastruey-Arimon for leading the project, guidance and questions answered throughout this project.

Table of contents

1 Introduction **1**

2 Methods **3**
2.1 Governing equations . . . 3
2.1.1 A,Q system . . . 3
2.1.2 A,U system . . . 4
2.1.3 Closing the system; Constitutive equation . . . 4
2.1.4 P,Q system . . . 5
2.2 Characteristic variables and their relation with the state variables . . . 6
2.2.1 A,U system . . . 6
2.2.2 P,Q system . . . 7
2.3 Womersley Theory . . . 8

3 Numerical solution **9**
3.1 Discontinuous Galerkin (DG) scheme . . . 9
3.2 Locally conservative Galerkin (LCG) scheme . . . 9
3.3 Finite Volume (FV) scheme . . . 9
3.4 Galerkin Least-Squares Finite Element (FE) scheme . . . 10
3.5 MacCormack (McC) scheme . . . 10
3.5.1 Derivation of the MacCormack scheme for a general hyperbolic system . . . 10
3.5.2 Application on 1D-system . . . 11
3.6 Simplified Trapezium Rule Method (STM) . . . 12
3.7 Boundary conditions . . . 12
3.7.1 Inflow boundary condition . . . 12
3.7.2 Junction matching conditions . . . 13
3.7.3 Terminal boundary conditions . . . 15
3.8 Error calculations . . . 16

4 Tests **17**
4.1 Propagation of a single pulse in a straight vessel . . . 17
4.2 CCA . . . 17
4.3 ThoA . . . 18
4.4 AoBif . . . 19
4.5 Benchmark (in vitro) . . . 20
4.6 Benchmark (ADAN55 model) . . . 21
4.7 Steady Flow in a single vessel with narrowing in the middle . . . 22
4.8 Constant Flow in symmetric and asymmetric single-bifurcation . . . 23

5 Process **25**

6 Grid-adaption **27**
6.1 Propagation of a single pulse in a straight vessel . . . 27
6.2 CCA . . . 27
6.3 ThoA . . . 29
6.4 AoBif . . . 29
6.5 Benchmark . . . 30
6.6 Adan55 . . . 30

7 Results: STARFiSh and Womersley **35**
7.1 STARFiSh . . . 35
7.1.1 Propagation of a single pulse in a straight vessel . . . 35
7.1.2 CCA . . . 36
7.1.3 ThoA . . . 38
7.1.4 AoBif . . . 40
7.1.5 Benchmark (in vitro) . . . 41
7.1.6 Benchmark (ADAN55 model) . . . 42
7.1.7 Steady Flow in a single vessel with narrowing in the middle . . . 46
7.1.8 Constant Flow in symmetric and asymmetric single-bifurcation . . . 47
7.2 Womersley . . . 50

8 Discussion **55**
8.1 STARFiSh . . . 55
8.1.1 SingleVesselPulse . . . 55
8.1.2 CCA, AoBif, BenchMark . . . 55
8.1.3 ThoA . . . 56
8.1.4 Adan55 . . . 56
8.1.5 Steady Flow in a single vessel with narrowing in the middle . . . 58
8.1.6 Constant Flow in symmetric and asymmetric single-bifurcation . . . 59
8.1.7 Methods used in STARFiSh's contribution to Comparison1D-scheme . . . 59
8.2 Womersley . . . 59
8.3 Future work . . . 60

9 Results Comparison1Dscheme **63**
9.1 Single pulse propagation in a straight reflection-free vessel . . . 63
9.2 Common carotid artery . . . 63
9.3 Upper thoracic aorta . . . 64
9.4 Aortic bifurcation . . . 64
9.5 Benchmark (in vitro) . . . 64
9.6 ADAN55 model . . . 64

10 Discussion Comparison1Dscheme **67**
10.1 Single pulse model . . . 67
10.2 Physiological single artery models . . . 68
10.3 Physiological network models . . . 68

11 Conclusions **71**

A Tests **i**
A.1 Benchmark (in vitro) . . . i
A.2 Benchmark (ADAN55 model) . . . ii

B Grid-adaption **v**
B.0.1 CCA, ThoA and AoBif . . . v

C Results STARFiSh **x**
C.1 AoBif . . . x
C.2 Benchmark test . . . xi

D Comparison1Dscheme **xvi**
D.1 tables xvi
D.2 figures xx

E Additional mathematics **xxxiii**
E.1 Analytical solution for steady flow through Bifurcation with Resistance BC . . . xxxiii

List of Figures

1 Moveable Control Volume. . . . 3
2 Compliant vessel . . . 7
3 Topology of Benchmark (in vitro) model . . . 20
4 Topology of ADAN55 model . . . 21
5 Geometry of long vessel with narrowing in midsection . . . 22
6 Geometry of the symmetric bifurcation with constant flow . . . 24
7 Geometry of the asymmetric bifurcation with constant flow . . . 24
8 Effect of changing CFL number in single-pulse model . . . 28
9 Oscillations due to very low CFL number in Thoracic aorta . . . 29
10 Griddepence shown in Pressure contours in aortic segments of ADAN55 model . 32
11 Effect of using discontinous compliance law in ADAN55 model . . . 33
12 Effect of an implementation error in McC scheme, in single-pulse model . . . 35
13 Comparison of Matrix- and Flux- McC scheme in single-pulse model . . . 36
14 Comparison of Matrix- and Flux- McC scheme in Common carotid artery . . . 37
15 Comparison of Matrix- and Flux- McC scheme in the upper thoracic aorta . . . 38
16 Comparison of Matrix- and Flux- McC scheme in the aortic bifurcation . . . 40
17 Comparison of McC schemes and bifurcation models in ADAN55 model (Aortic segments) . . . 43
18 Comparison of McC schemes and bifurcation models in ADAN55 model (fourth generation vessels) . . . 44
19 Comparison of McC schemes and bifurcation models in ADAN55 model (Pressure contours aorta) . . . 45
20 Comparison of McC schemes and bifurcation models in long vessel with narrowing in midsection . . . 47
21 validation of bifurcation model with analytical solution in symmetric bifurcation 49
22 validation of bifurcation model with analytical solution in asymmetric bifurcation 49
23 Electrical equivalent to bifurcation with distal Resistance and constant flow . . . 50
24 Comparison of Womersley solution and assumed velocity profile solution in thoracic aorta . . . 51
25 Validation of Womersley model with check of Flow . . . 52
26 Comparison of Convective term using Womersley theory and assumed profile . . 53
27 Comparison of friction term using Womersley theory and assumed profile . . . 53
28 Comparison of Womersley and assumed velocity profiles . . . 54
29 Forward/Backward vs Backward/Forward . . . 58
30 STARFiSh results, Benchmark test, aortic segments . . . xii
31 STARFiSh results, Benchmark test, first generation of bifurcations . . . xiii
32 STARFiSh results, Benchmark test, second generation of bifurcations . . . xiv
33 STARFiSh results, Benchmark test, third generation of bifurcations . . . xv
34 Comparison1Dscheme, Single Pulse . . . xx
35 Comparison1Dscheme, CCA . . . xxi
36 Comparison1Dscheme, ThoA . . . xxii
37 Comparison1Dscheme, AoBif . . . xxiii
38 Comparison1Dscheme, 37-artery, Aortic segments . . . xxiv
39 Comparison1Dscheme, 37-artery, First generation segments . . . xxv
40 Comparison1Dscheme, 37-artery, Second generation segments . . . xxvi
41 Comparison1Dscheme, 37-artery, Third generation segments . . . xxvii

42 Comparison1Dscheme, ADAN55, Aortic segments xxviii
43 Comparison1Dscheme, ADAN55, first generation of bifurcations xxix
44 Comparison1Dscheme, ADAN55, second generation of bifurcations xxx
45 Comparison1Dscheme, ADAN55, third generation of bifurcations xxxi
46 Comparison1Dscheme, ADAN55, pressure contours xxxii
47 Comparison1Dscheme, ADAN55, Systolic, mean and diastolic pressure along the aorta. xxxiii

List of Tables

1 Parameters of the single-pulse model . . . 17
2 Model parameters of the common carotid artery . . . 18
3 Model parameters of the upper thoracic aorta . . . 18
4 Model parameters of the human aortic bifurcation . . . 19
5 General model parameters of the benchmark model . . . 20
6 General model parameters of the ADAN55 model . . . 21
7 Model parameters of long vessel with narrowing in midsection . . . 22
8 Model parameters of the symmetric bifurcation with constant flow . . . 23
9 Model parameters of the asymmetric bifurcation with constant flow . . . 23
10 Gridadaption Adan 55 Numeical parameters . . . 31
11 Error metrics of Matrix- and Flux- McC scheme in the common carotid artery . 39
12 Error metrics of Matrix- and Flux- McC scheme in the common carotid artery . 39
13 Error metrics of Matrix- and Flux- McC scheme in the aortic bifurcation (Junction) 41
14 Numerical parameters used for STARFiSh in ADAN55-tests . . . 42
15 validation of bifurcation model with analytical solution in symmetric bifurcation 48
16 validation of bifurcation model with analytical solution in asymmetric bifurcation 50
17 error metrics of Womersley solution and assumed velocity profile solution in thoracic aorta . . . 52
18 Parameters Benchmark test . . . ii
19 Full table of Parameter for the ADAN55 model . . . iii
20 Continuation of Full table of Parameter for the ADAN55 model . . . iv
21 Grid-adaption CCA . . . v
22 Grid-adaption CCA . . . vi
23 Grid-adaption CCA . . . vi
24 Grid-adaption ThoA . . . vii
25 Grid-adaption ThoA . . . vii
26 Grid-adaption ThoA . . . viii
27 Grid-adaption AoBif . . . viii
28 Grid-adaption AoBif . . . ix
29 Grid-adaption AoBif . . . ix
30 Error metrics of Matrix- and Flux- McC scheme in the aortic bifurcation (Aortamid) . . . x
31 Error metrics of Matrix- and Flux- McC scheme in the aortic bifurcation (Iliacamid) x
32 STARFiSh results, errormetrics Benchmark test . . . xi
33 Numerical Parameters Comparison1Dscheme . . . xvi
34 Comparison1Dscheme, CCA errors . . . xvii
35 Comparison1Dscheme, ThoA errors . . . xvii
36 Comparison1Dscheme, AoBif errors . . . xviii
37 Comparison1Dscheme, 37-artery errors . . . xix

Abbreviations

NTNU
Norwegian University of Science and Technology

Comparison1Dscheme
Comparison of Numerical schemes for nonlinear 1-D arterial blood flow modeling (article)

STARFiSh
Stochastic Arterial Flow Simulations

DG
Discontinuous Galerkin

LCG
locally conservative Galerkin

FEM
Galerkin least-squares finite element method

FVM
finite volume method

McC
MacCormack

STM
simplified trapezium rule method

CCA
Common Carotid Artery

ThoA
Thoracic Aorta

AoBif
Aortic Bifurcation

RHS
Right hand side

LHS
Left hand side

FFT
Fast Fourier transform

RMS
Root mean square

Nomenclature

Symbol	Definition
A	Cross-sectional area
P	Pressure
C	Area compliance
Q	Volumetric flow rate
U	Mean blood flow velocity
x	Longitudinal coordinate of blood vessel
z	Longitudinal coordinate of blood vessel
t	Time
T	Period of one heart cycle
$v(x, r, t)$	Blood flow velocity
$u(x, r, t)$	Blood flow velocity
τ_w	Wall shear stress
f	Friction forces
ρ	Blood density
L	Lenght of vessel
r	Vessel radius
r_d	Diastolic radius
ξ	Radial coordinate
ζ	Polynomial order of power law
μ	Dynamic viscosity of blood
f	Friction forces
c	Wave speed
$\mathbf{M}$	System matrix/Jacobian of Flux vector
$\mathbf{R}$	Right eigen matrix
$\mathbf{L}$	Left eigen matrix
$\mathbf{u}$	State vector of system
$\mathbf{S}$	RHS vector of system equations
$\mathbf{\Lambda}$	Eigenvalue matrix
λ	Eigenvalues
ω	Characteristic variable
ω	Angular frequency
α	Convective correction factor
α	Womersley number
β	Stiffness parameter for compliance law
h	Wall thickness
E	Young's modulus
A_d	Reference area for compliance law (diastolic)
A_0	Initial area
P_d	Reference pressure for compliance law (diastolic)
P_{ext}	External pressure for compliance law
P_{out}	Venous pressure
R_1	Impedance element of Windkessel boundary condition
R_2	Distal resistance of Windkessel boundary condition
C	Compliance of Windkessel boundary condition
R	Distal resistance of single resistance model
Z_c	Characteristic impedance of vessel
N	Nodes or elements
J_0	Complex Bessel function of zero order
J_1	Complex Bessel function of first order
ϵ	Relative error

1 Introduction

One-dimensional (1-D) models of blood flow have been extensively used to study wave propagation phenomena in arteries and veins. In contrast to 3-D fluid-structure interaction models, they are notably recognized to be computationally inexpensive. Pressure and flow pulse waveforms can be obtained at any points of extensive networks. Pulse waveforms are intimately related to physical properties of the cardiovascular system that are altered by disease (*e.g.* arterial geometry and stiffness). Through 1-D modelling we can investigate physical mechanisms underlying changes produced by disease in pulse wave patterns that can be measured *in vivo* and, hence, provide valuable information for the clinical assessment of cardiovascular function. Key contributions to 1-D modelling include the studies of Hughes and Lubliner [22], Avolio [5], Stettler *et al.* [47], Stergiopulos *et al.* [46, 37], Olufsen *et al.* [33], Formaggia *et al.* [17], Sherwin *et al.* [43], Bessems *et al.* [9], Mynard and Nithiarasu [32], and more recently Müller and Toro [28, 29], and Blanco *et al.* [11, 10].

The 1-D equations also form the basis of wave analysis tools for extracting clinically relevant information from waveform measurements; *e.g.* separation of waves into forward- and backward-traveling components [54] and wave intensity analysis [35]. For recent reviews on arterial pulse wave hæmodynamics see [50, 3]. For a historical overview of this field of research see [34] and the introductions in [22, 43, 50].

An increasing number of recent studies have shown the ability of the 1-D formulation to capture the main features of pressure, flow and area waveforms in large human arteries, using *in vivo* measurements [47, 33, 45, 37, 56], *in vitro* experiments [41, 8, 1, 39, 21], or 3-D numerical data [32, 57]. Although an exhaustive comparison between 1-D and 3-D formulations has recently been published [57], to date there have been very few comparisons among commonly used numerical schemes for 1-D blood flow modeling.

Different formulations and several corresponding numerical methods have been proposed to solve the 1-D equations, especially in the time domain. These include the method of characteristics [40, 51], finite element methods such as Galerkin [43, 45, 9, 32, 1, 53] and Taylor-Galerkin (combined with operator splitting techniques) [17] schemes, finite volume methods [49, 27, 30], and finite difference methods such as the Lax-Wendroff method [33, 6, 25] and the MacCormack method [19, 39]. Taylor-Galerkin and discontinuous Galerkin 1-D schemes were compared in an idealised artery with abrupt changes in material properties [42], and in a model of the aorta and cerebral arteries [4]. In these studies, however, there was no 'benchmark' data to compare with, and in the latter, the emphasis was more on the development of a methodology for parameter estimation than on providing a systematic comparison between numerical schemes. Using a different formulation, Müller and Toro [27] proposed and validated a novel 'well-balanced' scheme against the experimental results obtained in [1], but did not provide a cross-comparison among other schemes. Wang *et al.* [52] recently presented a comparison of four numerical schemes (local discontinuous Galerkin, MacCormack, Taylor-Galerkin, and a monotonic upwind scheme for conservation laws), tested on a single tube, a simple bifurcation and a network with 55 arteries. However, they did not rely on experimental or 3-D data to assess the accuracy of their 1-D numerical solutions.

The aim of this thesis is to compare the numerical methods used in STARFiSh (MacCormack, McC), with 5 other commonly used numerical schemes for arterial 1-D modelling in a series of

benchmark test cases. The schemes under consideration are: discontinuous Galerkin (DG), locally conservative Galerkin (LCG), Galerkin least-squares finite element method (FEM), finite volume method (FVM), and a simplified trapezium rule method (STM). The test cases are: *(i)* a model of blood flow in a reflection-free tube for which a theoretical solution exists; *(ii)* blood flow in the human common carotid artery, *(iii)* the upper thoracic aorta, and *(iv)* the aortic bifurcation, for which 3-D solutions are available from [57]; *(v)* blood flow in a network with 37 arterial segments representing the aorta and its largest branches, for which *in vitro* pressure and flow waveforms were acquired in [26]; and *(vi)* blood flow in the ADAN55 model, which contains the largest 55 systemic arteries of the human circulation under normal physiological conditions [11].

The outline of this Thesis is as follows. In Methods and Numerical solution I describe the 1-D formulation and numerical schemes used in this work paying special attention to common and particular aspects of each scheme, including the implementation of boundary conditions. The Descriptions of the five other schemes are relatively short, but includes the needed references for a more detailed description. The numerical methods used in STARFiSh is elaborated in more detail. Here I present the original (MacCormack) scheme, and suggest a new one. These sections also include a new bifurcation model, and a model that includes Womersley Theory. I then present all testcases used in the Thesis. In Gridadaption the numerical parameters used in STARFiSh's contribution to the article is decided. In the Results section I test and compare new and old implementations of STARFiSh in the six benchmark test cases, and in additional tests. Based on these results the numerical methods (solving scheme and Bifurcation model) used in STARFiSh's contribution to the article is decided. The Thesis also includes the final results (Results Comparison1Dscheme) and discussion (Discussion Comparison1Dscheme) of the six numerical schemes. Here we compare the numerical predictions of all six numerical schemes in all benchmark test cases.

2 Methods

This section contain the governing equations of 1-D compliant vessel flow. Three mathematically equivalent systems are presented. A mathematical manipulation (methods of characteristic) of the system(s), used when treating boundary-conditions is then performed. Lastly Womersley theory for pulsatile rigid pipe flow is presented.

2.1 Governing equations

The governing 1D-equations for flow and pressure propagation in a blood vessel is obtained by ensuring continuity of mass and momentum balance in a compliant vessel. The governing equations can be derived by use of Reynolds Transport Theorem for a movable control volume illustrated in figure 1, but this is omitted here. Blood is assumed incompressible and Newtonian, and the vessel wall to be impermeable.

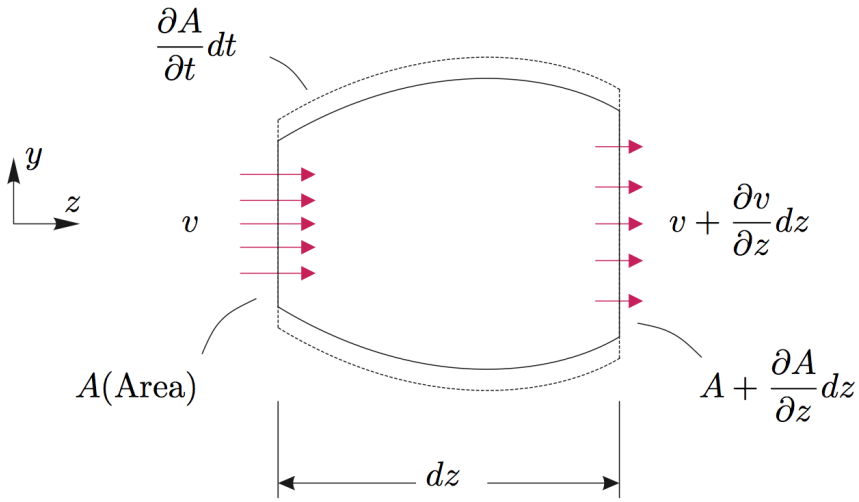

Figure 1: Moveable Control Volume.

2.1.1 A,Q system

The governing equations written in terms of the the variables (A, Q) [43] are:

$$\frac{\partial A}{\partial t} + \frac{\partial Q}{\partial x} = 0 \tag{1a}$$

$$\frac{\partial Q}{\partial t} + \frac{\partial \alpha Q^2/A}{\partial x} = -\frac{A}{\rho}\frac{\partial P}{\partial x} + \frac{f}{\rho} \tag{1b}$$

where A is the crossectional area, Q is the volumetric flow, and P is the pressure assumed constant over the crossection. ρ is the density of blood and f is frictional forces. α in the momentum equation accounts for nonlinearity in the crossectional integration of the local velocity $\hat{u}$ [43]:

$$\int_S \rho(\hat{u})^2 \mathrm{d}\sigma = \alpha\rho U^2 A = \alpha\rho QU \Rightarrow \alpha(x,t) = \frac{\int_S \hat{u}^2 \mathrm{d}\sigma}{AU^2} \tag{2}$$

Where U is the crossectional averaged velocity. Assuming a flat velocity profile results in $\alpha = 1$. A common way to asses the dependence on the local velocity profile on the convective and friction term is to assume a power law for the shape of the axial velocity given by:

$$u(x,\xi,t) = U(x,t)\frac{\zeta+2}{\zeta}\left[1-\left(\frac{\xi}{r}\right)^{\zeta}\right], \tag{3}$$

where $r(x,t)$ is the lumen radius, ξ is the radial coordinate and ζ is the polynomial order. This profile yields $f(x,t) = 2\mu\pi r\frac{\partial u}{\partial \xi}|_{\xi=r}$ [44], with μ the viscosity of blood, assumed to be constant. For the velocity profile given by Eq. (3) we have $f = -2\left(\zeta+2\right)\mu\pi U$ in which the local f is proportional to the local flow. Note that $\zeta = 2$ leads to the Poiseuille flow resistance $f = -8\mu\pi U$. By evaluating the integral in Eq. (2) with the assumed profile given by Eq. (3) leads to

$$\alpha(x,t) = \frac{\int_S \hat{u}^2 \mathrm{d}\sigma}{AU^2} = \frac{(\zeta+2)}{(\zeta+1)} \tag{4}$$

2.1.2 A,U system

An alternative formulation of Eqs. (1a) and (1b), can be formulated in terms of the variables (A,U). By assuming a flat velocity profile and inviscid flow the governing equations in terms of the (A, U) variables are [43]:

$$\frac{\partial A}{\partial t} + \frac{\partial UA}{\partial x} = 0 \tag{5a}$$

$$\frac{\partial U}{\partial t} + \frac{\partial U^2/2}{\partial x} = -\frac{1}{\rho}\frac{\partial P}{\partial x} \tag{5b}$$

Still neglecting the nonlinearity associated with the integration of the local velocity $\hat{u}$ given by Eq. (4), but not assuming inviscid flow the governing equations in terms of the variables (A, U) can be expressed in matrix form as:

$$\begin{gathered}\frac{\partial \mathbf{U}}{\partial t} + \frac{\partial \mathbf{F}}{\partial x} = \mathbf{S}, \\ \mathbf{U} = \begin{bmatrix} A \\ U \end{bmatrix}, \quad \mathbf{F} = \begin{bmatrix} AU \\ \frac{U^2}{2} + \frac{P}{\rho} \end{bmatrix}, \quad \mathbf{S} = \begin{bmatrix} 0 \\ \frac{f}{\rho A} \end{bmatrix}.\end{gathered} \tag{6}$$

2.1.3 Closing the system; Constitutive equation

Regardless of the formulation there are two governing equations with three primary variables. Either A, Q and P, or A, U and P, and thus a constitutive equation relating pressure and area is needed to close the system. The elasticity of the vessel wall is nonlinear and also exhibit viscoelastic effects, and thus this is a field of its own. In this thesis a purely algebraic relation between pressure and area have been used:

$$P = \mathrm{f}(A; x, t) \tag{7}$$

A commonly used constitutive relationship between P and A (or *tube law*) based on Laplace's law leads to [17]

$$P - P_{\mathrm{ext}} = P_{\mathrm{d}} + \frac{\beta}{A_{\mathrm{d}}}\left(\sqrt{A} - \sqrt{A_{\mathrm{d}}}\right), \tag{8}$$

where P_{ext} is the external pressure, $P - P_{\text{ext}}$ is the trans-mural pressure, and P_{d}, A_{d} are the diastolic pressure and area respectively. The term $\beta(x) = \frac{4}{3}\sqrt{\pi}Eh$ accounts for the material properties of the arterial wall, modeled here as a thin, incompressible, homogeneous, isotropic, elastic membrane with elastic modulus $E(x)$ and thickness $h(x)$. Despite the fact that it does not account for vessel collapse, and that it results in increasing compliance at high pressures, the simple relationship given by Eq. (8) has been used extensively [33, 17, 43, 32], and exclusively in this thesis. Regardless of the algebraic relation the compliance is defined as.

$$C = \frac{\partial A}{\partial P}, \tag{9}$$

The introduction of the compliance C, allows for a more generic representation of an algebraic constitutive equations

$$A(P) = A_0 + C\,(P - P_0) \tag{10}$$

The compliance is a measure of the vessels ability to expand and is related to the inverse of the elasticity. By introducing a compliance model equation (1a) and (1b) will take the form of Hyperbolic PDE's, and thus changes (e.g. in P, Q or A) at the boundaries will not be "felt" instantaneously in the domain, but will propagate with a finite velocity.

2.1.4 P,Q system

By applying the chain rule on the mass equation (1a) ($\frac{\partial A}{\partial t} = \frac{\partial A}{\partial P}\frac{\partial P}{\partial t}$)and combining with the momentum equation (1b), the governing equations can be written written in terms of the variables (P,Q) [50]:

$$\frac{\partial P}{\partial t} + \frac{1}{C}\frac{\partial Q}{\partial x} = 0 \tag{11a}$$

$$\frac{\partial Q}{\partial t} + \frac{\partial \alpha Q^2/A}{\partial x} = -\frac{A}{\rho}\frac{\partial P}{\partial x} + \frac{f}{\rho} \tag{11b}$$

A non-conventional matrix form of the P, Q system could be stated as

$$\begin{gathered} \frac{\partial \mathbf{U}'}{\partial t} + \frac{\partial \mathbf{F}'}{\partial x} = \mathbf{S}', \\ \mathbf{U}' = \begin{bmatrix} P \\ Q \end{bmatrix}, \quad \mathbf{F}' = \begin{bmatrix} \frac{Q}{C_c} \\ \frac{\alpha Q^2}{A} + \frac{A_c P}{\rho} \end{bmatrix}, \quad \mathbf{S}' = \begin{bmatrix} 0 \\ \frac{f}{\rho} \end{bmatrix}. \end{gathered} \tag{12}$$

Where C_c, and A_c denotes that these values are not differentiated, and thus for every term $\frac{\partial \mathbf{F}'}{\partial x}$, these values should be treated as constants, as is ρ. Alternatively the system may be written as

$$\mathbf{U}' = \begin{bmatrix} P \\ Q \end{bmatrix}, \quad \mathbf{F}' = \begin{bmatrix} \frac{Q}{C} \\ \frac{\alpha Q^2}{A} + \frac{A}{\rho}P \end{bmatrix}, \quad \mathbf{S}' = \begin{bmatrix} Q\frac{\partial}{\partial x}\left(\frac{Q}{C}\right) \\ \frac{f}{\rho} + P\rho\frac{\partial A}{\partial x} \end{bmatrix}, \tag{13}$$

in which (C, Q, A, P) are truly treated as variables in the evaluation of $\frac{\partial \mathbf{F}'}{\partial x}$. The above systems can also be rearranged and presented in non conservative Matrix form as follows

$$\begin{gathered} \frac{\partial \mathbf{U}'}{\partial t} + \mathbf{M}\frac{\partial \mathbf{U}'}{\partial x} = \mathbf{S}', \\ \mathbf{U}' = \begin{bmatrix} P \\ Q \end{bmatrix}, \quad \mathbf{M} = \begin{bmatrix} 0 & 1/C \\ C(c^2 - U^2\alpha) & 2\alpha U \end{bmatrix}, \quad \mathbf{S}' = \begin{bmatrix} 0 \\ \frac{f}{\rho} \end{bmatrix}. \end{gathered} \tag{14}$$

where the relation $\frac{\partial}{\partial x}\left(\frac{Q^2}{A}\right) = 2U\frac{\partial Q}{\partial x} - U^2\frac{\partial A}{\partial x}$ is used. Evaluating the integral in Eq. (3) leads to $\alpha = \frac{(\zeta+2)}{(\zeta+1)}$.

2.2 Characteristic variables and their relation with the state variables

Regardless of the formulation ((AQ), (AU) or (PQ)), the general hyperbolic system that is formed by Eq. (1a), (1b) and (10) may be presented in a general nonconservative form;

$$\frac{\partial \mathbf{U}}{\partial t} + \mathbf{M}\frac{\partial \mathbf{U}}{\partial x} = \mathbf{S}, \tag{15}$$

where $\mathbf{M}$-matrix is the Jacobian of the flux vector, *i.e.*

$$\mathbf{M} = \frac{\partial \mathbf{F}}{\partial \mathbf{U}} \tag{16}$$

The non-conservative representation (15) may be diagonalized (*i.e.* coupled into two independent wave equations) showing that there are two waves traveling in opposite directions with wave speeds.
The diagnoalization of (15) is obtained by decomposing $\mathbf{M} = \mathbf{R}\mathbf{\Lambda}\mathbf{L}$ [19], where $\mathbf{\Lambda}$ is the *diagonal* eigenvalue matrix with eigenvalues λ_1 and λ_2. The left and right eigenmatrices are denoted $\mathbf{L}$ and $\mathbf{R}$, respectively, and satisfy $\mathbf{LR} = \mathbf{I}$. A change of variables is obtained by multiplying (15) with

$$\frac{\partial \boldsymbol{\omega}}{\partial \mathbf{U}} = \mathbf{L}, \tag{17}$$

Assumption of negligible local viscous losses (*i.e.* zero right hand side) and subsequent use of the chain rule in reverse and the decomposition $\mathbf{M} = \mathbf{R}\mathbf{\Lambda}\mathbf{L}$ yields a system of decoupled wave equations:

$$\frac{\partial \boldsymbol{\omega}}{\partial t} + \mathbf{\Lambda}\frac{\partial \boldsymbol{\omega}}{\partial x} = 0 \Rightarrow \frac{d\boldsymbol{\omega}}{dt} = 0 \quad \text{if} \quad \lambda_1 = \frac{dx_f}{dt} \text{ and } \lambda_2 = \frac{dx_b}{dt} \tag{18}$$

which shows that ω_1 and ω_2 are constant (or invariant) along characteristic paths. Subject to assumptions of flat velocity profiles (convective correction factor $\alpha = 1$) the eigenvalues of $\mathbf{M}$ may be shown to be:

$$\lambda_{1,2} \equiv c_{\mathrm{f,b}} = U \pm c, \qquad c = \sqrt{\frac{A}{\rho}\frac{\partial P}{\partial A}} = \sqrt{\frac{A}{\rho}\frac{1}{C}} \tag{19}$$

which may be shown to hold for all formulations (AU,PU, PQ, AQ) of the governing equations. The characteristic variables may be found from (17):

$$\Delta\boldsymbol{\omega} = \int \mathbf{L}\, d\mathbf{U} \tag{20}$$

2.2.1 A,U system

For the AU-formulation:

$$\mathbf{F} = \mathbf{F}(\mathbf{U}) = \begin{bmatrix} AU \\ \frac{U^2}{2} + \frac{P}{\rho} \end{bmatrix} \quad \Rightarrow \mathbf{M} = \frac{\partial \mathbf{F}}{\partial \mathbf{U}} = \begin{bmatrix} U & A \\ c^2/A & U \end{bmatrix} \quad \Rightarrow \mathbf{L} = \begin{bmatrix} c/A & 1 \\ -c/A & 1 \end{bmatrix} \tag{21}$$

and concequently:

$$\Delta\omega_{1,2} = U \pm \int \frac{c}{A}\, dA \tag{22}$$

2.2.2 P,Q system

The system matrix M is represented in Eq. (14), and

$$\mathbf{\Lambda} = \begin{bmatrix} \lambda_1 & 0 \\ 0 & \lambda_2 \end{bmatrix} \quad , \lambda_1 = U\alpha + \sqrt{U^2\alpha^2 - U^2\alpha + c^2}, \quad \lambda_2 = U\alpha - \sqrt{U^2\alpha^2 - U^2\alpha + c^2} \tag{23}$$

With c given by the Bramwell-Hill equation $c^2C = A/\rho$ [13]. Notice that if one assumes $\alpha = 1$ also in the P,Q formulation the eigenvalues for the P,Q and A,U system will be the same. Further the following representations of the right and left eigenvalue matrices are obtained:

$$\mathbf{L} = \begin{bmatrix} 1 & Z_2 \\ 1 & -Z_1 \end{bmatrix}, \mathbf{R} = \frac{1}{Z_1 + Z_2} \begin{bmatrix} Z_1 & Z_2 \\ 1 & -1 \end{bmatrix} \tag{24}$$

With $Z_1 = \frac{1}{C\lambda_1}$, and $Z_2 = -\frac{1}{C\lambda_2}$, which may be recognized as the vessel impedance for forward and backward traveling waves respectively. By substitution of Eq. (24) into (20) integrating between two time-steps and applying the mean value theorem, the following expression relating primary anda characteristic variable is used when treating boundary-conditions:

$$\Delta P = R_{11}\Delta w_1 + R_{12}\Delta w_2 \tag{25a}$$
$$\Delta Q = R_{21}\Delta w_1 + R_{22}\Delta w_2 \tag{25b}$$

If in addition $U/c \ll 1$, the right and left eigenvalues will be equal, but with opposite signs. In such cases the forward and backward impedances will be equal. Inserting in Eq. (24), combining with (20) and integrating from diastolic to systolic values yields the classical results for wave separation is obtained[50]:

$$\Delta\omega_1 = \Delta p_f = \frac{\Delta p + Z_c\Delta Q}{2} \qquad \text{and} \qquad \Delta\omega_2 = \Delta p_b = \frac{\Delta p - Z_c\Delta Q}{2} \tag{26}$$

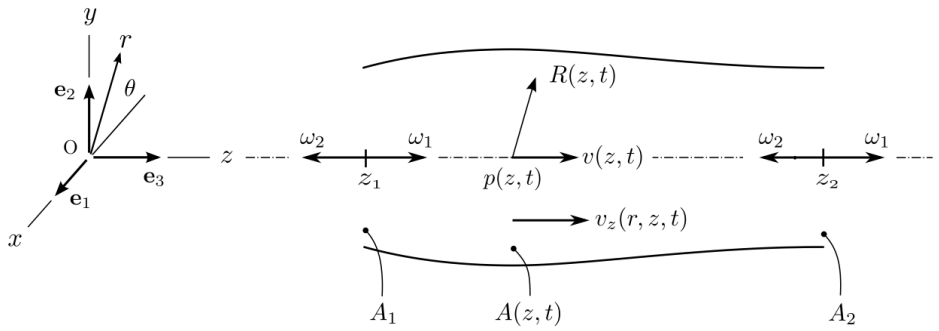

Figure 2: Illustration of compliant vessel with major axis along the z-axis. Given by vessel radius $R = R(z,t)$ and cross-section area $A = A(z,t)$. The axial fluid velocity is $v_z = v_z(r,z,t)$ and the cross sectional averaged fluid velocity and pressure are given by $v = v(z,t)$ and $p = p(z,t)$. The $A_1 = A_1(t)$ and $A_2 = A_2(t)$ boundaries define in/out-flow faces of the vessel fixed at the axial positions z_1 and z_2. The Riemann variables ω_1 and ω_2 in the positive and negative z-direction respectively, are illustrated as they leave the boundary surfaces A1 and A2. The figure is adapted from "Blood Flow in Compliant Vessels" [18]

2.3 Womersley Theory

In the previously described methods, the velocity is treated as known. However the velocity profile has an effect on both convective and friction term in the momentum equation. As mentioned earlier, the profile is commonly assumed flat in regards to the convective term, and a power law description given by Eq. (3) is commonly used for treating the friction term. Or one could use the assumed power law profile also in the convective term, by adding the nonlinear effect simply with the correction given by Eq. (4). Yet another method that could be used is the Womersley theory for periodic pulsatile flow [38]. With assumptions of periodic/pulsatile fully developed flow in infinite long rigid pipes, Womersley developed analytical solution for the velocityprofile. Even though these assumptions are relatively crude when it comes to flow in compliant vessels, with bifurcations, tapering and curvature, the velocity profile obtained with Womersley theory could yield a better estimation of the actual velocity profile, than assuming one akin to the one given by Eq. (3). In regards to Womersley theory it is convenient to write the momentum equation in its most general form, without assuming the velocity profile

$$\frac{\partial Q}{\partial t} + \frac{\partial \left(\int_A u^2 \mathrm{d}A \right)}{\partial x} = -\frac{A}{\rho} \frac{\partial P}{\partial x} + \frac{f}{\rho} \tag{27}$$

Using Womersleytheory yields the following expression for the velocity profile

$$u\left(r,t;x\right) = \frac{2}{\pi R^2}\left(1-\frac{r^2}{R^2}\right) Q_1 + \sum_n \mathrm{Re}\left(\frac{Q_n}{\pi R^2} \frac{1-\frac{J_0\left(\alpha j^{3/2} r/R\right)}{J_0\left(\alpha j^{3/2}\right)}}{1-\frac{2J_1\left(\alpha j^{3/2}\right)}{\alpha j^{3/2} J_0\left(\alpha j^{3/2}\right)}} \exp^{j\omega t} \right) \tag{28}$$

where $Q_n\left(x,t\right)$ is the n^{th} harmonic of the flow pulse, and J_0 and J_1 are the complex Bessel functions of zero and first order respectively. α_i is the Womersley number for each harmonic defined as $\alpha_i = R\left(\frac{\rho 2\pi \mathrm{f_i}}{\mu}\right)$ [38]. ω is the angular frequency defined as $\omega = 2\pi \mathrm{f_i}$. An analytic form of the friction term could also be obtained by differentiating Eq. (28) and using the definition for friction $f(x,t) = 2\mu\pi r \frac{\partial u}{\partial \xi}|_{\xi=r}$. However to reduce the number of computations needed, a numerical differentiation of the obtained velocity profile has been chosen in this work. Eq. (28) could also be stated with pressure gradient $\frac{d\mathrm{P}}{d\mathrm{x}}$ instead of Q. However using this formulation leads to a needed numerical evaluation of $\frac{d\mathrm{P}}{d\mathrm{x}}$, and a question arises when choosing dx and if to use static or total pressure [7]. Regardless,the signal of interest has to be transformed into the frequency domain. Previous work in STARFiSh has been done on the subject, by Hallvard Moian Nydal. He proposed methods for using future expanding Fourier transforms to obtain data for the convective and friction terms in the next time step. Azer *et al.* [7] proposed a method that integrate the Womersley theory in the governing momentum equation and that solve the system iteratively for each time step. Here I present a method inspired by Reymond *et al.* [38], which exploit the periodic nature of a full heart cycle. This method is thus primarily valid in cases where the period of the heart cycle is known, and constant. This is also in accordance with the Womersley theory. The procedure is done as follows; First, one full cycle is run by assuming a profile shape given by Eq. (3), from which the flow data for all interior nodes is transformed into the frequency domain by a FFT (Fast Fourier Transform). From this data the velocity profiles for every node and every time step (could calculate for less time steps and interpolate to use in correct time) of one cycle is calculated. From the obtained profiles, $\int_A u^2 \mathrm{d}A$ is evaluated numerically with use of a trapezoidal rule, and stored for usage in Convective term in next heart cycle. Similarly $\frac{\partial u}{\partial \xi}|_{\xi=r}$, is calculated by a forward euler and fed into the friction term in the next heart cycle. The procedure is repeated until convergence.

3 Numerical solution

This sections outlines the six numerical schemes used in this work. We focus on highlighting common and particular aspects of each method and refer the reader to our previous papers in which these schemes are described in detail.
Each segment of the computational domain Ω is discretised according to the chosen method, using either finite elements (DG, LCG, FEM), finite volumes (FVM), finite differences (McC), or any equivalent spatial discretisation (STM). In order to define the characteristic spatial discretisation, an element, a cell or finite difference stencil are equally referred to as Ω_e.

STARFiSh uses the MacCormack scheme. The numerical methods used for the five other schemes are written in short descriptions, with needed references for a more detailed one. The numerical methods used in STARFiSh is elaborated in more detail. These same methods have been used for the Womersley model with the needed changes to treat the convective and friction terms.

3.1 Discontinuous Galerkin (DG) scheme

The DCG scheme solves Eq. (6) together with the tube law given by Eq. (8). The discrete weak form is obtained by multiplying the resulting system by Galerkin test functions, which belong to the finite space of piecewise polynomial vector functions, and by integrating over the domain Ω. The solution vector is expanded using high-order Legendre polynomials, which may be discontinuous across inter-element boundaries, resulting in a spectral/*hp* spatial discretization. Information is propagated between elemental regions Ω_e through the flux term $\mathbf{F}$, using the characteristics variables introduced in Section 2.2. Time integration is performed by means of an explicit second-order Adams-Bashforth method. A detailed description of this scheme is given in [3] and of the spectral/*hp* element methods in [23]. The flux correction factor α given by Eq. (4) in the convective term is taken to be 1.

3.2 Locally conservative Galerkin (LCG) scheme

The LCG method is based on a standard finite element Galerkin procedure, with the addition of Taylor-Garlerkin stabilisation [42]. The scheme is derived as in the DCG method, but in this case, the solution vector is expanded using a piecewise linear approximation. Elements Ω_e are treated as sub-domains with their own boundaries, so that only small systems are solved locally and independently of one another, *i.e.* without the need for assembling global arrays. Information is propagated between elements at each time step using interface fluxes and, at global mesh nodes, contributions from different elements are averaged to provide a unique solution. The scheme is first order in space and second order in time. The resulting equations must satisfy the Courant-Friedrichs-Lewy (CFL) stability condition. See [32, 48] for a detailed exposition and further references. The flux correction factor α given by Eq. (4) in the convective term is taken to be 1.

3.3 Finite Volume (FV) scheme

In the FEM, the equivalent AQ formulation is rewritten in characteristic form and discretised in time using an implicit finite difference Euler scheme. A least-squares approach is used to formulate a variational problem on top of which a Galerkin finite element method is employed for the spatial discretisation. The method is implicit, requiring the assembly of the matrix

system at each time step. However, no CFL constraint must be satisfied. First-order spatial approximation is used and nonlinearities are treated using fixed point iterations. See [53] for a detailed exposition. The flux correction factor α given by Eq. (4) in the convective term is taken to be 1.

3.4 Galerkin Least-Squares Finite Element (FE) scheme

The system is written in terms of conserved variables AQ Eqs. (1a)-(1b) and reformulated as proposed in [49] in order to treat varying mechanical properties up to the limiting case of discontinuous properties. The resulting non-conservative system is solved using a finite-volume type numerical scheme [31]. The numerical scheme is fully explicit and allows for arbitrary space-time accuracy. In order to preserve the space-time accuracy at bifurcations, a special treatment is applied [30]. The time step is computed adaptively at each time iteration, in order to satisfy the corresponding CFL condition. The flux correction factor α given by Eq. (4) in the convective term is taken to be 1.

3.5 MacCormack (McC) scheme

This section present the general MacCormack scheme used for solving interior nodes in STARFiSh. Further two different applications on the P,Q system is presented; original (non-conservative), and new (conservative).

3.5.1 Derivation of the MacCormack scheme for a general hyperbolic system

Given a general hyperbolic system of the form:

$$\frac{\partial \mathbf{U}}{\partial t} + \frac{\partial \mathbf{F}}{\partial x} = \mathbf{b} \tag{29}$$

the derivation of the MacCormack method proceeds in two steps: a predictor and a corrector step. At the predictor step a provisional value of $\bar{\mathbf{U}}_i^{n+1} = \mathbf{U}_i^p$ is estimated with forward euler difference for both the temporal and spatial derivatives:

$$\frac{\mathbf{U}_i^{n+1} - \mathbf{U}_i^n}{\Delta t} = -\frac{\mathbf{F}_{i+1}^n - \mathbf{F}_i^n}{\Delta x} + \mathbf{b} \tag{30}$$

rearraning so that $\bar{\mathbf{U}}_i^{n+1} = \mathbf{U}_i^p$ is alone on LHS gives:

$$\mathbf{U}_i^p = \mathbf{U}_i^n - \Delta t \frac{\mathbf{F}_{i+1}^n - \mathbf{F}_i^n}{\Delta x} + \Delta t \mathbf{b} \tag{31}$$

In the corrector step a backward finite difference approximation is utilized for the spatial derivatives, and the time step used in the in the temporal derivative is $\Delta t/2$ leading to:

$$\frac{\mathbf{U}_i^{n+1} - \mathbf{U}_i^{n+1/2}}{\Delta t/2} = -\frac{\mathbf{F}_i^p - \mathbf{F}_{i-1}^p}{\Delta x} + \mathbf{b} \tag{32}$$

rearranging so that $\mathbf{U}_i^{n+1}$ is alone on LHS and using the approximation $\mathbf{U}_i^{n+1/2} = \frac{\mathbf{U}_i^{n+1} + \mathbf{U}_i^p}{2}$ gives:

$$\mathbf{U}_i^{n+1} = \frac{\mathbf{U}_i^{n+1} + \mathbf{U}_i^p}{2} - \frac{\Delta t}{2}\frac{\mathbf{F}_i^p - \mathbf{F}_{i-1}^p}{\Delta x} + \frac{\Delta t}{2}\mathbf{b} \tag{33}$$

3.5.2 Application on 1D-system

In the original scheme for solving the governing equations in the interior nodes of the vessels, the system is written in the matrix form given by Eq. (14). This may be recognized as the nonconservative form of the general hyperbolic system given by Eq. (29), where:

$$\frac{\partial \mathbf{F}}{\partial x} = \mathbf{M}\left(\mathbf{U}\right)\frac{\partial \mathbf{U}}{\partial x}, \quad \mathbf{M} = \frac{\partial \mathbf{F}}{\partial \mathbf{U}} \tag{34}$$

Substituting into Eq. (33) leads the following form of the MacCormack predictor corrector method:

$$\begin{aligned} \hat{\mathbf{U}}_i &= \mathbf{U}_i^n - \Delta t\left(\mathbf{M}\left(\mathbf{U}_i^n\right)\frac{\left(\mathbf{U}_{i+1}^n - \mathbf{U}_i^n\right)}{\Delta x} + \mathbf{S}'\left(\mathbf{U}_i^n\right)\right), \\ \mathbf{U}_i &= \frac{1}{2}\left(\mathbf{U}_i^n + \hat{\mathbf{U}}_i - \Delta t\left(\mathbf{M}\left(\hat{\mathbf{U}}_i\right)\frac{\left(\hat{\mathbf{U}}_i - \hat{\mathbf{U}}_{i-1}\right)}{\Delta x} + \mathbf{S}'\left(\hat{\mathbf{U}}_i\right)\right)\right), \end{aligned} \tag{35}$$

Even though the different formulations in Eq. (34) is mathematically equivalent for arbitrary, nonlinear fluxes, their numerical implementation is not [20]. This can be exemplified for instance by looking at the term:

$$\mathbf{M}\left(\mathbf{U}_i^n\right)\frac{\left(\mathbf{U}_{i+1}^n - \mathbf{U}_i^n\right)}{\Delta x} \tag{36}$$

if one sum all contributions of this term over all grid nodes in a domain there will be residual internal flux contributions. Let's look at a domain with N grid nodes. Summing over all nodes leads to:

$$\begin{aligned} &\mathbf{M}\left(\mathbf{U}_1^n\right)\frac{\left(\mathbf{U}_2^n - \mathbf{U}_1^n\right)}{\Delta x} + \mathbf{M}\left(\mathbf{U}_2^n\right)\frac{\left(\mathbf{U}_3^n - \mathbf{U}_2^n\right)}{\Delta x} + \mathbf{M}\left(\mathbf{U}_3^n\right)\frac{\left(\mathbf{U}_4^n - \mathbf{U}_3^n\right)}{\Delta x} + ...+ \\ &\mathbf{M}\left(\mathbf{U}_{N-3}^n\right)\frac{\left(\mathbf{U}_{N-2}^n - \mathbf{U}_{N-3}^n\right)}{\Delta x} + \mathbf{M}\left(\mathbf{U}_{N-2}^n\right)\frac{\left(\mathbf{U}_{N-1}^n - \mathbf{U}_{N-2}^n\right)}{\Delta x} + \mathbf{M}\left(\mathbf{U}_{N-1}^n\right)\frac{\left(\mathbf{U}_N^n - \mathbf{U}_{N-1}^n\right)}{\Delta x} \end{aligned} \tag{37}$$

where no terms cancel, leading to numerical flux contributions from the interior. On contrary, if one perform the same analysis on the conservative form leads to

$$\begin{aligned} &\frac{\left(\mathbf{F}_2^n - \mathbf{F}_1^n\right)}{\Delta x} + \frac{\left(\mathbf{F}_3^n - \mathbf{F}_2^n\right)}{\Delta x} + \frac{\left(\mathbf{F}_4^n - \mathbf{F}_3^n\right)}{\Delta x} + ...+ \\ &\frac{\left(\mathbf{F}_{N-2}^n - \mathbf{F}_{N-3}^n\right)}{\Delta x} + \frac{\left(\mathbf{F}_{N-1}^n - \mathbf{F}_{N-2}^n\right)}{\Delta x} + \frac{\left(\mathbf{F}_N^n - \mathbf{F}_{N-1}^n\right)}{\Delta x} = \frac{\left(\mathbf{F}_N^n - \mathbf{F}_1^n\right)}{\Delta x} \end{aligned} \tag{38}$$

where only the flux contributions from the nodes remain. Indeed this is why its called conservative form, and sometimes called the 'telescoping property' of the flux terms [20]. In the current implementation $\mathbf{M}\left(\mathbf{U}_i^n\right)$ is evaluated at the point of interest. This is not fundamental, and $\mathbf{M}\left(\mathbf{U}_{i+1/2}^n\right)$, or $\mathbf{M}\left(\mathbf{U}_{i+1}^n\right)$ might be a better choice. This problem is avoided by keeping the governing equation in its conservative form. A related question arises also in the conservative form. Looking at the governing equation for the P, Q system, the Compliance in the mass equation, and Area in pressure term in momentum equation is not part of the differentiation, and thus for every term $\frac{\left(\mathbf{F}_{i+1}^n - \mathbf{F}_i^n\right)}{\Delta x}$ a value of P and C between P_i^n and P_{i+1}^n, and C_i^n and C_{i+1}^n has to be chosen to be used in both flux terms $\left(\mathbf{F}_{i+1}^n, \mathbf{F}_i^n\right)$. Since the wavelength in general is long in physiological conditions, the effect of this choice is likely not very big. However it

is something to have in mind. I would assume that the effect is more prominent in the mass equation than in the momentum equation, keeping in mind that the Compliance is a differentiated variable ($C(P;x,t) = \frac{\partial A}{\partial P}$). Looking at the A, U system given by Eq. (5b), one can see that it has a very compact conservative form, and no evaluation of dependent (A, P, Q, C) variables are needed. Worth noting is that the way this A,U system is written assumes a flat velocity-profile in regards to the convective term. In the A, Q system this is avoided in the mass equation.
The following MacCormack scheme, slightly altered from the general scheme have been implemented:

$$\mathbf{U}_i^p = \mathbf{U}_i^n - \Delta t \frac{\mathbf{F}_{i+1}^n|_{C_c,A_c} - \mathbf{F}_i^n|_{C_c,A_c}}{\Delta x} + \Delta t \mathbf{b}\left(\mathbf{U}_i^n\right) \tag{39}$$

$$\mathbf{U}_i^{n+1} = \frac{\mathbf{U}_i^{n+1} + \mathbf{U}_i^p}{2} - \frac{\Delta t}{2} \frac{\mathbf{F}_i^p|_{C_c,A_c} - \mathbf{F}_{i-1}^p|_{C_c,A_c}}{\Delta x} + \frac{\Delta t}{4}\left(\mathbf{b}\left(\mathbf{U}_i^p\right) + \mathbf{b}\left(\mathbf{U}_i^n\right)\right) \tag{40}$$

where $C_c = C_i^n$ or $C_c = C_i^p$, and $P_c = P_i^n$ or $P_c = P_i^p$ respectively, and

$$\mathbf{F} = \begin{bmatrix} \frac{Q}{C_c} \\ \frac{\alpha Q^2}{A} + \frac{A_c P}{\rho} \end{bmatrix} \tag{41}$$

Because of the needed evaluation of C_c, and A_c, one could argue that this P,Q flux lack the 'telescoping property'. The predictor corrector method is second order in time and space [20]. Stability requires that the CFL (Courant-Friedrichs-Lewy) condition is satisfied $CFL \leq 1$, where the CFL number is given by $CFL = \frac{\Delta t}{\Delta x}\left(|U| + c\right)_{max}$. The flux correction factor α given by Eq. (4) in the convective term is evaluated from the assumed velocity profile given by Eq. (3), leading to $\alpha = \frac{(\zeta+2)}{(\zeta+1)}$. However, in the final solutions submitted in Comparison1Dscheme, the correction factor is set to one.

3.6 Simplified Trapezium Rule Method (STM)

The STM scheme solves the PQ system for a domain discretised into non-overlaping two noded elements after linearisation, time discretisation and spatial integration along the vessel axis. Linearisation is performed by Newton's method up to first order, time discretization is achieved using a second order backward difference scheme and integration is done using the trapezium rule. It can be shown that continuity of static pressure is automatically satisfied using this method, and thus no additional coupling equations are required. For more details regarding the numerical scheme, we refer the reader to [24]. The flux correction factor α given by Eq. (4) in the convective term is taken to be 1.

3.7 Boundary conditions

Given that we have a convection-dominated problem with sub-critical flow, we need to prescribe one boundary condition at both the inlet and outlet of each arterial domain Ω. We classify them into *inflow* (Sect. 3.7.1), *junction* (Sect. 3.7.2) and *terminal* (Sect. 3.7.3) boundary conditions.

3.7.1 Inflow boundary condition

In all test cases presented below, the volume flow rate $Q_{\text{in}}(t)$ is imposed at the inlet of single-domain models (4.1, 4.2 and 4.3) or at the root of network models (Sections 4.4, 4.5 and 4.6). This amounts to consider the following condition at the corresponding terminal site

$$Q = Q_{\text{in}}(t) \tag{42}$$

where $Q_{\text{in}}(t)$ is a given function of time.
To avoid spurious reflections in the DCG, FVM, LCG and McC schemes, values of the primitive variables are determined from the prescribed flow rate using the characteristic variables, following the same procedure as described below for terminal boundary conditions. For the FEM the inflow condition is strongly imposed in the system matrix by replacing the incoming characteristic equation by the boundary condition. For the STM method, however, enforcing continuity of propagating characteristic variables is not required.

3.7.2 Junction matching conditions

In the 1-D formulation the nodes connecting the arterial segments are treated as discontinuities. Detailed 3-D calculations of flow at arterial bifurcations show that the flow is generally very complex with the possibility of transient separation and the development of secondary flows. Most of these flow features are confined to the region near the bifurcation and their effect on pulse wave propagation is commonly neglected in the 1-D formulation. In this study, we connect arterial domains at junctions by enforcing conservation of mass, and continuity of both total pressure ($P + \frac{1}{2}\rho U^2$) and propagating characteristics variables. The McC scheme originally had a linearized method which lead to continuity of static pressure throughout the bifurcation. The STM scheme uses this linearized method

In cases with branching into vessels with big difference in radius, the difference between the two methods used in branching could be relatively big. Previously, only the linear method which ensures continuity of static pressure was implemented in Starfish. Here I present an implementation of the nonlinear method which ensures continuity of total pressure, propagating characteristics variables and conservation of mass. Looking at the bifurcation, information from inside the mother vessel can only reach the bifurcation from ω_1^1, and similarly information from inside the two daughter vessels can only reach the bifurcation from ω_2^2 and ω_3^2, respectively. Where subscript 1, 2, 3 denotes mother-vessel, left daughter vessel and right daughter vessel respectively, and superscript 1, 2 denotes forward or backward characteristics. ω_1^1 was a distance $\Delta x_1 = \lambda_1^1 \Delta t$, proximal to the bifurcation node at time t^n. Similarly ω_2^2 was a distance $\Delta x_2 = -\lambda_2^2 \Delta t$ distal to the boundary node in the left daughter vessel, and ω_3^2 was a distance $\Delta x_3 = -\lambda_3^2 \Delta t$ distal to the boundary node in the right daughter vessel at time t^n. Continuity of propagating characteristics variables thus leads to the following three equations:

$$\omega_1^1\left(x_1, t^{n+1}\right) = \omega_1^1\left(x_1 - \Delta x_1, t^n\right) \tag{43a}$$
$$\omega_2^2\left(x_2, t^{n+1}\right) = \omega_2^2\left(x_2 + \Delta x_2, t^n\right) \tag{43b}$$
$$\omega_3^2\left(x_3, t^{n+1}\right) = \omega_3^2\left(x_3 + \Delta x_3, t^n\right) \tag{43c}$$

Where x_1, x_2, x_3 denotes the position of bifurcation in mother vessel, left and right daughter vessel respectively. In addition Conservation of Mass, and continuity of total Pressure in the bifurcation contributes with three additional equations:

$$Q_1 = Q_2 + Q_3 \tag{44a}$$
$$P_1 + \rho\,\frac{1}{2}U_1^2 = P_2 + \rho\frac{1}{2}U_2^2 \tag{44b}$$
$$P_1 + \rho\,\frac{1}{2}U_1^2 = P_3 + \rho\frac{1}{2}U_3^2 \tag{44c}$$

This yields six equations for the six unknowns, P_1, P_2, P_3, Q_1, Q_2 and Q_3. However by discretization of the pressure and flow with the Riemann invariants according to Eq. (25a) and (25b), Eqs. (43a) - (43c) are automatically satisfied, and thus reduces the number of unknowns from six, to the three unknown characteristics ω_1^2, ω_2^1 and ω_3^1. Rearranging so that RHS is 0 in Eqs. (44a), (44b) and (44c), and using Δ values when discretization of the pressure and flow yields the following three functions

$$\begin{aligned} f_1\left(\omega_1^2, \omega_2^1, \omega_3^1\right) = Q_1^n + R21_1\Delta\omega_1^1 + R22_1\Delta\omega_1^2 \\ -Q_2^n - R21_2\Delta\omega_2^1 - R22_2\Delta\omega_2^2 - Q_3^n - R21_3\Delta\omega_3^1 - R22_3\Delta\omega_3^2 = 0 \end{aligned} \tag{45}$$

$$\begin{aligned} f_2\left(\omega_1^2, \omega_2^1, \omega_3^1\right) = P_1^n + R11_1\Delta\omega_1^1 + R12_1\Delta\omega_1^2 + \rho\frac{1}{2}\frac{\left(Q_1^n + R21_1\Delta\omega_1^1 + R22_1\Delta\omega_1^2\right)^2}{A_1^2} \\ -P_2^n - R11_2\Delta\omega_2^1 - R12_2\Delta\omega_2^2 - \rho\frac{1}{2}\frac{\left(Q_2^n + R21_2\Delta\omega_2^1 + R22_2\Delta\omega_2^2\right)^2}{A_2^2} \end{aligned} \tag{46}$$

$$\begin{aligned} f_3\left(\omega_1^2, \omega_2^1, \omega_3^1\right) = P_1^n + R11_1\Delta\omega_1^1 + R12_1\Delta\omega_1^2 + \rho\frac{1}{2}\frac{\left(Q_1^n + R21_1\Delta\omega_1^1 + R22_1\Delta\omega_1^2\right)^2}{A_1^2} \\ -P_3^n - R11_3\Delta\omega_3^1 - R12_3\Delta\omega_3^2 - \rho\frac{1}{2}\frac{\left(Q_3^n + R21_3\Delta\omega_3^1 + R22_3\Delta\omega_3^2\right)^2}{A_3^2} \end{aligned} \tag{47}$$

Being nonlinear the equations need to be solved iteratively for each time-step. A_1, A_2 and A_3 is also dependent on the pressure and should be updated for each iteration. The Nonlinear equations were solved for each time step by the Newton-Raphson method given by:

$$\boldsymbol{x_{i+1}} = \boldsymbol{x_i} - (\boldsymbol{J_i})^{-1} f_i \tag{48}$$

where J is the Jacobi Matrix:

$$J_{jk} = \frac{\partial f_j}{\partial x_k} \tag{49}$$

where $\boldsymbol{x} = [x_1, x_2, x_3] = [\Delta\omega_1^2, \Delta\omega_2^1, \Delta\omega_3^1]$, $\boldsymbol{f} = [f_1, f_2, f_3]$, $J_{jk} = \frac{\partial f_j}{\partial x_k}$, $j = 1, 2, 3, k = 1, 2, 3$. Performing the differentiations lead to the following Jacobi, and inverse Jacobi matrices:

$$\mathbf{J} = \begin{bmatrix} a & b & c \\ d & e & 0 \\ f & 0 & g \end{bmatrix}, \quad \mathbf{J^{-1}} = \begin{bmatrix} eg & -bg & -ce \\ -dg & ag - cf & cd \\ -ef & bf & ae - bd \end{bmatrix} \frac{1}{aeg - bdg - cef}. \tag{50}$$

where

$$a = R22_1 \tag{51a}$$

$$b = -R21_2 \tag{51b}$$

$$c = -R21_3 \tag{51c}$$

$$d = f = R12_1 + \rho\frac{\left(Q_1^n + R21_1\Delta\omega_1^1 + R22_1\Delta\omega_1^2\right)R22_1}{A_1^2} \tag{51d}$$

$$e = -R11_2 - \rho\frac{\left(Q_2^n + R21_2\Delta\omega_2^1 + R22_2\Delta\omega_2^2\right)R21_2}{A_2^2} \tag{51e}$$

$$g = -R11_3 - \rho\frac{\left(Q_3^n + R21_3\Delta\omega_3^1 + R22_3\Delta\omega_3^2\right)R21_3}{A_3^2} \tag{51f}$$

The iterations are started with $\boldsymbol{x}$ values from the previous time-step. The iterations are stopped with criteria based on the three functions $\boldsymbol{f}(\boldsymbol{x}) = [f_1, f_2, f_3] < [10^{-14}, 10^{-4}, 10^{-4}]$. Keeping in mind that f_1, is a mass/flow equation, and the two others are pressure equations.

3.7.3 Terminal boundary conditions

In peripheral vessels (small arteries, arterioles and capillaries), fluid resistance dominates over wall compliance and fluid inertia, which are both dominant in large arteries. The effect of peripheral resistance on pulse wave propagation in large 1-D model arteries is commonly simulated using linear lumped parameter models (or zero-dimensional (0-D) models) coupled to 1-D model terminal branches. In this Thesis, I use the following three types of terminal boundary conditions: completely absorbent outflow conditions, single-resistance models, or matched three-element Windkessel models. The latter is required in models in which peripheral vessels include large compliant arteries. This model relates the pressure and the flow at the end point of a terminal domain Ω through

$$Q\left(1+\frac{R_1}{R_2}\right)+CR_1\frac{\partial Q}{\partial t}=\frac{P-P_{\text{out}}}{R_2}+C\frac{\partial P}{\partial t}. \tag{52}$$

It consists of a resistance R_1 connected in series with a parallel combination of a second resistance R_2 and a compliance C . The resistance R_1 is equal to the characteristic impedance of the end point in Ω to minimise wave reflections [2].
More sophisticated terminal models include 0-D models with time-dependent resistances to simulate flow control mechanisms [2], single tapering vessels [32] and structured-tree networks [33, 14] to capture wave propagation phenomena in downstream vessels, and 0-D (compartmental) models of parts of the cardiovascular system that are not simulated using the 1-D formulation (*e.g.* the chambers of the heart and the venous circulation) [28, 29, 25, 36].

The McC scheme discretized the governing equation of the three-element Windkessel around the next time step $t^n + \Delta t$, with central differences for the derivatives of P and Q, which give

$$(Q^n+\Delta Q)\left(1+\frac{R_1}{R_2}\right)+CR_1\frac{\Delta Q}{\Delta t}=\frac{P^n+\Delta P-P_{\text{out}}}{R_2}+C\frac{\Delta P}{\Delta t}. \tag{53}$$

The Δ values of P and Q are further formulated in terms of the Riemann invariables according to Eq. (17), and where the right eigenvalue matrix $\mathbf{R}\left(\hat{\mathbf{U}}\right)$ is evaluated at the time step t^n. inserting in Eq. (53) gives

$$\begin{aligned}\Delta P &= r_{11}\Delta\omega_1 + r_{12}\Delta\omega_2,\\ \Delta Q &= r_{21}\Delta\omega_1 + r_{22}\Delta\omega_2,\end{aligned} \tag{54}$$

$$\begin{aligned}&(Q^n + r_{21}\Delta\omega_1 + r_{22}\Delta\omega_2)\left(1+\frac{R_1}{R_2}\right)+CR_1\frac{r_{21}\Delta\omega_1 + r_{22}\Delta\omega_2}{\Delta t} =\\ &\frac{P^n + r_{11}\Delta\omega_1 + r_{12}\Delta\omega_2 - P_{\text{out}}}{R_2}+C\frac{r_{11}\Delta\omega_1 + r_{12}\Delta\omega_2}{\Delta t}.\end{aligned} \tag{55}$$

The characteristic variable traveling from proximal to distal direction ω_1, can be calculated from the eigenvalue λ_1 of the system matrix $\mathbf{M}$ (See Sect. 2.2). ω_1 was a distance $\Delta x' = \lambda_1\Delta t$, proximal to the terminal boundary node at time t^n. This leaves ω_2 the only unknown in Eq. (55), and is thus solved for. The Δ values of the primary variables P and Q is then calculated from Eq. (25b) and the values at time step $t^n + \Delta t$ is updated.

A Similar approach is made in the case of single-resistance terminal model ($P - P_{out} = QR$). Where R is the distal resistance. In the case of completely absorbent outflow condition, this is obtained by simply setting $\omega_2 = 0$.

3.8 Error calculations

For the test cases presented in Sects. 4.2, 4.3 and 4.4, the numerical solutions of pressure P, volumetric flow rate $Q = AU$ and luminal radius r were compared between the 1-D and 3-D formulations, based on the results obtained by Xiao *et al.* [57]. For the benchmark problem presented in Sect. 4.5, the numerical solutions of the 1-D problem are compared at each measuring site, as determined from the data in Matthys et al. [26].
We use the following relative error metrics:

$$\mathcal{E}_P^{RMS} = \frac{1}{n}\sum_{i=1}^{n}\sqrt{\left(\frac{P_i^{1D} - \mathscr{P}_i}{\mathscr{P}_i}\right)^2}, \qquad \mathcal{E}_Q^{RMS} = \frac{1}{n}\sum_{i=1}^{n}\frac{\sqrt{\left(Q_i^{1D} - \mathscr{Q}_i\right)^2}}{max_j(\mathscr{Q}_j)}, \tag{56}$$

$$\mathcal{E}_P^{MAX} = \max_i\left|\frac{P_i^{1D} - \mathscr{P}_i}{\mathscr{P}_i}\right|, \qquad \mathcal{E}_Q^{MAX} = \max_i\left|\frac{Q_i^{1D} - \mathscr{Q}_i}{max_j(\mathscr{Q}_j)}\right|, \tag{57}$$

$$\mathcal{E}_P^{SYS} = \frac{max(P^{1D}) - max(\mathscr{P})}{max(\mathscr{P})}, \qquad \mathcal{E}_Q^{SYS} = \frac{max(Q^{1D}) - max(\mathscr{Q})}{max(\mathscr{Q})}, \tag{58}$$

$$\mathcal{E}_P^{DIAS} = \frac{min(P^{1D}) - min(\mathscr{P})}{min(\mathscr{P})}, \qquad \mathcal{E}_Q^{DIAS} = \frac{min(Q^{1D}) - min(\mathscr{Q})}{max(\mathscr{Q})}, \tag{59}$$

where P_i^{1D} and Q_i^{1D} are the results obtained from the 1-D solutions at a given spatial location, and for each time point i, and $\mathscr{P}_i$ and $\mathscr{Q}_i$ are either the cross-sectional averaged pressure and flow from the 3-D model, or the instantaneous values measured *in vitro*. The number of time points n is determined by the 3-D solution (1 kHz) for the test cases, and by the experimental sampling rate for the benchmark problem (1 kHz). In addition, when comparing quantities such a radii and pressure differences (ΔP) between the inlet and the outlet of a domain Ω, we use definitions similar to those in Eq. (56) for the flow rate, with Q replaced by r or ΔP, respectively. All error metrics were calculated over a single cardiac cycle, after the numerical results achieved periodic behaviour.

4 Tests

In this section a series of eight tests are presented. Tests 4.1 to 4.6 are adapted from Comparison1Dscheme, whereas test 4.7 and 4.8 are primarily tests of the implemented link/bifurcation model presented in Sect. 3.7.2, and the two schemes in Sect. 3.5.

4.1 Propagation of a single pulse in a straight vessel

This test simulates the propagation of a narrow Gaussian-shaped wave in a single vessel with uniform parameters and a completely absorbent outflow boundary condition; *i.e.* with a zero reflection coefficient that absorbs any incident wave [4]. The parameters of this model, which we refer to as the *single-pulse model*, are given in Table 1. At the inlet, a volume inflow rate with a peak value of 1 ml s^{-1} is prescribed using the function

$$Q_{\text{in}} = 10^{-6} \exp\left(-10000(t-0.05)^2\right) \quad \text{m}^3\text{s}^{-1}, \tag{60}$$

with t given in seconds. The solution is determined using Eq. (8) with $A_{\text{d}} = A_0$ and $P_{\text{d}} = P_{\text{ext}} = 0$. Two different values of blood viscosity (μ) are considered: $\mu = 0$ (inviscid problem) and $\mu = 4$ mPa s.

Property	Value
Length, L	10 m
Cross-sectional area, A_0	π cm^2
Wall thickness, h	1.5 mm
Blood mass density, ρ	1050 kg m^{-3}
Blood viscosity, μ	4 mPa s
Velocity profile order, ζ	9
Young's modulus, E	400 kPa
Diastolic pressure, P_{d}	0
External pressure, P_{ext}	0
Outflow pressure, P_{out}	0

Table 1: Model parameters of the single-pulse model taken from [4]. The calculated pulse wave velocity at A_0 is $c_0 = 6.17$ m s^{-1}.

4.2 CCA

The common carotid artery is simulated as a single vessel with uniform properties coupled to a three-element lumped parameter model of the rest of the systemic circulation [57]. The parameters of this model are given in Table 2. The initial area $A_0 = 0.22038$ cm^2 that yields the reference diastolic area $A_{\text{d}} = 0.28274$ cm^2 at $P = P_{\text{d}} = 10.933$ kPa is calculated using

$$A_0 = A_{\text{d}} \left(1 - \sqrt{A_{\text{d}}} \frac{P_{\text{d}}}{\beta}\right)^2. \tag{61}$$

This expression follows from Eq. (8) by considering $P = 0$, $A = A_{\text{d}}$ and solving for A_0.

Property	Value
Length, L	126 mm
Radius at diastolic pressure, r_d	3 mm
Wall thickness, h	0.3 mm
Blood density, ρ	$1,060$ Kg m^{-3}
Blood viscosity, μ	4 mPa s
Velocity profile order, ζ	2
Young's modulus, E	700.0 kPa
Diastolic pressure, P_d	10.933 kPa
External pressure, P_ext	0
Outflow pressure, P_out	0
Windkessel resistance, R_1	$2.4875 \cdot 10^8$ Pa s m^{-3}
Windkessel compliance, C	$1.7529 \cdot 10^{-10}$ m^3 Pa^{-1}
Windkessel resistance, R_2	$1.8697 \cdot 10^9$ Pa s m^{-3}

Table 2: Model parameters of the common carotid artery taken from [57]. The resulting wave speed at mean pressure is $c_\mathrm{m} = 6.74$ m s^{-1}.

4.3 ThoA

The thoracic aorta from the aortic root to the descending aorta is simulated as a single vessel with uniform properties coupled to a three-element lumped parameter model of the rest of the systemic circulation [57]. The parameters of this model are displayed in Table 3. The initial area $A_0 = 3.0605$ cm^2 that yields the reference diastolic area $A_\mathrm{d} = 4.5239$ cm^2 at $P = P_\mathrm{d} = 9.4\hat{6}$ kPa is calculated using Eq. (61).

Property	Value
Length, L	24.137 cm
Radius at diastolic pressure, r_d	1.2 cm
Wall thickness, h	1.2 mm
Blood density, ρ	$1,060$ Kg m^{-3}
Blood viscosity, μ	4 mPa s
Velocity profile order, ζ	9
Young's modulus, E	400.0 kPa
Diastolic pressure, P_d	9.4666666666 kPa
External pressure, P_ext	0
Outflow pressure, P_out	0
Windkessel resistance, R_1	$1.1752 \cdot 10^7$ Pa s m^{-3}
Windkessel compliance, C	$1.0163 \cdot 10^{-8}$ m^3 Pa^{-1}
Windkessel resistance, R_2	$1.1167 \cdot 10^8$ Pa s m^{-3}

Table 3: Model parameters of the upper thoracic aorta taken from [57]. The resulting wave speed at mean pressure is $c_\mathrm{m} = 5.17$ m s^{-1}.

4.4 AoBif

Before considering a complete network of arteries, we simulate the abdominal aorta branching into the two iliac arteries as a symmetric, single-bifurcation model [57]. Both iliac arteries are coupled to a three-element lumped parameter model of the rest of the systemic circulation. This test case verifies the ability of each scheme to deal with multiple reflections generated at a junction, where continuity and compatibility conditions are imposed (Section 3.7.2). The parameters of this model are shown in Tab. 4. Initial areas are calculated using Eq. (61).

Property	Aorta	Iliac
Length, L	8.6 cm	8.5 cm
Radius at diastolic pressure, r_d	0.86 cm	0.60 cm
Wall thickness, h	1.032 mm	0.72 mm
Blood density, ρ	$1,060$ Kg m^{-3}	
Blood viscosity, μ	4 mPa s	
Velocity profile constant ζ	9	
Young's modulus, E	500.0 kPa	700.0 kPa
Diastolic pressure, P_d	9.4666666666 kPa	9.4666666666 kPa
External pressure, P_ext	0	0
Outflow pressure, P_out	–	0
Windkessel resistance, R_1	–	$6.8123 \cdot 10^7$ Pa s m^{-3}
Windkessel compliance, C	–	$3.6664 \cdot 10^{-10}$ m^3 Pa^{-1}
Windkessel resistance, R_2	–	$3.1013 \cdot 10^9$ Pa s m^{-3}

Table 4: Model parameters of the human aortic bifurcation taken from [57]. The resulting wave speed at mean pressure is $c_\mathrm{m} = 6.26$ m s^{-1} in the abdominal aorta and $c_\mathrm{m} = 7.35$ m s^{-1} in both iliac arteries.

4.5 Benchmark (in vitro)

We simulate the arterial tree presented in Matthys *et al.* [26], for which *in vitro* pressure and flow measurements were acquired at multiple locations. The tree is made up of 37 silicone vessels representing the largest central systemic arteries of the human vascular system. At the inlet of the ascending aorta, the flow rate measured *in vitro* is prescribed as the inflow boundary condition. Terminal vessels are coupled to single resistors that are simulated as single-resistance terminal models. The 1-D governing equations are solved using the tube law given by Eq. (8) with $A_{\mathrm{d}} = A_0$ and $P_{\mathrm{d}} = 0$. General parameters of this model are given in Table 5. A complete set of parameters is listed in Table 18, and topology is illustrated in Fig. 3

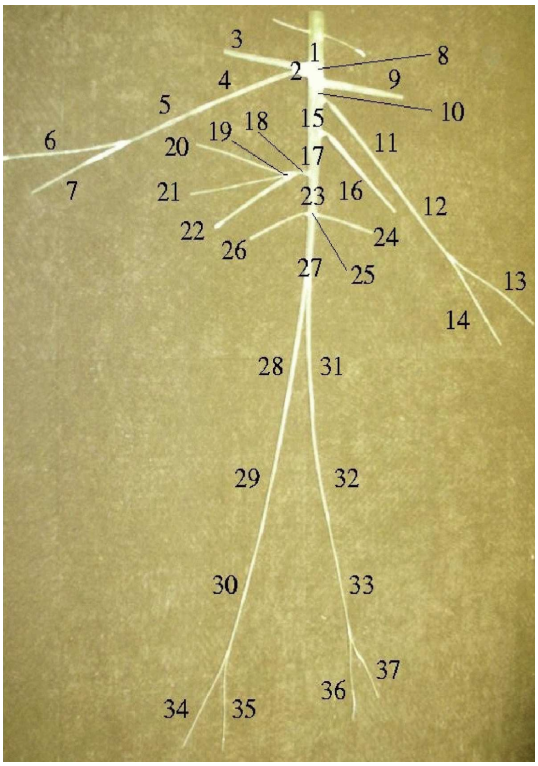

Figure 3: Topology of the *Benchmark (in vitro)* model adapted from Matthys *et al.* [26] (see Table 18)

Property	Value
Blood density, ρ	$1,050$ Kg m^{-3}
Blood viscosity, μ	2.5 mPa s
Velocity profile order, ζ	9
Young's modulus, E	1.2 MPa
Diastolic pressure, P_{d}	0
External pressure, P_{ext}	0
Outflow pressure, P_{out}	432.6 Pa

Table 5: General model parameters of the benchmark model taken from [26].

4.6 Benchmark (ADAN55 model)

The last benchmark model considered to test 1-D numerical schemes is a reduced version of the anatomically-detailed arterial network (ADAN) model developed by Blanco *et al.* [10, 12]. The model contains the largest 55 vessels of the human arterial system (an artery is composed by more than one segment), as described in [12]. Hereafter, we refer to this model as *ADAN55*. Wall thickness is calculated using the following empirical expression [12]

$$h = R_0\left[\tilde{a}\exp\left(\tilde{b}R_0\right) + \tilde{c}\exp\left(\tilde{d}R_0\right)\right], \tag{62}$$

where R_0 is the reference radius (related to A_0) , $\tilde{a} = 0.2802$, $\tilde{b} = -5.053$ 1/cm, $\tilde{c} = 0.1324$ and $\tilde{d} = -0.1114$ 1/cm. The rest of the parameters of the model are presented in Table 6. This model is not exactly as in [12], because the tube law is different. In the present case, Young moduli are constant throughout the arterial network and the tube law is given by Eq. (8) with $A_{\rm d} = A_0$ and $P_{\rm d} = P_0 = 10$ kPa.The initial conditions are $(A(x,0), U(x,0), P(x,0)) = (A_0(x), 0, P_0)$ A complete set of parameters is listed in Tables 19 and 20.

Property	Value
Blood density, ρ	$1,040$ Kg m^{-3}
Blood viscosity, μ	4.0 mPa s
Velocity profile order, ζ	2
Young's modulus, E	225 kPa
Diastolic pressure, $P_{\rm d}$	10 kPa
External pressure, $P_{\rm ext}$	0
Outflow pressure, $P_{\rm out}$	0

Table 6: Model parameters of the ADAN55 model [12]. Arterial compliance was redefined [12] to be consistent with the present linear tube law.

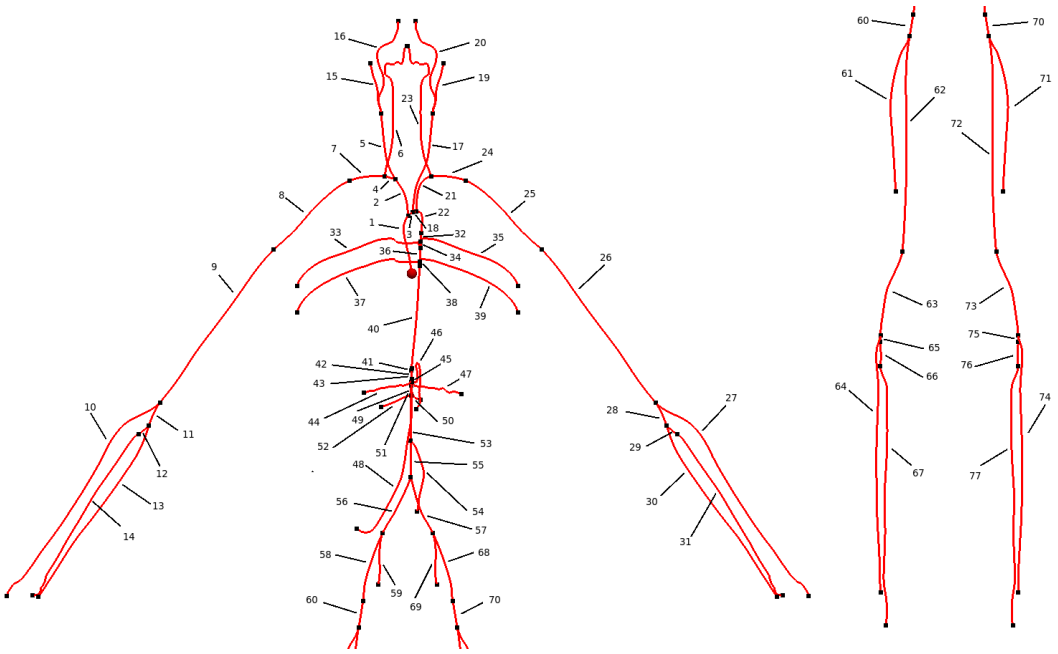

Figure 4: Topology of the *ADAN55* model (see Tables 19 and 20 for details).

4.7 Steady Flow in a single vessel with narrowing in the middle

The parameters of this model are the same as in the single-pulse model, except from a narrowing to half the area between four and six meters. I consider a continous narrowing, by using two half sine functions, and also by separating the vessel into three segments. The flow is set constant at the inlet with value 100 ml/s. The distal boundary condition is a single resistance element with $R = 10^8$ Pa s/m^2 . The geometries are presented in Fig. 5, and properties in Table 7.

Property	Left section	Middle section	Right section
Length, L	4 m	2 m	4 m
Radius at diastolic pressure, r_{d}	1 cm	0.707 cm	1 cm
Wall thickness, h	1.5 mm	1.5 mm	1.5 mm
Blood density, ρ	$1,050$ Kg m^{-3}		
Blood viscosity, μ	0 mPa s		
Velocity profile constant ζ	NA		
Young's modulus, E	400.0 kPa	400.0 kPa	400.0 kPa
Diastolic pressure, P_{d}	0 kPa	0 kPa	0 kPa
External pressure, P_{ext}	0 kPa	0 kPa	0 kPa
Outflow pressure, P_{out}	–	–	0
Resistance, R	–	–	$1 \cdot 10^8$ Pa s m^{-3}

Table 7: Model parameters of long narrowing vessel with constant flow as described in Sect. 4.7. notice that two cases are considered; a continous narrowing (one vessel with narrowing constructed by half sine functions) and a discontinous narrowing (three vessels). See Fig. 5. The vessels have compliance models that govern wavespeed and give the problem a hyperbolic nature, however the area is set constant.

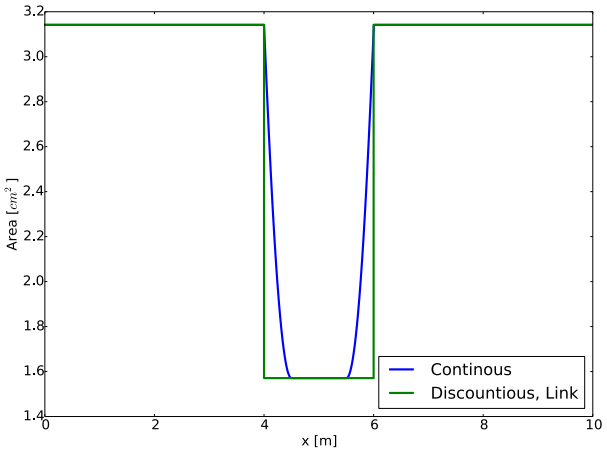

Figure 5: Figure showing the geometries associated with test 4.7. The area in the middle is half of the area in the start and end section, which is π cm^2. The continous case is constructed by five smooth curves; 1, straight line from $x = 0$m to $x = 4$m; 2, half sine from $x = 4$ m to $x = 4.5$m; 3, straight line from $x = 4.5$m to $x = 5.5$m; 4, half sine from $x = 5.5$m to $x = 6$m; 5, straight line from $x = 6$m to $x = 10$m. The Discontinous case is constructed by linking three single vessels; 1, single vessel with area πcm^2, from $x = 0$m to $x = 4$m; 2, single vessel with area $\pi/2$cm^2, from $x = 4$m to $x = 6$m; 3, single vessel with area πcm^2, from $x = 4$m to $x = 6$m.

4.8 Constant Flow in symmetric and asymmetric single-bifurcation

In this test I consider two single bifurcations with constant flow. The first of whom is a symmetric bifurcation with parameters akin to those in the previous test, but now considering a bifurcation rather than a link. The mother vessel is one meter long and have constant crossectional area of $A_m = \pi$ cm^2. The two daughter vessel are also one meter and have constant crossectional area of $A_l = A_r = \frac{A_m}{4} = \frac{\pi}{4}$ cm^2. The flow is set constant at the inlet with value 100 ml/s. The distal boundary condition of both daughter vessels is a single resistance element with $R = 10^8$ Pa s/m^2 . The geometries are presented in Fig. 6, and parameters in Table 8.
Secondly I consider an asymmetric bifurcation, where the mother- and left daughter-vessel, inlet and outlet boundary boundary conditions are equal to the symmetric case. However in this case the right daughter vessel has a constant area of $A_r = \frac{A_m}{8} = \frac{\pi}{8}$ cm^2. Parameters are listed in Table 9, and geometry is illustrated in Fig. 7

Property	Mother	Daughters
Length, L	1 m	1 m
Radius at diastolic pressure, r_d	1 cm	0.5 cm
Wall thickness, h	1.5 mm	1.5 mm
Blood density, ρ	$1,050$ Kg m^{-3}	
Blood viscosity, μ	0 mPa s	
Velocity profile constant ζ	NA	
Young's modulus, E	400.0 kPa	400.0 kPa
Diastolic pressure, P_d	0 kPa	0 kPa
External pressure, P_ext	0	0
Outflow pressure, P_out	–	0
Resistance, R	–	$1 \cdot 10^8$ Pa s m^{-3}

Table 8: Model parameters of the symmetric bifurcation with constant flow as described in Sect. 4.8. The vessels have compliance models that govern wavespeed and give the problem a hyperbolic nature, however the area is set constant.

Property	Mother	L. daughter	R. daughter
Length, L	1 m	1 m	1 m
Radius at diastolic pressure, r_d	1 cm	0.5 cm	0.354 cm
Wall thickness, h	1.5 mm	1.5 mm	1.5 mm
Blood density, ρ	$1,050$ Kg m^{-3}		
Blood viscosity, μ	0 mPa s		
Velocity profile constant ζ	NA		
Young's modulus, E	400.0 kPa	400.0 kPa	400.0 kPa
Diastolic pressure, P_d	0 kPa	0 kPa	0 kPa
External pressure, P_ext	0 kPa	0 kPa	0 kPa
Outflow pressure, P_out	–	0	0
Resistance, R	–	$1 \cdot 10^8$ Pa s m^{-3}	$1 \cdot 10^8$ Pa s m^{-3}

Table 9: Model parameters of the asymmetric bifurcation with constant flow as described in Sect. 4.8. The vessels have compliance models that govern wavespeed and give the problem a hyperbolic nature, however the area is set constant.

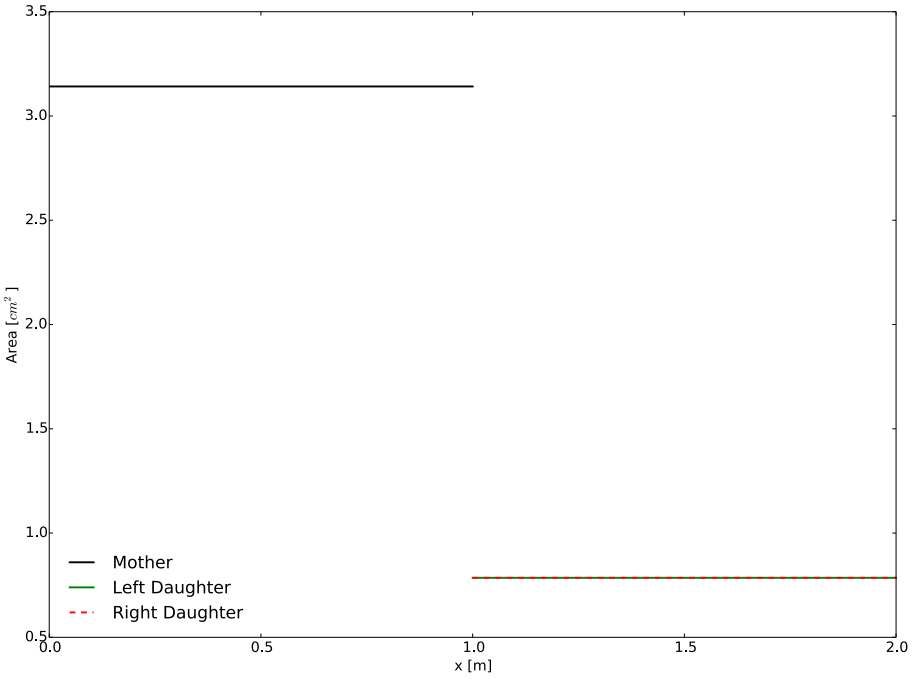

Figure 6: Showing the geometries associated with test 4.8. A single symmetric bifurcation. Mother vessel with constant area of πcm^2; Two equal daughter vessels with constant area $\frac{\pi}{4}\text{cm}^2$.

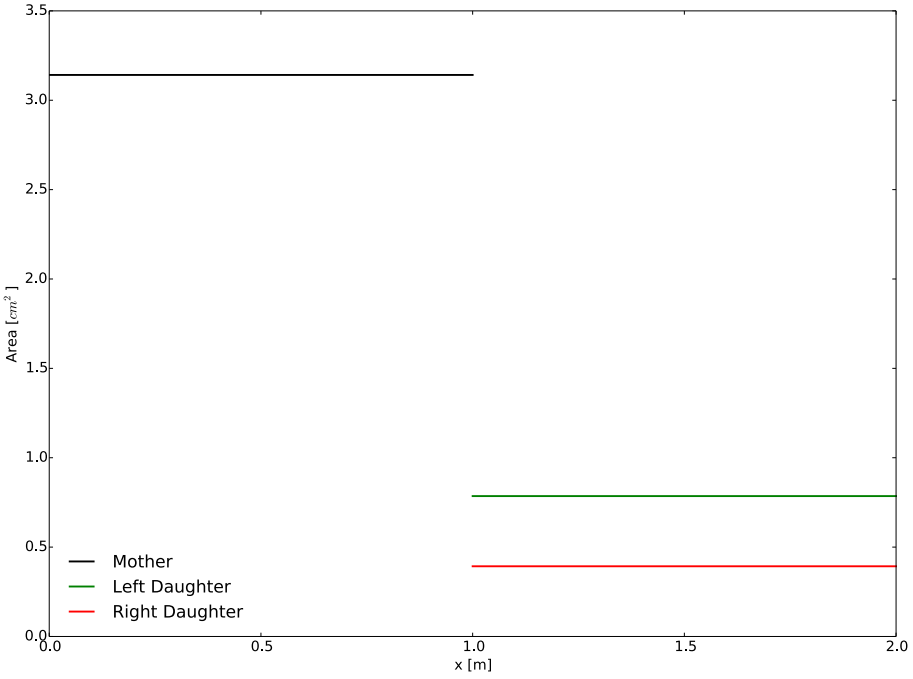

Figure 7: Showing the geometries associated with test 4.8. A single asymmetric bifurcation. Mother vessel with constant area of πcm^2; Two daughtervessels with constant area of $\frac{\pi}{4}\text{cm}^2$ and $\frac{\pi}{8}\text{cm}^2$ respectively.

5 Process

The first part of this Master Thesis delt with getting (better) to know with STARFiSh and to set up the test cases described in Sect. 4. The preliminary deadline for performing the tests in Coparison1Dscheme was set to April 1st. However the 3D and Experimental data for Comparison in tests 4.2 to 4.5 were not obtained before march 16th, which slowed down the process of validating and optimizing the tests. As will be seen in Sect. 6 the final solutions with the original implementation of STARFiSh were not satisfying in all tests. The Process of finding the reason for the big discrepancies in the STARFiSh solutions proved a cumbersome one. For every strange result, the natural thing to do is to check your own procedures, once, twice, three, four or more times, before looking into other solutions. After easter a problem-solving period started. For better understanding of the methods used in STARFiSh, test 4.1 to 4.3 were programmed in mini-solvers on my own personal computer, where BCs, and Riemann invariants were added adaptively. Finally a version which also included Womersley theory was made. The solving schemes in all these minisolvers were based on the Fluxbased method given by Eq. 39 and Eq. 40

6 Grid-adaption

In this section the effect of changing CFL number, Δt and amount of nodes is presented. In the following sections the term Flux refers to field equations being solved according to Eq. 39 and Eq. 40, whereas Matrix refers to field equations being solved according to Eq. 35. Linear link/bifurcation model refers to model based on continuity of static pressure, whereas nonlinear model referes to link/bifurcation model based on continuity of total pressure, as described in Sect. 3.7.2. Thus, naturally six different combinations evolve:

combination 1 Flux based scheme, Singlevessel

combination 2 Matrix based scheme, Singlevessel

combination 3 Flux based scheme, and nonlinear link/bifurcation model

combination 4 Flux based scheme, and linear link/bifurcation model

combination 5 Matrix based scheme, and nonlinear link/bifurcation model

combination 6 Matrix based scheme, and linear link/bifurcation model

It should be noted that the results (in this section) presented for test 4.1 to 4.3 were all performed with combination 2. As will be seen in the following sections, I argue that combination 1 is more numerically correct. However it is believed that the same tendencies in CFL number, Δt and amount of nodes is also valid for combination 1. The gridadption for test 4.4 and 4.5 were performed with combination 6, even though I later argue that combination 3 is numerically and physiologically more correct. The gridadaption for test 4.6 were all performed with combination 3. The results from this Section form the basis for the grid, and Δt values used in the final STARFiSh (McC) solutions in Comparison1Dscheme.

6.1 Propagation of a single pulse in a straight vessel

The inflow has a width of approximately 0.05 s and an initial wave speed of $c_0 = 6.17$ m s^{-1}, giving a wavelength of about $c_0 T \approx 31$ cm. This is a short wavelength comparing with the length of the vessel.
Fig. 8 show the pulse as it has propagated for 1.5 s. Different CFL and Δt values are compared. It is clear that this test requires CFL numbers close to one in order to avoid diffusive and dispersive errors. When assuring CFL number close to one, diffusive and dispersive errors are relatively small, even at high Δ t values. The Δt value chosen in this test is 0.5 ms, with 3201 nodes, giving a CFL number of 0.99. The Simulation time for this test was 0.36 seconds.

6.2 CCA

In Appendix B (B) a series of tables with error metrics (relative to 3D data), for different Δt values, grid-nodes, and CFL number is shown. All simulations in were initialized with a constant pressure of Pd, to try to reach steady state solution fast. It should be noted that Table 21 contain error metrics calculated after just 3 cycles, whereas Table 22 and 23 were calculated in its 8 th cycle, which could cause some inconsistency. Nevertheless, some concluding remarks could be made. This test has a much higher wavelength than the previous test. An approximate wavelength based on the period of the systolic inflow is $l = c_\mathrm{m}/f = c_\mathrm{m} T \approx 2.7m$, with period $T \approx 0.4$, and wave speed at mean pressure $c_\mathrm{m} = 6.74$ m s^{-1}. This indeed is much longer than

(a) $\Delta t = 0.8$ ms

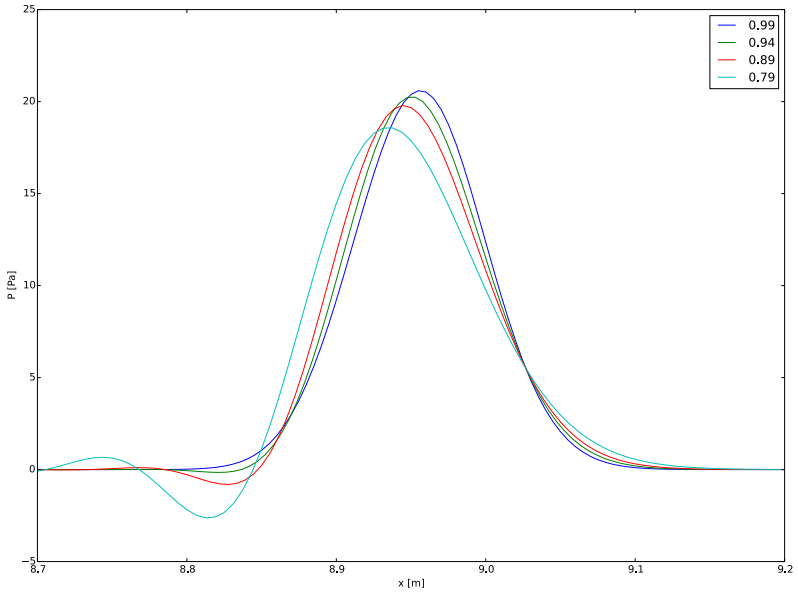

(b) $\Delta t = 0.4$ ms

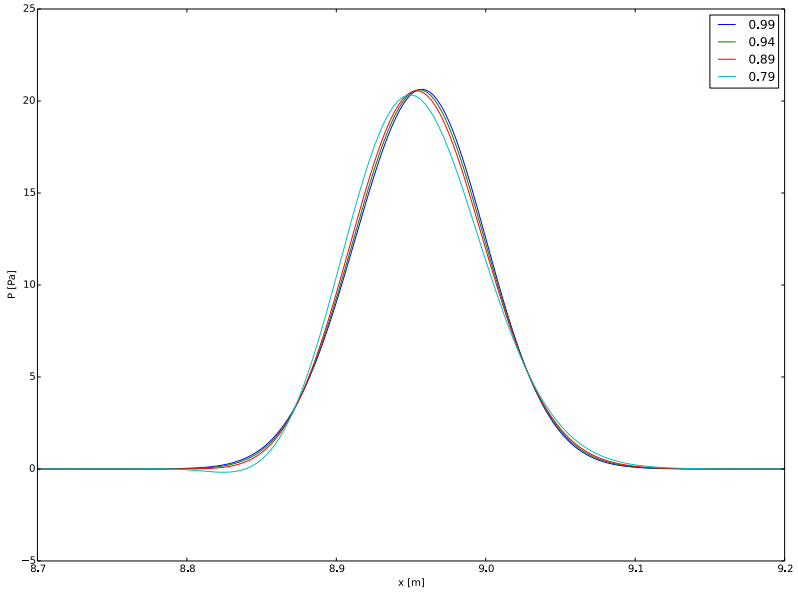

Figure 8: Showing the effect on changing the CFL number in the single-pulse model. The figures show the pulse at t=1.5 s. All simulations in the top figure have Δt of 0.8 ms, and the number of Nodes to achieve CFL numbers of 0.99, 0.94, 0.89 and 0.79 is 2001, 1901, 1801 and 1601 repectively. All simulations in the bottom figuere have Δt of 0.4 ms, and the number of Nodes to achieve CFL numbers of 0.99, 0.94, 0.89 and 0.79 is 4001, 3801, 3601 and 3201 repectively. From the graphs it is clear that diffusive (loss in amplitude), and dispersive(change in phase) errors occur if the CFL number is not very close to 1 in this short wave test. It is also clear that the effect is enhanced at higher Δt values

in the first test, and from table 21, 22 and 23 one can see that diffusive and dispersive errors are not as sensitive on the CFL number, as in the first test. Also the errors when increasing Δt is not very big. A satisfying solution is found by using a Δt value of 0.5 ms, CFL number of 0.87 and 33 grid-nodes.

6.3 ThoA

For the ThoA test a series of tables with error-metrics relative to 3D data is presented in Appendix B. As was the case in the previous case, the error metrics in Table 24 were calculated after 8 cycles, whereas the error metrics in Table 25 and 26 were calculated after 20 cycles. An approximate wavelength based on the period of the systolic inflow is $l = c_{\mathrm{m}}/f = c_{\mathrm{m}}T \approx 1.8m$, with period $T \approx 0.35$, and wave speed at mean pressure $c_{\mathrm{m}} = 5.17$ m s^{-1}. This is also relatively long, and reflected in that low CFL numbers do not constitute large errors. In table 25, and 26 it almost seems as low CFL number give rise to lower error metrics. This is sort of a paradox, but as can be seen from Fig. 9, very low CFL numbers coincide with non physiological oscillations. Table 25, and 26 also show that increasing Δt does not critically increase the errors. The chosen Δt, CFL number and grid-node for this test is, 0.5, 0.35 and 35 respectively.

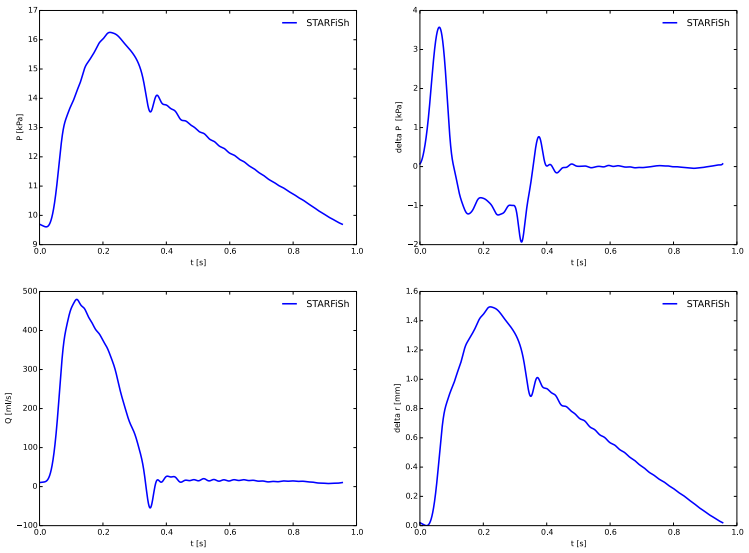

Figure 9: Showing pressure (top left), pressure gradient (top right), flow (bottom left), and change in radius (bottom right), for 1D MacCormack (STARFiSh)in Thoracic aorta test. Simulation with only 5 nodes, and a resulting maximum CFL number of only 0.04 give rise to nonphysiological oscillations, noticable in diastole.

6.4 AoBif

Also with the AoBif test, a series of tables with error-metrics relative to 3D data is presented in Appendix B. The trends are similar to those in the previous two cases. Long wavelength means that relatively low CFL numbers can be tolerated, and increasing Δt does not critically increase the errors. The error metrics in Table 27 were calculated after 8 cycles, whereas the error metrics in Table 28 and 29 were calculated after 25 cycles. The chosen Δt, maximum CFL number (Iliac artery), and grid-nodes (all arteries) in this test is, 0.5 ms, 0.53 cm and 13.

6.5 Benchmark

Similar tests were on the Benchmark test, however the results are not presented in this Thesis. Comparing with the experimental data, increasing the numerical parameters (Δt and Δx) did not critically increase the error-metrics. However noticeable differences between the other schemes occurred by increasing the numerical parameters. Also worth noting is that the Solutions in this test have relatively high frequent waveforms. As a result a relatively high CFL number was chosen. The final numerical parameters were chosen to be $\Delta t = 0.25$ ms, $\Delta x = 0.18$ cm and CFL number of 0.7.

6.6 Adan55

Fig. 10a show the dependence on changing CFL/Δt values for the Adan55 model. Corresponding numerical parameters are given in Table 10. The figure show pressure waveforms through the aorta segments at systole (t/T=0.2 s). In contrast to the previous physiological tests, the dependence on grid seem more important here. However this is believed to be related to the bifurcation/link model rather than to CFL number and order of accuracy in solving of field equations. One difficulty with this test is that it has some very short vessels. In order to calculate the field equations, at least three nodes are needed. Looking at Fig. 10a this behaviour is present in the interface between the longest vessel, aorta 9 (Id 40), and shortest vessel aorta 10 (ID 41). Aorta 9 is the vessel furthest to the left in Fig. 10b. Aorta 10 is the shortest vessel just to the right of aorta 9, and as can be seen the solution with only two nodes (MacCormack643) in aorta 10 have increasing pressure with increasing distance (x). As the nodes in this vessel increase the solution seem to converge more or less to the DCG solution. As will be seen in later sections the DCG scheme coincide with most of the other state of the art numerical schemes, and thus is a good reference. Another thing to notice is that this grid-dependence does not seem to be present in the DCG scheme and many of the other schemes, and only two or a few nodes in aorta 10 seem to suffice. The reason for this is not certain, and more tests should be run to figure this out. However some thoughts around this have been made. In the implementation of the nonlinear link/bifurcation model the pressure and flow is discretized with Riemann invariants and thus only three equations and three unknowns are solved for. This should automatically satisfy continuity of propagating characteristic variables. However looking at simulation 643MacComack in Fig. 10a and 10b in aorta 11, the solutions at the boundary does not seem to form a nice smooth curve coinciding with the field solution. The other schemes seem to have smoother solutions. Thus a question arises; is continuity of characteristic variables really satisfied? And if not, why so? Some thought and possible reasons for this is Discussed in Sect. 8.1.4.

Another problem that was encountered in this test was the setting of the parameters for the tube law. In the first few tests the vessel wall-thickness was calculated according to Eq. 62, with R_0 chosen as the proximal radius(constant wall-thickness in each vessel). This had some interesting effects, noticeable in certain links. This tests has some vessels that are segmented into two or more vessels, even though they have continuously decreasing radius. Aorta 9 and Aorta 10 is an example of such a vessel. Fig. 11a, show how aorta 9 and aorta 10 behave as two discontinuous vessels if parameters are set according to $R_{proximal}$. Fig. 11b on the other hand show how aorta 9 and 10 behave as one continuous vessel, when the wall-thickness is calculated according to $R_0(x)$ (tapering included in vessel wall-thickness). The final solution chosen as STARFiSh contribution in Comparison1Dscheme was MacCormack642, with tapering included in calculation of wall-thickness. This simulation was chosen since it has a fine balance between

accuracy and amount of nodes. Later findings proved that using a Δt value of 0.1 ms, the same amount of nodes giving an average CFL number of 0.32 yields a solution closer to the other schemes. Thus once again, the solution is not sensitive to low CFL numbers. The error is directly related to Δt.

simulation	Δt [ms]	CFL number	note
MacCormack631	0.2	0.6-0.9	
MacCormack633	0.1	0.6-0.9	high CFL number in short vessels, lower in longer vessels
MacCormack637	0.2	0.6-0.9	high CFL number in short vessels, lower in longer vessels
MacCormack642	0.25	0.8	constant CFL number
MacCormack643	0.25	0.5	constant CFL number

Table 10: Showing Δt values and CFL numbers for simluations corresponding to Fig. 10.

(a) All segments

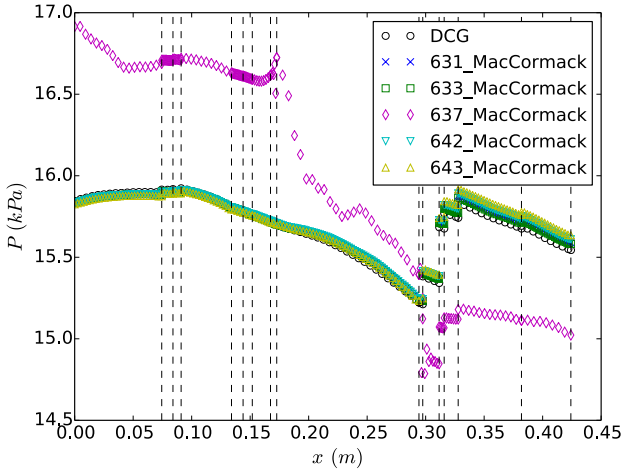

(b) close up of aorta 9, 10, 11, 12 and 13

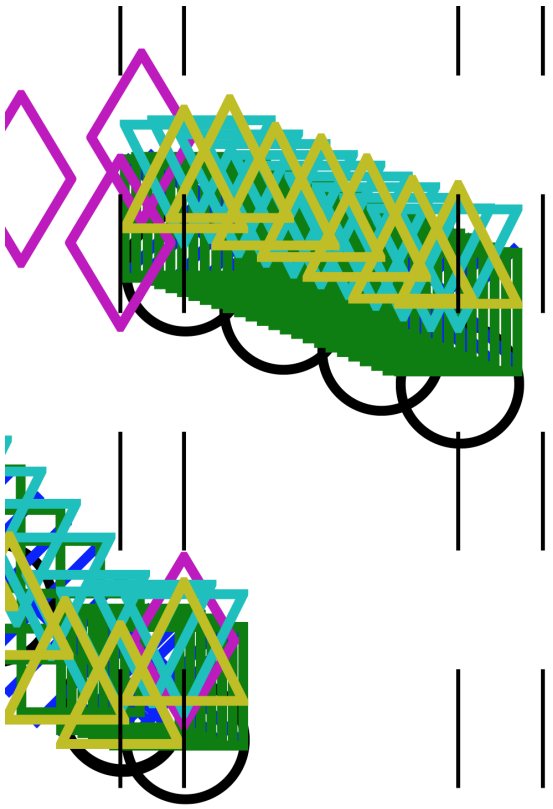

Figure 10: Showing the dependence on gridnodes and or Δt. The figure show pressure waveforms through the aorta segments at systole (t/T=0.2 s). The CFL numbers, and Δt values of this figure is listed in Table 10. All simluations are performed with parameters for the tube law given by Eq. 62, with $R_0 = R_0(x)$ (tapering also included in wallthickness). The behaviour at the vessel segment interface is griddependent. Also noticable is that STARFiSh solutions does not seem to form as nice smooth curves connecting boundary and field nodes as the other schemes.

(a) Discontinous

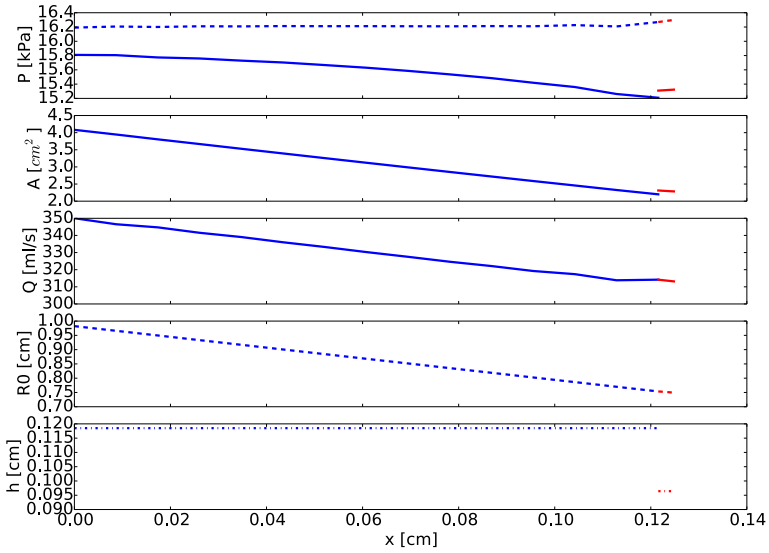

(b) Continous

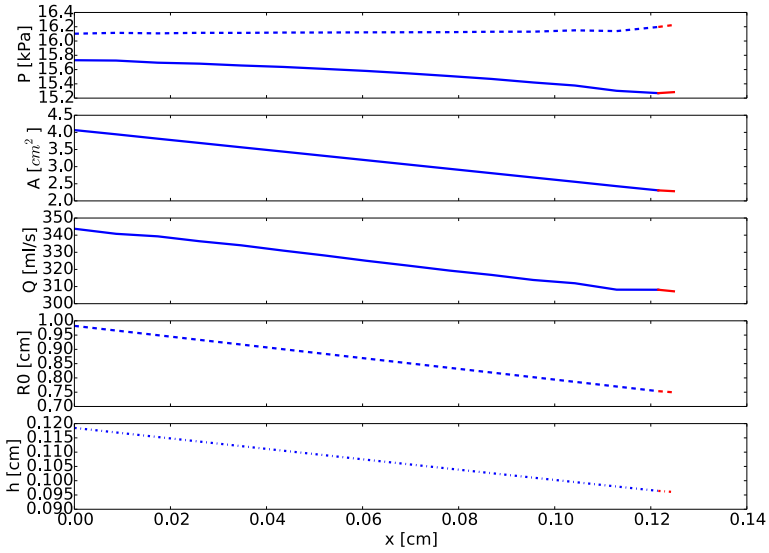

Figure 11: Showing static and total (dotted line) pressuer (top), area, volumetric flow, initial radius and wallthickness (bottom), for aorta 9 (blue line) and aorta 10 (red line), as a function of x in adan 55 model at time t/T=0.2 s. The wallthickness in the top simulation is not continous, resulting in discontinuities in area at the vessel interface (different pressure area relation). The wallthickness in the bottom simulation is continous. Thus the area at the vessel interface is equal throughout the period.

7 Results: STARFiSh and Womersley

This section shows the results from the tests presented in Sect. 4. The section is subdivided into Sect. 7.1, and Sect. 7.2. Sect. 7.1 contains results from tests with different methods and feautures within STARFiSh only. Sect. 7.2 contain results on Womersleytheory.

7.1 STARFiSh

Unless otherwise stated all STARFiSh simulations presented in this section have Δt, and Δx as described in Sect. 6, Grid-adaption. This can also be found in Table 33, which in addition show Δt, and Δx for any other scheme's solution presented here.

7.1.1 Propagation of a single pulse in a straight vessel

This test proved to take quite a bit of time due to an implementation error in the MacCormack scheme. Fig. 12 shows the pulse propagating through the first few nodes of the vessel, and as can be seen a quite substantial loss of peak flow is present from node zero to node one. The problem proved to simply be that in the MacCormack scheme the value of the predicted values at node zero was chosen to be the value U_0^n rather than calculated as given by Eq. 35. The error caused both loss in flow, pressure and also introduced dispersive errors.

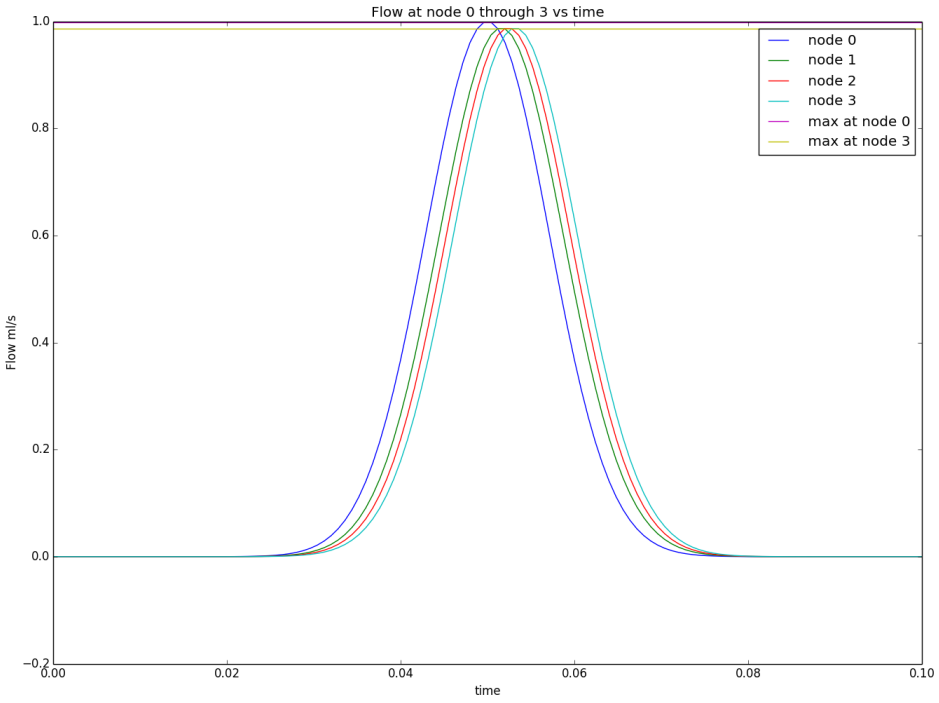

Figure 12: Showing the effect of an implementation error in the original MacCormack scheme. A quite substantial loss of Flow from node zero to node one is present, due to wrong handling of predicted values of boundaries in MacCormack scheme.

In this section I also present a comparison of the corrected Matrix formulation (combination 2), with the new Flux formulation, (combination 1) . Fig. 13 show a comparison of the original Matrix formulation of the MacCormack scheme given by Eq. 35 with the new scheme given by

Eq. 39 and Eq. 40. The figure show the pressure pulse at time t = 1.5. The solution from the FEM scheme is plotted for comparison. Both STARFiSh solutions have $\Delta t = 0.5$ ms, and 3201 nodes. Both schemes show very small diffusive errors, whereas it seems that the Matrix formulation introduce some dispersive errors.

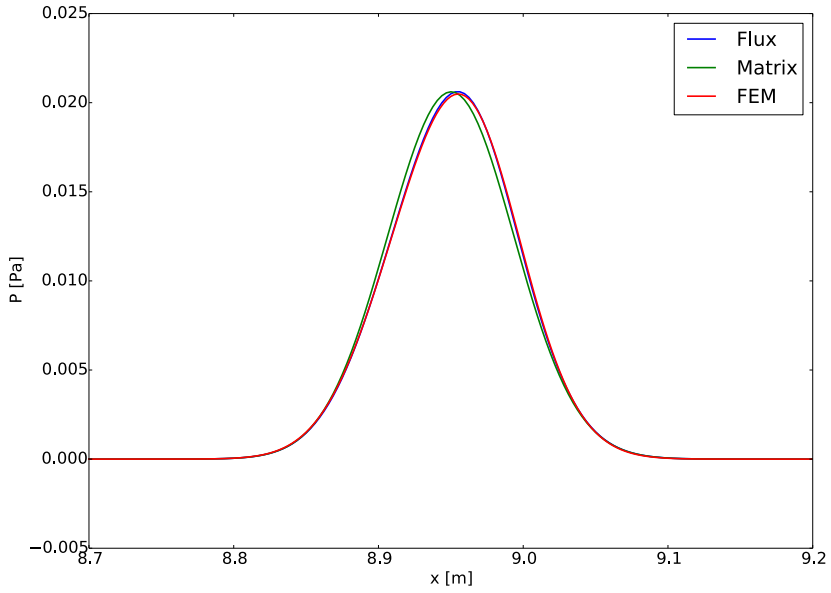

Figure 13: Showing the pressure pulse at time t = 1.5 s comparing the inviscid case of the original Matrix MacCormack scheme (combination 2) with the new Flux based formulation (combination 1). The results from the FEM scheme is also plotted for Comparison.

7.1.2 CCA

In this section different features of STARFiSh are tested and compared with each other in a test replicating the Common Carotid artery. 3D data and some of the other state of the art flow-solvers are also present for better visualization. McCMatrix1 is combination two with convective correction factor equal to one ($1 \rightarrow \alpha = 1$). McCFlux1 is combination one with convective correction factor equal to one. McCMatrixa is combination two with convective correction factor calculated according to Eq. 4 ($\text{a} \rightarrow \alpha = \frac{(\zeta+2)}{(\zeta+1)}$). The results are presented in Fig. 14 and Table 11. The difference between the STARFiSh solutions are small. The waveforms are very similar, but the McC solution seem to have the best error metrics. The only noticable difference is visible in the Pressure Gradient. Here one may observe that the Flux method is more in accordance with the other Schemes. There is also a slight difference between using convective correction factor equal to one, and calculating it based on the assumed Poiseuille flow velocity-profile.

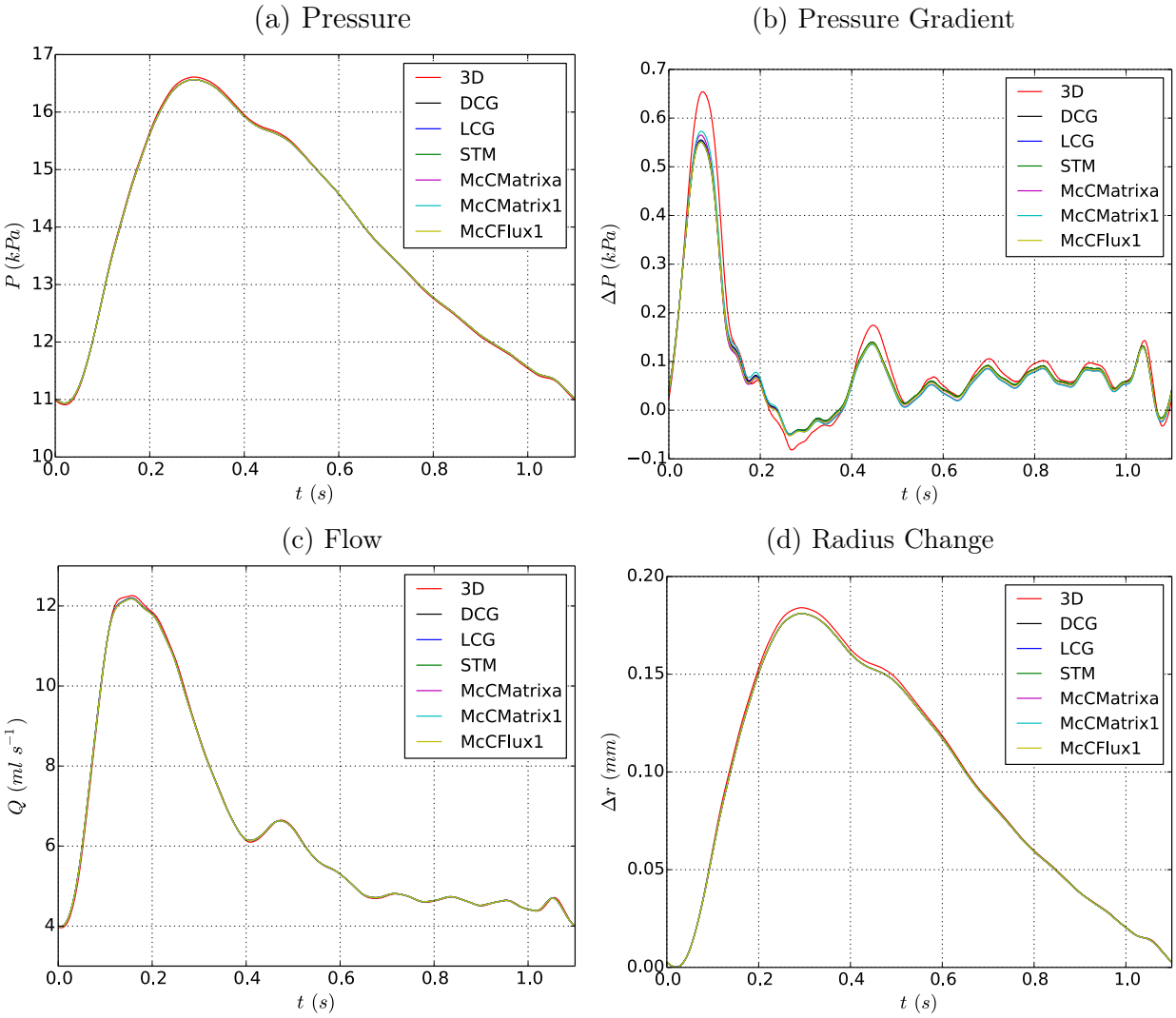

Figure 14: Common carotid artery. Pressure (a), pressure gradient between inlet and outlet (ΔP) (b), flow rate (c), and change in radius from diastole (d) with time at the midpoint of the vessel. Results are shown for three different STARFiSh solutions (See text description in Sect. 7.1.2), three other 1-D numerical schemes and the 3-D model from [57]. The model parameters are shown in Table 2 and the error calculations in Table 11.

7.1.3 ThoA

In this section different features of STARFiSh are tested and compared with eachother in the test replicating the Thoracic Aorta. 3D data and some of the other state of the art flowsolvers are also present for better visualization. MacCMatrix1 is combination two with convective correction factor equal to one. McCFlux1 is combination one with convective correction factor equal to one. MacCMatrixa is combination two with convective correction factor calculated according to Eq. 4. The results are presented in Fig. 15 and Table 12. The difference between the STARFiSh solutions are bigger than in the previous case. The waveforms are different especially looking at the flow and pressure gradient. The McCFlux seem more in accordance with the other schemes, and have the best error-metrics. There is also a slight difference between using convective correction factor equal to one, and calculating it based on the assumed power law ($\zeta = 9$) velocity-profile, visible in the pressure gradient (MacCMatrix1 vs MacCMatrixa).

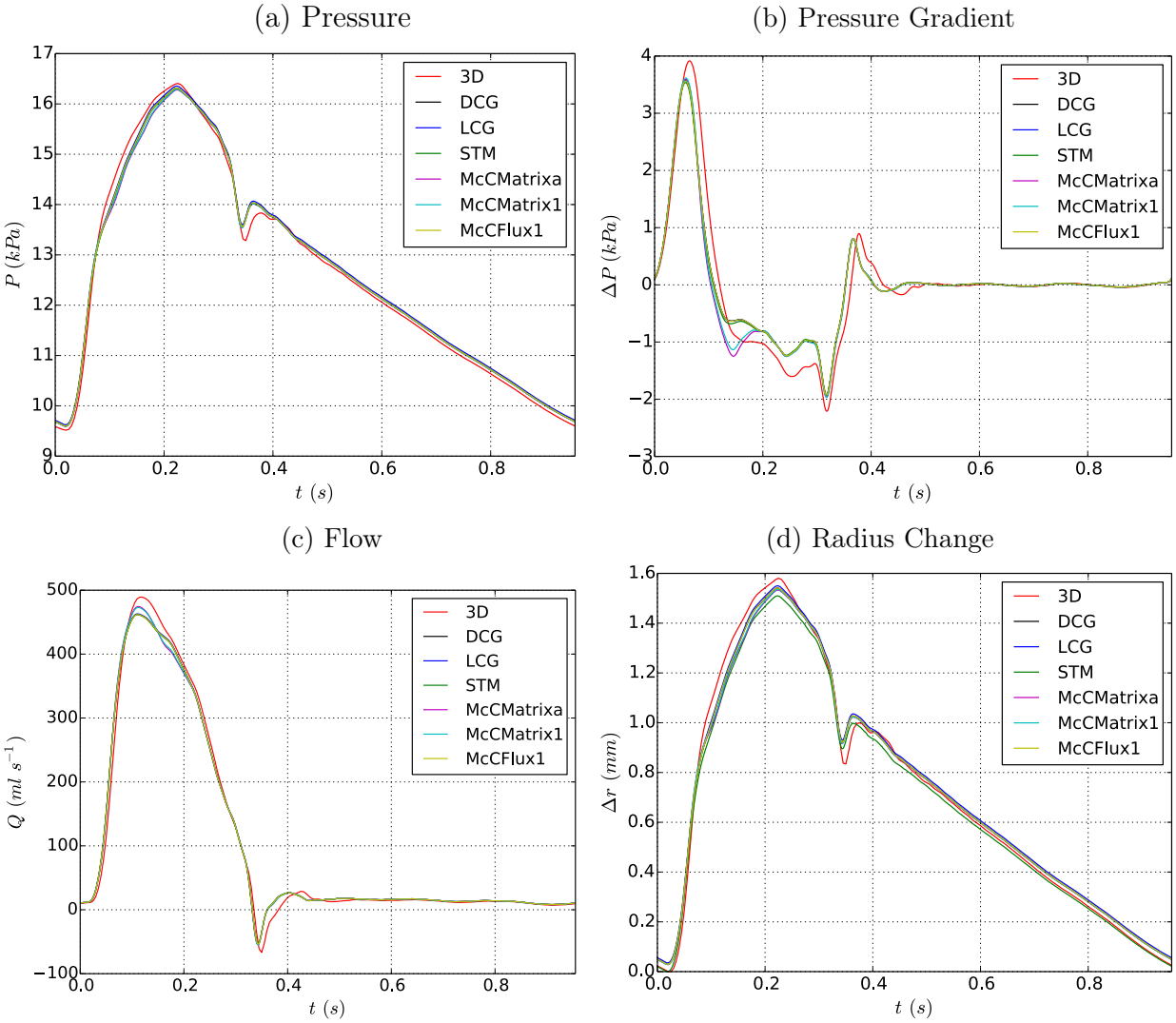

Figure 15: Upper thoracic aorta. Pressure (a), pressure gradient between inlet and outlet (b), flow rate (c), and change in radius from diastole (d) with time at the midpoint of the vessel. Results are shown for three different STARFiSh solutions (See text description in Sect. 7.1.3), three other 1-D numerical schemes and the 3-D model from [57]. The model parameters are shown in Table 3 and the error calculations in Table 12.

	CCA					
	DCG	LCG	STM	McCMatrix1	McCFlux1	McCMatrixa
$\mathcal{E}_P^{RMS}$	0.19	0.24	0.24	0.22	0.24	0.23
$\mathcal{E}_Q^{RMS}$	0.39	0.26	0.29	0.29	0.30	0.29
$\mathcal{E}_{\Delta r}^{RMS}$	0.94	1.00	0.98	0.99	1.01	1.01
$\mathcal{E}_{\Delta P}^{RMS}$	4.43	4.35	4.47	3.95	4.47	4.35
$\mathcal{E}_P^{MAX}$	0.30	0.52	0.53	0.46	0.52	0.51
$\mathcal{E}_Q^{MAX}$	1.21	1.02	1.13	1.15	1.20	1.16
$\mathcal{E}_{\Delta r}^{MAX}$	1.68	1.93	1.96	1.80	1.93	1.91
$\mathcal{E}_{\Delta P}^{MAX}$	16.69	16.17	16.90	12.89	16.58	15.39
$\mathcal{E}_P^{SYS}$	-0.26	-0.27	-0.26	-0.26	-0.27	-0.27
$\mathcal{E}_Q^{SYS}$	-0.54	-0.46	-0.55	-0.62	-0.62	-0.64
$\mathcal{E}_{\Delta r}^{SYS}$	-1.62	-1.63	-1.63	-1.61	-1.63	-1.63
$\mathcal{E}_{\Delta P}^{SYS}$	-15.11	-15.37	-15.76	-12.41	-15.73	-13.59
$\mathcal{E}_P^{DIAS}$	0.28	0.28	0.27	0.26	0.28	0.26
$\mathcal{E}_Q^{DIAS}$	0.26	0.22	0.27	0.22	0.23	0.22
$\mathcal{E}_{\Delta P}^{DIAS}$	4.98	4.76	4.85	4.94	4.45	4.66

Table 11: Calculated relative root mean square, maximum, systolic and diastolic errors (%), as defined in Eq. (56), for test case presented in . 4.2, or the common carotid artery (CCA), Fig. 14. Errors are determined at the midpoint of each segment.

	ThoA					
	DCG	LCG	STM	McCMatrix1	McCFlux1	McCMatrixa
$\mathcal{E}_P^{RMS}$	1.08	1.21	1.12	1.14	1.08	1.18
$\mathcal{E}_Q^{RMS}$	2.55	2.19	2.28	2.11	2.22	2.17
$\mathcal{E}_{\Delta r}^{RMS}$	2.30	2.41	2.90	2.52	2.33	2.64
$\mathcal{E}_{\Delta P}^{RMS}$	7.71	7.23	7.52	7.51	7.23	7.96
$\mathcal{E}_P^{MAX}$	3.55	3.55	3.30	3.24	3.27	3.53
$\mathcal{E}_Q^{MAX}$	9.12	7.20	7.40	6.84	7.04	7.12
$\mathcal{E}_{\Delta r}^{MAX}$	7.77	7.67	8.04	7.26	7.09	7.87
$\mathcal{E}_{\Delta P}^{MAX}$	31.86	29.31	31.19	31.70	29.31	34.06
$\mathcal{E}_P^{SYS}$	-0.55	-0.32	-0.59	-0.70	-0.55	-0.77
$\mathcal{E}_Q^{SYS}$	-5.57	-5.36	-5.56	-3.33	-5.58	-3.02
$\mathcal{E}_{\Delta r}^{SYS}$	-2.48	-1.93	-4.48	-2.84	-2.49	-3.00
$\mathcal{E}_{\Delta P}^{SYS}$	-8.97	-8.89	-9.70	-7.66	-9.04	-8.25
$\mathcal{E}_P^{DIAS}$	0.85	1.12	0.85	0.81	0.87	0.80
$\mathcal{E}_Q^{DIAS}$	2.70	2.67	2.95	2.43	2.67	2.45
$\mathcal{E}_{\Delta P}^{DIAS}$	7.28	7.24	7.47	6.23	7.32	6.30

Table 12: Calculated relative root mean square, maximum, systolic and diastolic errors (%), as defined in Eq. (56), for test cases corresponding to Fig. 15, or the upper thoracic aorta (ThoAo). Errors are determined at the midpoint of the segment.

7.1.4 AoBif

In this section different features of STARFiSh are tested and compared with each other in the test replicating an aortic bifurcation. 3D data and some of the other state of the art flow-solvers are also present for better visualization. In Fig. 16 MacCMatrixaL is STARFiSh with Matrix based scheme with linear bifurcation model (L=Linear), and convective correction factor calculated according to Eq. 4 (combination 6), MacCMatrix1N is STARFiSh with Matrix based scheme with nonlinear bifurcation model (N=Non-linear), and convective correction factor set to one (combination 5), McCFlux1N is STARFiSh with Flux based scheme with nonlinear bifurcation model, and convective correction factor set to one (combination 3). In this test the difference between the three is almost indiscernible. Error-metrics are shown in Table 13, for the Junction. Further error metrics for midsection of aorta and iliac may be found in Table 30and 31 in Appendix C. The error-metrics are very similar for all three STARFiSh solutions.

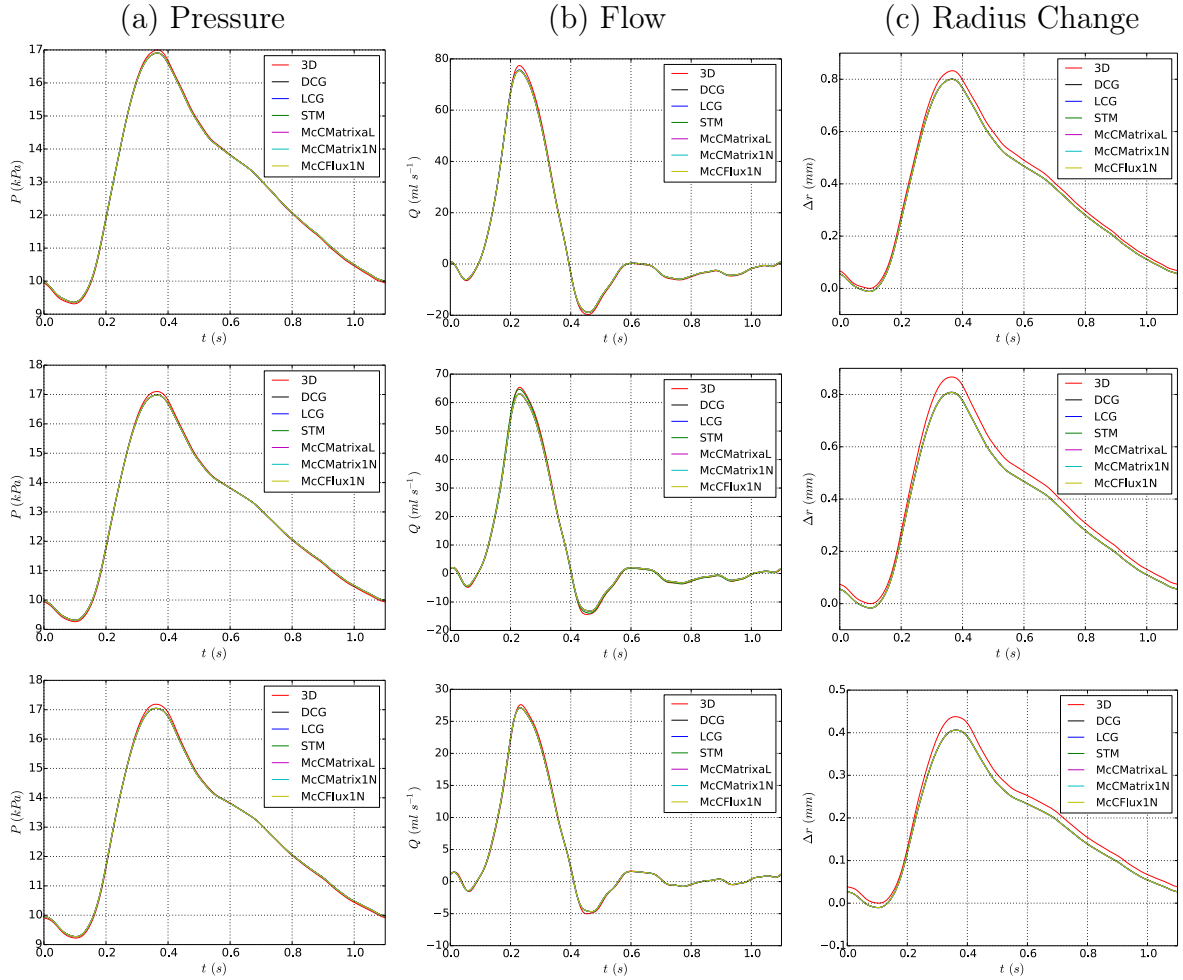

Figure 16: Aortic bifurcation. Pressure (a), flow rate (b), and change in radius from diastole (c) at the midpoint of the aorta (top), end point of the aorta (middle) and midpoint of either iliac artery (bottom). Results are shown for three different STARFiSh solutions (See text description in Sect. 7.1.4), three other 1-D numerical schemes and the 3-D model from [57] The model parameters are shown in Table 4 and the error calculations in Table 13, 30 and 31 .

	Junction					
	DCG	LCG	STM	McCMatrix1N	McCFlux1N	McCMatrix1L
$\mathcal{E}_P^{RMS}$	0.42	0.43	0.42	0.41	0.42	0.41
$\mathcal{E}_Q^{RMS}$	1.19	1.13	0.46	1.11	1.12	1.10
$\mathcal{E}_{\Delta r}^{RMS}$	4.07	4.02	4.05	4.07	4.08	4.08
$\mathcal{E}_P^{MAX}$	0.75	0.75	0.73	0.73	0.74	0.74
$\mathcal{E}_Q^{MAX}$	3.58	3.54	1.48	3.43	3.53	3.41
$\mathcal{E}_{\Delta r}^{MAX}$	6.86	6.76	6.98	6.84	6.85	6.85
$\mathcal{E}_P^{SYS}$	-0.69	-0.70	-0.69	-0.70	-0.70	-0.71
$\mathcal{E}_Q^{SYS}$	-3.52	-3.53	-1.08	-3.43	-3.52	-3.40
$\mathcal{E}_{\Delta r}^{SYS}$	-6.81	-6.73	-6.90	-6.83	-6.83	-6.84
$\mathcal{E}_P^{DIAS}$	0.53	0.55	0.53	0.53	0.54	0.52
$\mathcal{E}_Q^{DIAS}$	1.76	1.78	0.69	1.77	1.77	1.77
$\mathcal{E}_{\Delta r}^{DIAS}$	-1.95	-1.92	-1.88	-1.94	-1.94	-1.95

Table 13: Calculated relative root mean square, maximum, systolic and diastolic errors (%), as defined in Eq. (56), for test cases corresponding to Fig. 16 or the aortic bifurcation (AoBif). Errors are determined at the midpoint of each segment.

7.1.5 Benchmark (in vitro)

In this section different features of STARFiSh are tested and compared with each other in the Benchmark (in vitro test). For this test the results have been moved to Appendix C. Fig. 30 to 33 show the results in selected aortic segements and through first second and third generation vessels. Table 32 show errormetrics comparing with in vitro data. Some of the other state of the art flow-solvers are also present for better visualization. MacCMatrixaL is STARFiSh with Matrix based scheme with linear bifurcation model, and convective correction factor calculated according to Eq. 4 (combination 6), MacCMatrix1N is STARFiSh with Matrix based scheme with nonlinear bifurcation model, and convective correction factor set to one (combination 5), McCFlux1N is STARFiSh with Flux based scheme with nonlinear bifurcation model, and convective correction factor set to one (combination 3). There are no significant difference between any of the solutions, either in waveforms (figures) or errormetrics.

7.1.6 Benchmark (ADAN55 model)

In this section different features of STARFiSh are tested and compared with each other in the detailed arterial network adan55. Fig. 17 and Fig. 18 show the pressure and flow waveforms in the aorta and in third and fourth generation of bifurcations. Fig. 19 show pressure in the 15 segments that form the aorta, in different period of the cycle. The methods and grid description of the different STARFiSh solutions, McCFlux1, McCFlux2, McCMatrixN and McCMatrixL are listed in Table 14. DCG and LCG solutions are plotted for Comparison. As can be seen from the Figures, the differences between the STARFiSh solutions are quite big, and this test revealed some problems and limitations of the original implementations in STARFiSh. The test has a high density of link and bifurcations, and also have high Reynolds-number in the aortic segments. One can see that the tests run with the original implementations of STARFiSh (Combination 5 and 6) deviate a lot from the other state of the art Flow-Solvers. From Fig. 19 it is clear that the behaviour in the Bifurcations are quite important in this test, and that the bifurcation model which ensures continuity of static pressure introduce quite big errors in this test. It also proved that the difference between the flux based scheme and the matrix based scheme is quite big in this test. The Flux based method is much more in accordance with the other solvers. As previously described in the Grid adaption Sect. 6.6, The number

simulation	combination	α	Δt [ms]	CFL number
McCFlux1	3	1	0.1	0.6-0.9
McCFlux2	3	1	0.25	0.5
McCMatrixN	5	1	0.25	0.5
McCMatrixL	6	1	0.25	0.5

Table 14: Simulation cases corresponding to Fig. 17 to 19.

of nodes, and CFL number is also of big importance here. McCFlux2 and McCFlux1 are both combination 1 solutions, but McCFlux 1 has a finer grid. The solution seem to converge to the other state of the are flow-solver, as the grid gets finer.

(a) Aortic Arch

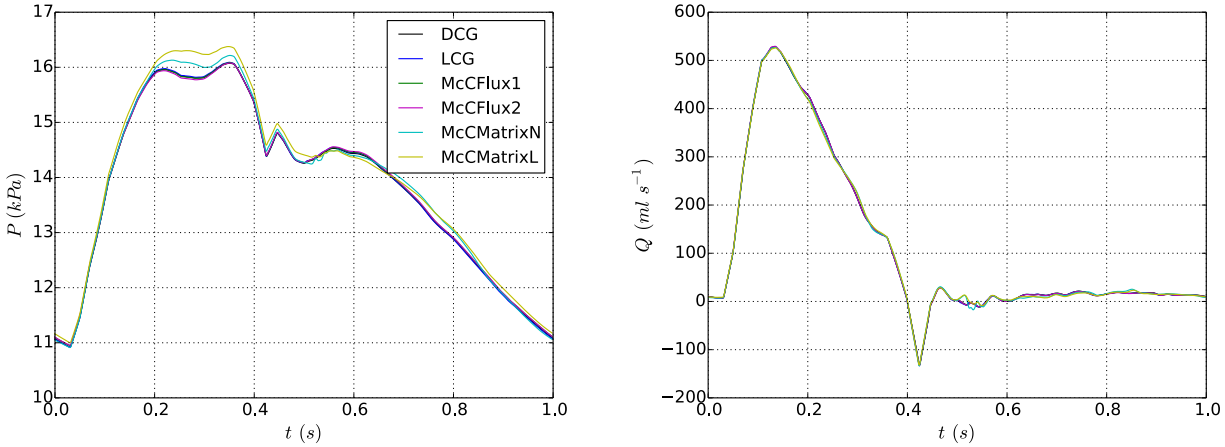

(b) Thoracic Aorta

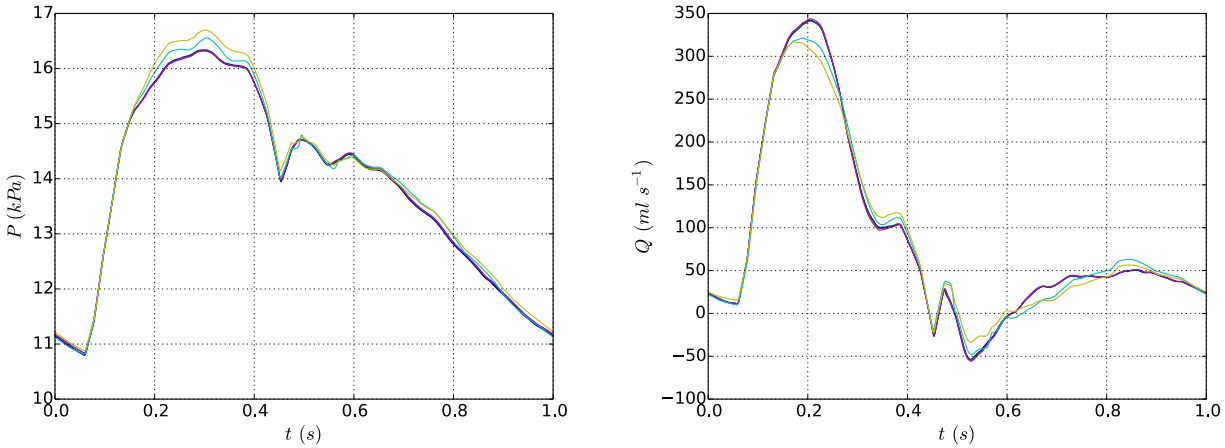

(c) Abdominal Aorta

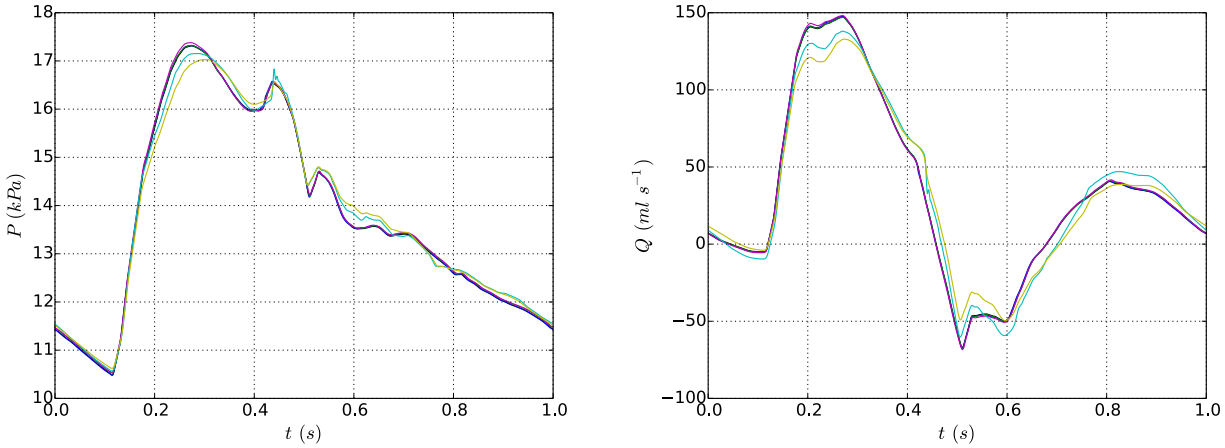

Figure 17: ADAN55 model. Pressure (left) and flow (right) waveforms in the midpoint of three aortic segments: (a) aortic arch I, (b) thoracic aorta III and (c) abdominal aorta V. Results are shown for STARFiSh solutions, McCFlux1, McCFlux2, McCMatrixN and McCMatrixL. Difference in grid and methods used are listed in Table 14. General model parameters are shown in Table 6.

(a) Right Posterior Interosseous

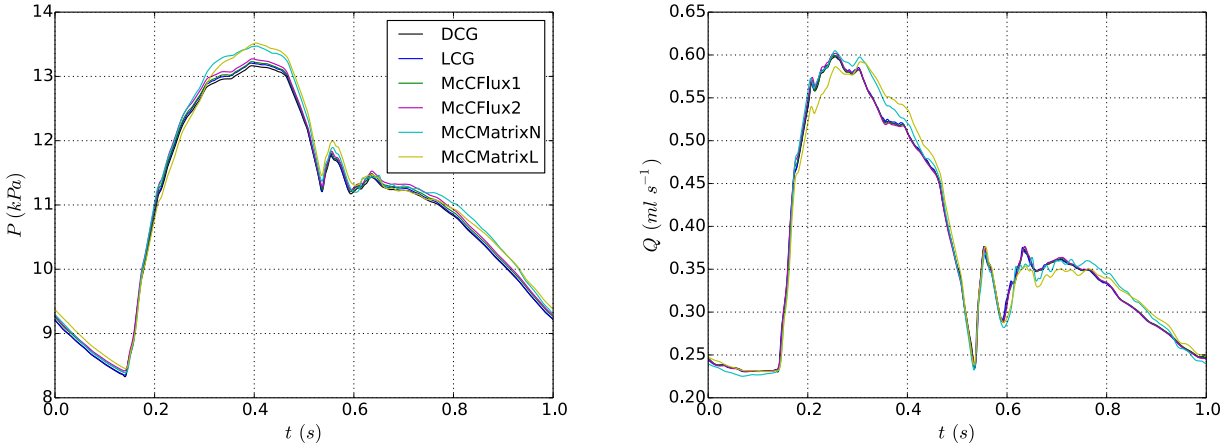

(b) Right Femoral

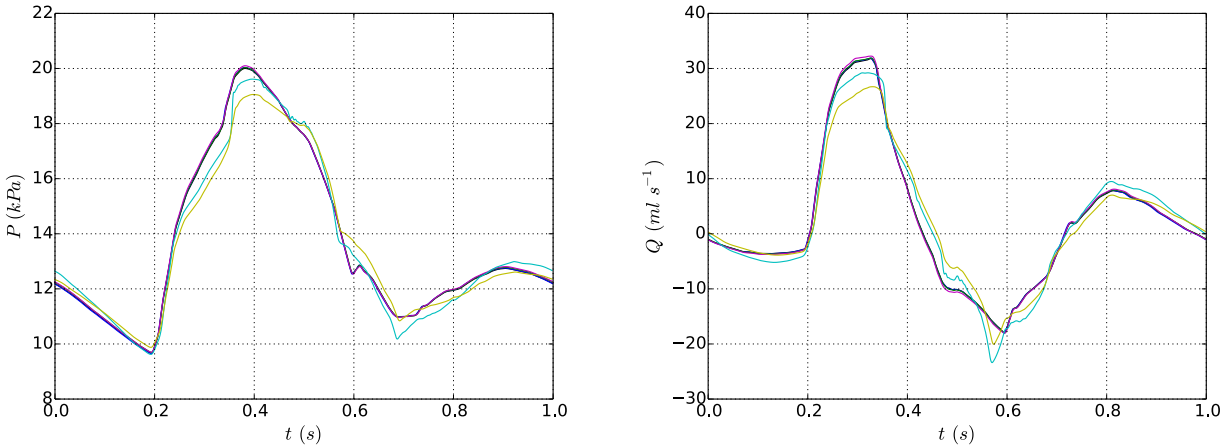

(c) Right Anterior Tibial

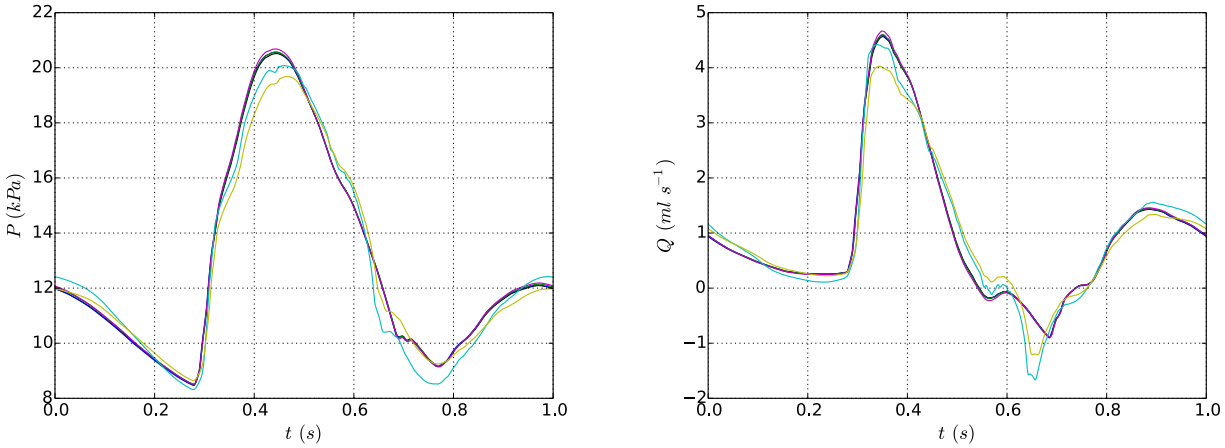

Figure 18: ADAN55 model. Pressure (left) and flow (right) waveforms in the midpoint of three vessels from the third and fourth generation of bifurcations: (a) right posterior interosseous, (b) right femoral and (c) right anterior tibial. Results are shown for STARFiSh solutions, McCFlux1, McCFlux2, McCMatrixN and McCMatrixL. Difference in grid and methods used are listed in Table 14. General model parameters are shown in Table 6.

(a) $t/T = 0.1$ (b) $t/T = 0.2$

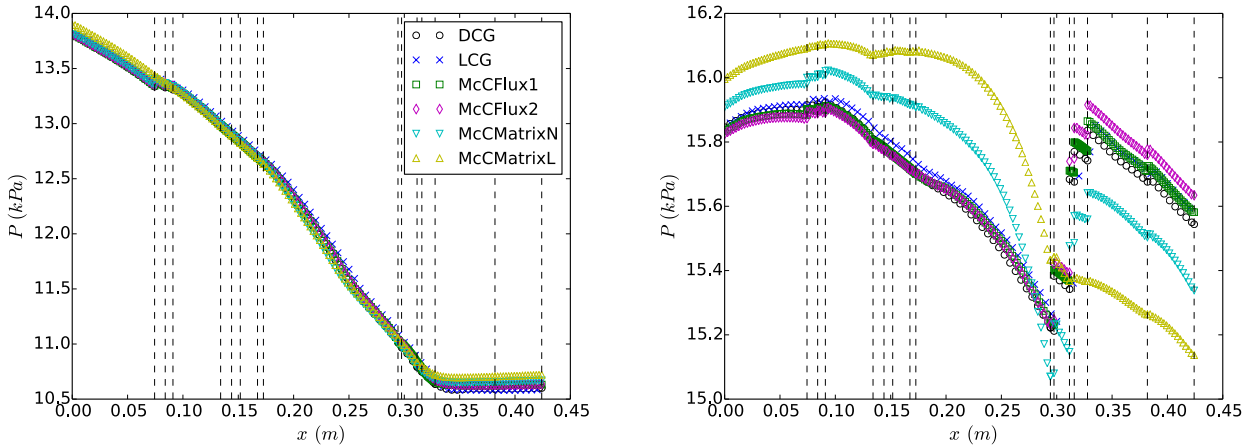

(c) $t/T = 0.3$ (d) $t/T = 0.5$

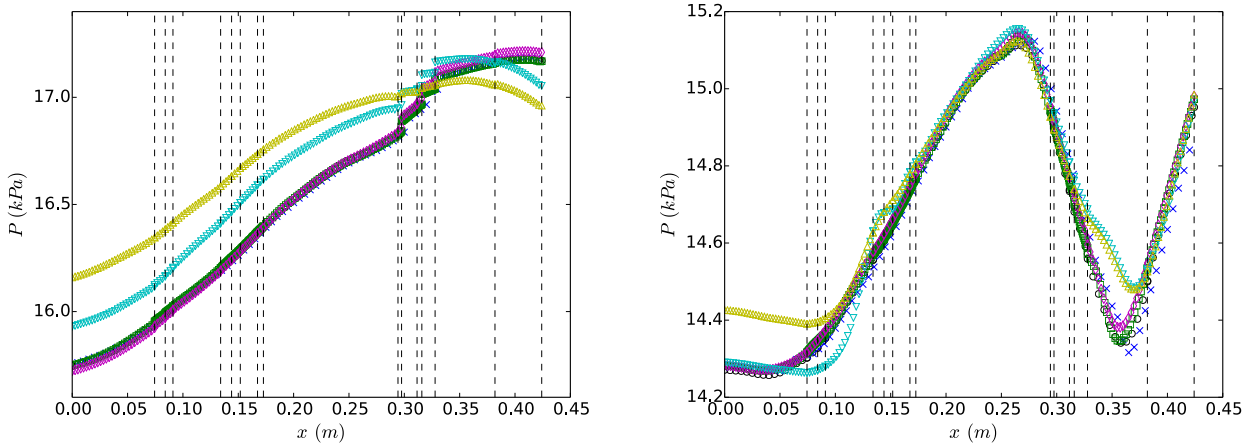

(e) $t/T = 0.7$ (f) $t/T = 1.0$

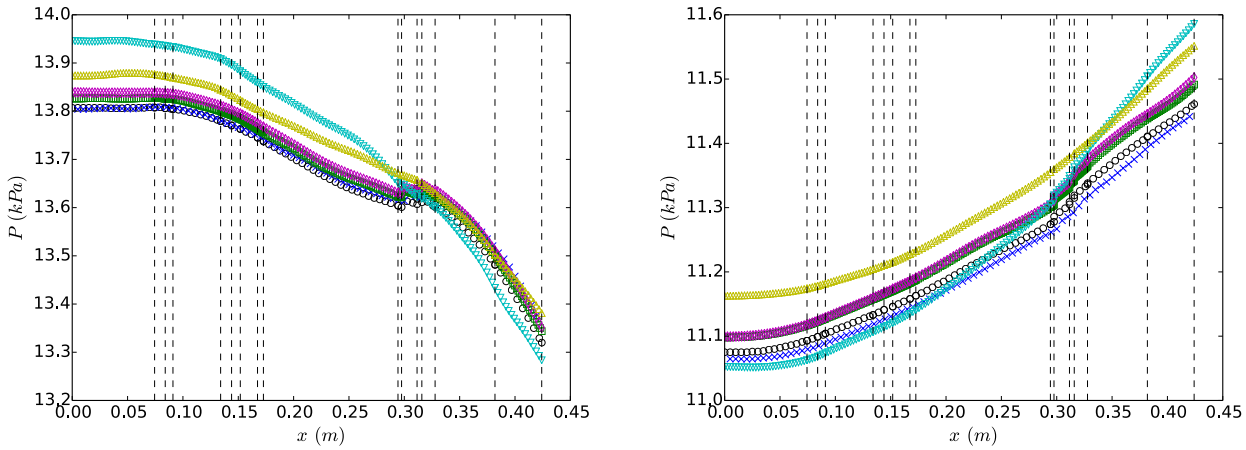

Figure 19: ADAN55 model. Pressure contour along the aorta at several time instants during the cardiac cycle, relative to the cardiac period T.

7.1.7 Steady Flow in a single vessel with narrowing in the middle

In this section the results from the test with narrowing (continous and link) is presented. In this case the flow is assumed laminar even though the case is without friction (Reynolds number is undefined ($Re = \frac{\rho U d}{\mu}$)). Thus for this case the analytic solution through the narrowing is the Bernoulli equation:

$$\Delta P = \frac{\rho}{2}\left(U_2^2 - U_1^2\right) \tag{63}$$

where U_1 is the mean velocity before the narrowing, and U_2 is the mean velocity in the narrowing. Conservation of mass yields $U_1 A_1 = U_2 A_2$, inserting in Eq. 63 give

$$\Delta P = \frac{\rho U_1^2}{2}\left(\frac{A_1}{A_2} - 1\right) \tag{64}$$

The equilibrium static pressure is given by $P = QR = 10^{-4}$ m^3/s 10^8 Pa s/m^3 = 10000 Pa. The flux based formulation given by Eq. 39 and Eq. 40 is not possible to part from the analytic Bernoulli solution. The Matrix formulation on the other hand given by Eq. 35 deviate from the Bernoulli solution as can be seen by two peaks in total pressure during the narrowing. It is also clear that the matrix based scheme does not regain the same pressure after the narrowing, as it should. The test reveal the non-conservative aspects of this method. The test also show that the new link model, which is the same as the bifurcation model presented in Sect. 3.7.2, but with only two vessels, is in accordance with the analytic Bernoulli solution. Using the model based on continuity of static pressure introduce quite big errors in this case. This is all clear from Fig. 20. All tests were run with $\Delta t = 0.6$ ms and with a total of 2001 nodes (equidistant spacing). The simulations were initialized with zero pressure and zero flow rate. The flow rate was then set to increase linearly from $Q(t = 0) = 0$, to $Q(t = 1s) = 100$ ml/s. The flow rate was then set constant for another 120 seconds to allow for steady state solution. The long time needed for steady state is a result of reflections from distal and proximal boundaries (prescribed total flow is highly reflective).

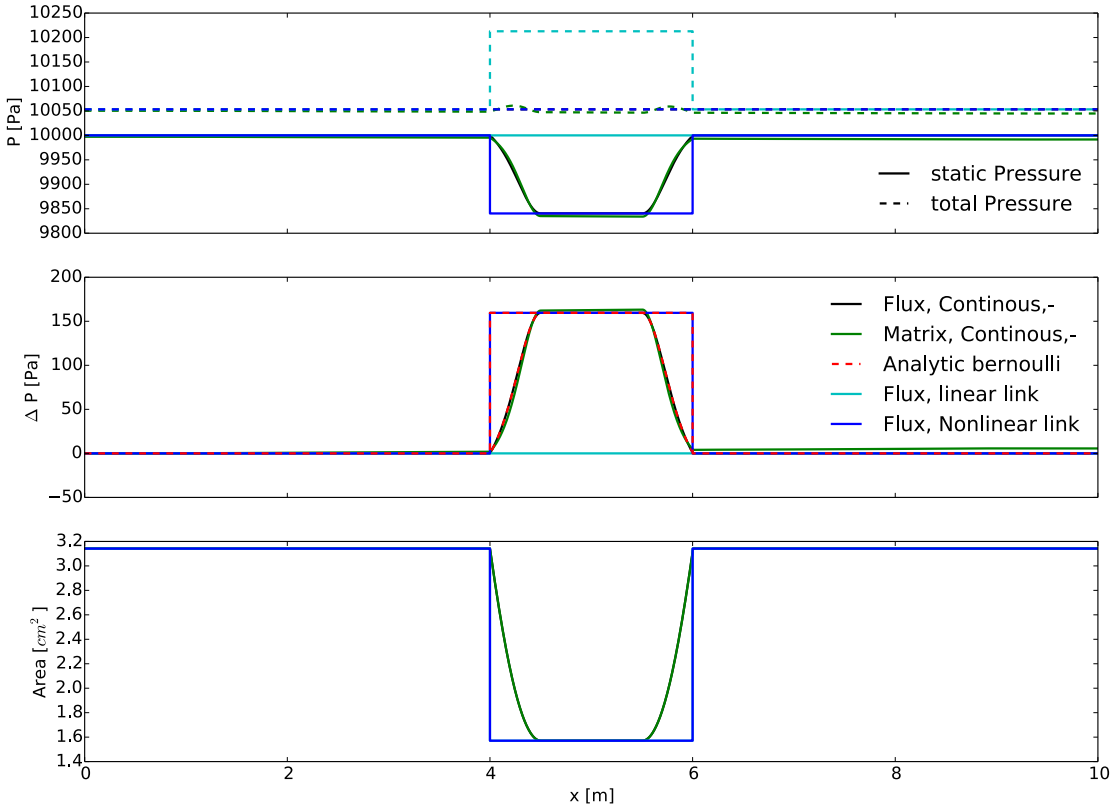

Figure 20: Results showing comparison between Flux based formulation of the MacCormack scheme given by Eq. 39 and Eq. 40, and the previously implemented Matrix formulation given by Eq. 35 (Continuous sine vessel). It also show the comparison of the implemented link model based on continuity of total pressure, and the previously implemented model based on continuity of static pressure. One can see that the Matrix formulation is not in accordance with the analytic Bernoulli solution. It also does not have completely regained the pressure after the narrowing. The difference between the two link models are big, and using the static pressure model introduce big errors comparing with the analytic Bernoulli solution.

7.1.8 Constant Flow in symmetric and asymmetric single-bifurcation

In this section the nonlinear bifurcation model described in Sect. 3.7.2 is tested and compared with analytic Bernoulli solutions. Since the test has constant flow and does not include friction, the network has an electrical equivalent analytical solution (See Fig 23). As described in Sect. 4.8 both a symmetric and an asymmetric bifurcation is evaluated. The first of which having a relatively easily derived analytic counterpart. Symmetric geometry and Resistance divide the flow into $Q_l = Q_r = \frac{Q_m}{2}$. In addition pressure and flow need to be in equilibrium with the resistance in the distal end of the daughter vessels $P_l = P_r = Q_l R = Q_r R = \frac{Q_m}{2} R = 50 * 1e^{-6} * 1e^{8} Pa = 5000 Pa$. Thus the pressure difference from daughters and mother can be

evaluated:

$$\Delta P_{m-l} = \Delta P_{m-r} = \frac{\rho}{2}\left(U_l^2 - U_m^2\right) = \frac{\rho}{2}\left(\left(\frac{Q_l}{A_l}\right)^2 - \left(\frac{Q_m}{A_m}\right)^2\right) = \frac{\rho}{2}\left(\left(\frac{Q_m/2}{A_m/4}\right)^2 - \left(\frac{Q_m}{A_m}\right)^2\right) = \frac{3\rho U_m^2}{2} \tag{65}$$

Where all RHS elements are known. Subscript m, l, and r denotes mother-, left daughter- and right daughter-vessel.
With the asymmetric bifurcation on the other hand, the pressure and flow values in mother, right and left daughter vessel is not as easily depicted. However, there are five equations and five unknowns; one mass equation, two Bernoulli equations, and two $P - Q$ equilibrium equations, for the five unknowns $(P_m, P_l, Q_l, P_r, Q_r)$

$$\begin{aligned} Q_m &= Q_r + Q_l \\ \Delta P_{m-l} &= \frac{\rho}{2}\left(U_l^2 - U_m^2\right) \\ \Delta P_{m-r} &= \frac{\rho}{2}\left(U_r^2 - U_m^2\right) \\ P_l &= Q_l R \\ P_r &= Q_r R \end{aligned}$$

Being non-linear the above system must be solved iteratively. A Newton-Rhapson solver similar to the one described in Sect. 3.7.2 have been used to solve for the analytical electrical equivalent system, to compare with STARFiSh solution. See Appendix E.1 for a complete description of the Newton Rhapson solver.
The results for the symmetric bifurcation are presented in Fig. 21 and Table 15, and the results for the asymmetric bifurcation in Fig. 22 and Table 16. Both cases have very good agreement between STARFiSh and analytical solution. Tests were also run with asymmetric distal boundary ($R1 \neq R2$) with similar agreements with analytical solution.

Variable	Mother	Daughters
$P_{STARFiSh}$,	5159.58086424 Pa	5000.0 Pa
$P_{analytic}$,	5159.5808642 Pa	5000.0 Pa
$Q_{STARFiSh}$,	100 ml/s	50.0 ml/s
$Q_{analytic}$,	100 ml/s	50.0 ml/s

Table 15: Results comparing STARFiSh with analytical Bernoulli solution in the symmetric bifurcation. The focus is on the numerical solution, and digits have not been rounded.

All simulations in this sections were run with $\Delta t = 0.6ms$, and $\Delta x = 0.5$ cm. The simulations were initialized with zero pressure and zero flow rate. The flow rate was then set to increase linearly from $Q(t = 0) = 0$, to $Q(t = 1s) = 100$ ml/s. The flow rate was then set constant for another 120 seconds to allow for steady state solution.

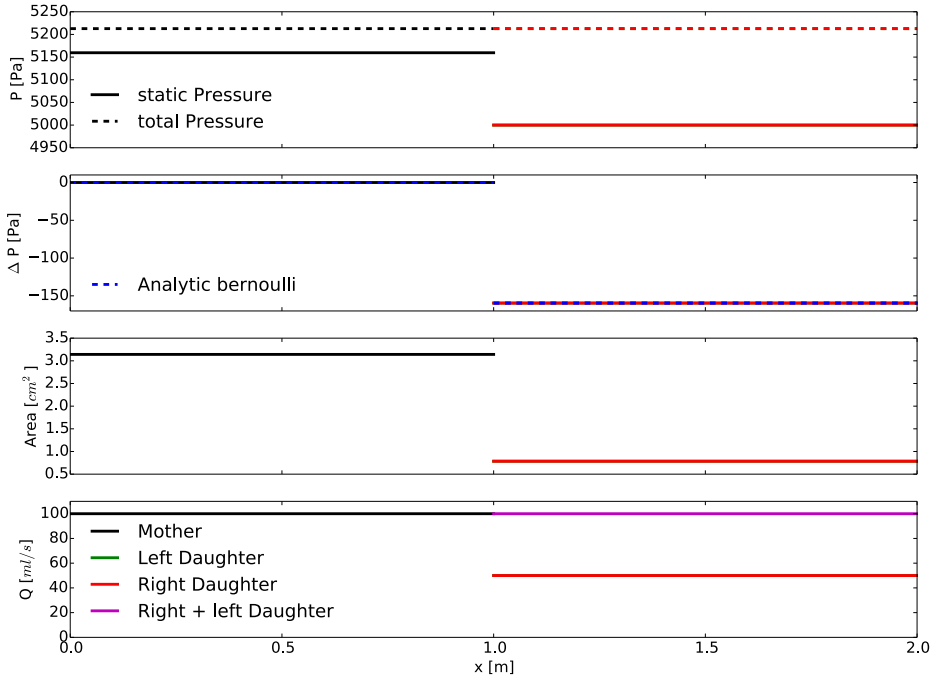

Figure 21: Showing static and total (dottedline) [top], dynamic pressure together with analytic Bernoulli solution, area and flow rate [bottom], for the symmetric bifurcation

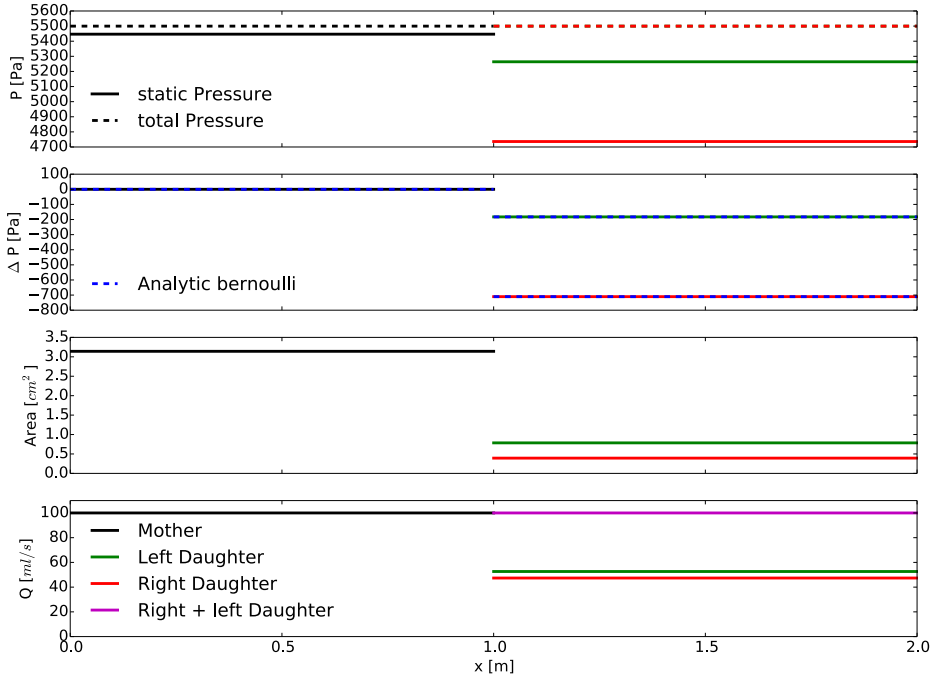

Figure 22: Showing static and total pressure [top], dynamic pressure together and analytic Bernoulli Pressure, area and flow rate [bottom], for the asymmetric bifurcation

Variable	Mother	L. daughter	R. daughter
$P_{STARFiSh}$,	5446.53374527 Pa	5263.89970128 Pa	4736.10029885 Pa
$P_{analytic}$,	5446.53374527 Pa	5263.89970117 Pa	4736.10029883 Pa
$Q_{STARFiSh}$,	100 ml/s	52.6389970137 ml/s	47.3610029884 ml/s
$Q_{analytic}$,	100 ml/s	52.6389970117 ml/s	47.3610029883 ml/s

Table 16: Results comparing STARFiSh with analytical Bernoulli solution in the asymmetric bifurcation. The focus is on the numerical solution, and digits have not been rounded.

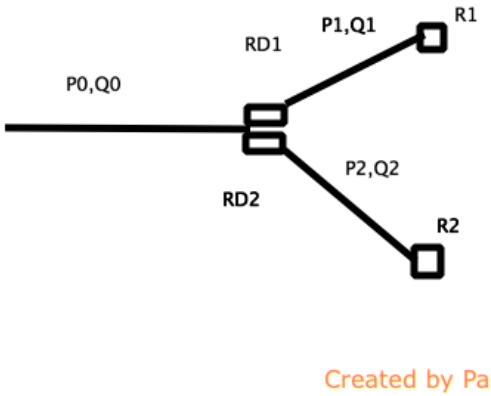

Figure 23: Showing the electrical equivalent system to the bifurcation with constant flow and distal single resistance boundary. R1, and R2 are the distal boundary resistance, whereas RD1 and RD2 are the resistances that govern the dynamic pressure difference between each daughter and the mother vessel.

7.2 Womersley

In this section some test are performed on the Womersley model. In Fig. 25 the input flow signal used in ThoaA test have been transformed from time-domain to frequency-domain to calculate the velocity profiles (using r_d as constant radius). Fig. 25 show the input flow, and the flow from the integrated velocity profiles. The input and output is indiscernible. Fig. 26 show the comparison of the nonlinear convective term $\left(\int_A u^2 \mathrm{d}A\right)$ using womersleytheory, assuming a flat velocity profile, and using the assumed power law profile given by Eq. (3). Fig. 27 show the difference between the friction-term $f(x,t) = 2\mu\pi r \frac{\partial u}{\partial \xi}|_{\xi=r}$ using womerslyetherory, and the assumed velocity profile. Finally Fig. 24 show the application of the womersleytheory in the ThoaA test. McCFlux is combination 1 solved in STARFiSh, McCFluxmy is combination 1 solved on personal computer using my own created minisolver, Womersley is solution using womersleytheory in both convective and friction-term, and Womersleyf is solution using womersleytheory in friction-term only. 3D data and DCG solution is showed for comparison. Error-metrics are given in Table 12. There are a few things to note; the difference between using Womersleytheory only in friction term, and using it in both the convective and friction term is not very big. Using womersleytheory on the friction-term seem to give rise to bigger difference (comparing with powerlaw), than using it on convective term. This is also evident in the pressure Gradient shown in Fig. 24. The solutions with Womersleytheory follow the same path, but a noticeable different one than the power-law solutions. Also noticable is that peak

pressure is lower in solutions with Womersley, and also further apart from the peak pressure in 3D solutions, than the power-law solutions. Errormetrics are worse for solutions with womersleytheory. McCFlux and McCFluxmy are indiscernible. The solutions were run with $\Delta t = 1$ ms and using 17 nodes, giving a maximum CFL number of about 34. The high Δt was chosen because of long simulation time for the Womersley simulations.

Looking at Fig. 28 one can see that using the assumed powerlaw velocity-profile in ThoA test give very similar profiles to those obtained with Womersley solution. This is especially the case in the systolic parts of the cycle.

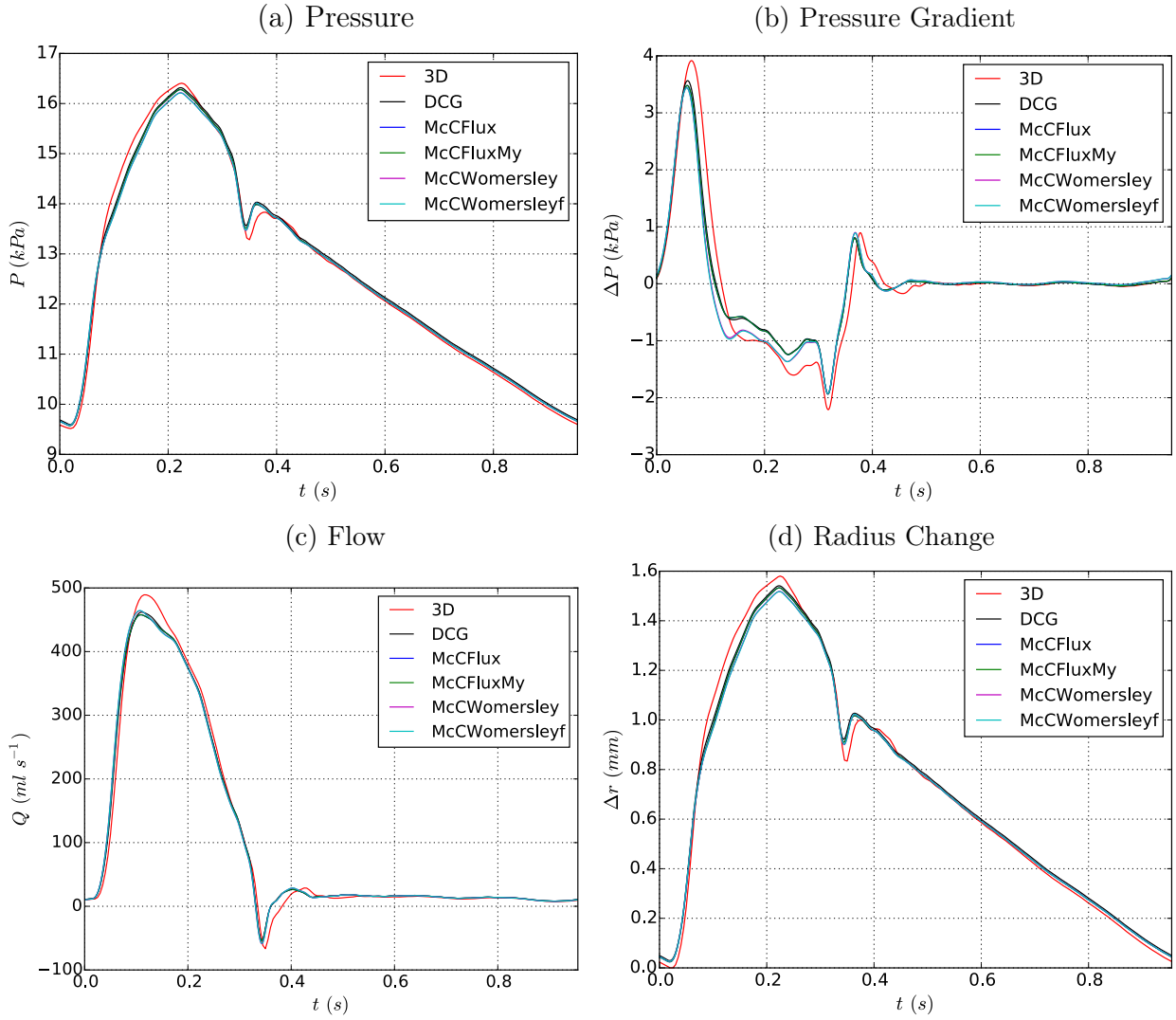

Figure 24: Upper thoracic aorta. Pressure (a), pressure gradient between inlet and outlet (b), flow rate (c), and change in radius from diastole (d) with time at the midpoint of the vessel. Results are shown for four different McC solutions (See text description in Sect. 7.2), one other 1-D numerical scheme and the 3-D model from [57]. The model parameters are shown in Table 3 and the error calculations in Table 17.

	ThoAW				
	DCG	McCFlux	McCFluxMy	Womersley	Womersleyf
$\mathcal{E}_P^{RMS}$	1.08	1.04	1.04	1.18	1.19
$\mathcal{E}_Q^{RMS}$	2.55	2.51	2.51	2.75	2.80
$\mathcal{E}_{\Delta r}^{RMS}$	2.30	2.43	2.43	2.79	2.82
$\mathcal{E}_{\Delta P}^{RMS}$	7.71	7.74	7.74	8.82	9.04
$\mathcal{E}_P^{MAX}$	3.55	3.10	3.10	3.38	3.46
$\mathcal{E}_Q^{MAX}$	9.12	8.78	8.78	10.65	11.03
$\mathcal{E}_{\Delta r}^{MAX}$	7.77	6.96	6.96	7.81	7.97
$\mathcal{E}_{\Delta P}^{MAX}$	31.86	32.76	32.76	38.86	40.34
$\mathcal{E}_P^{SYS}$	-0.55	-0.78	-0.78	-1.17	-1.19
$\mathcal{E}_Q^{SYS}$	-5.57	-6.41	-6.41	-5.14	-5.03
$\mathcal{E}_{\Delta r}^{SYS}$	-2.48	-3.01	-3.01	-3.92	-3.98
$\mathcal{E}_{\Delta P}^{SYS}$	-8.97	-11.15	-11.15	-12.16	-12.18
$\mathcal{E}_P^{DIAS}$	0.85	0.61	0.61	0.71	0.71
$\mathcal{E}_Q^{DIAS}$	2.70	2.58	2.58	1.60	1.74
$\mathcal{E}_{\Delta r}^{DIAS}$	1.86	1.53	1.53	1.67	1.67
$\mathcal{E}_{\Delta P}^{DIAS}$	7.28	6.99	6.99	7.27	7.31

Table 17: Calculated relative root mean square, maximum, systolic and diastolic errors (%), as defined in Eq. (56), for test cases corresponding Fig. 24, or the upper thoracic aorta (ThoAo). Errors are determined at the midpoint of the segment.

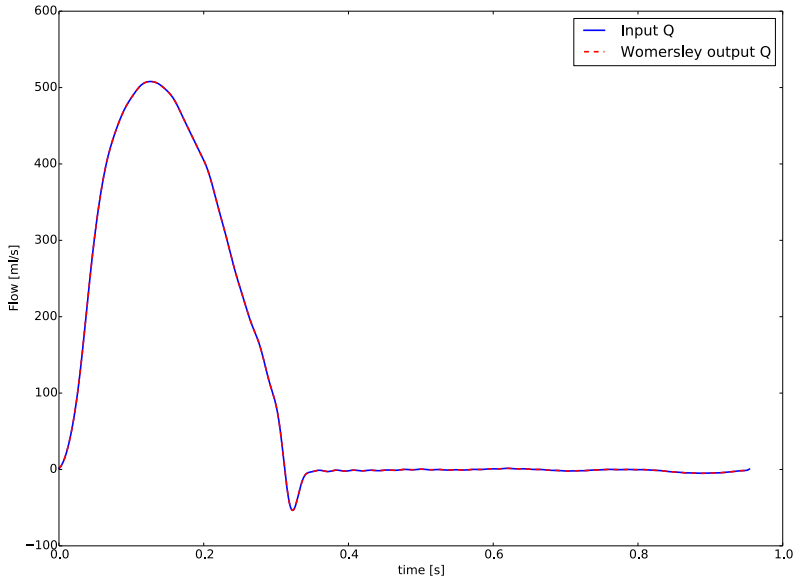

Figure 25: Results showing transformation of input-signal Q, to the frequency-domain to obtain the the velocity profiles during one period. The velocity profiles are then integrated to regain the flow. The input and output is indescernible

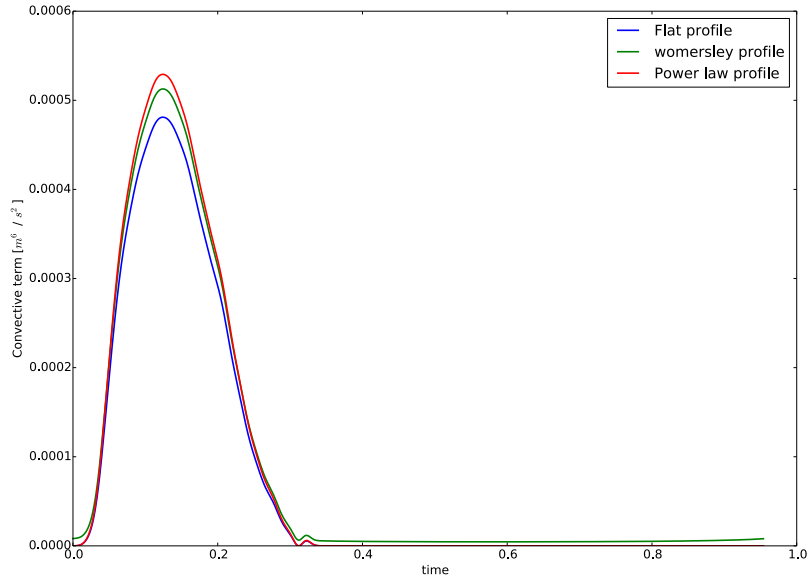

Figure 26: Comparing the convective term $\left(\int_A u^2 \mathrm{d}A\right)$ using flat velocity profile, Womersley profiles and the assumed power law ($\zeta = 9$) velocity profile.

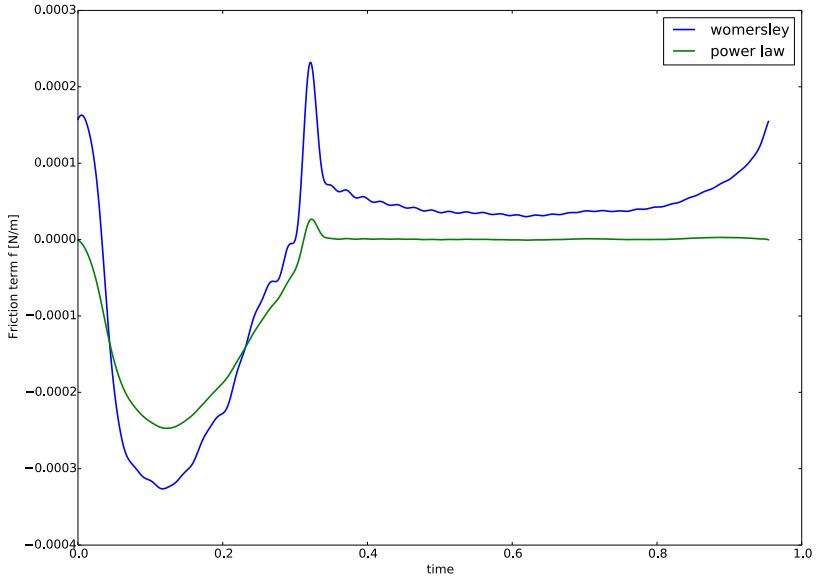

Figure 27: Comparing the friction term ($f(x,t) = 2\mu\pi r \frac{\partial u}{\partial \xi}|_{\xi=r}$) using Womersley theory, and the assumed velocity profile.

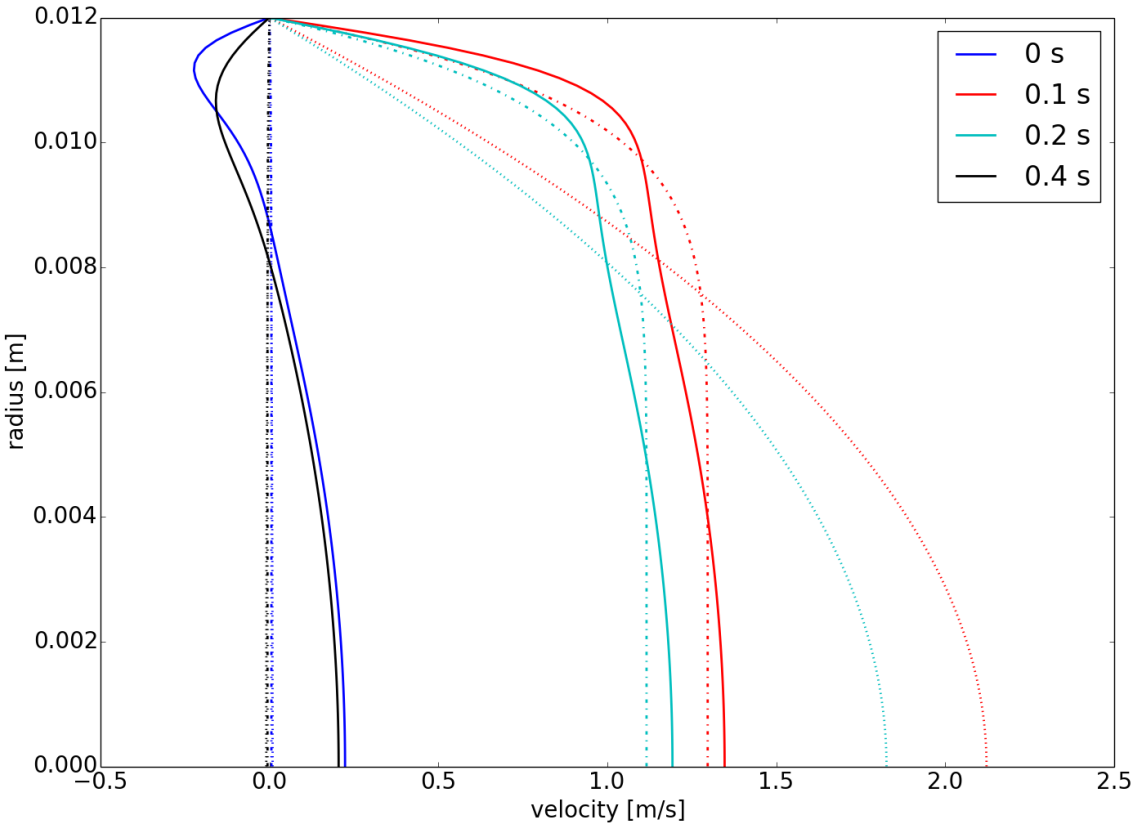

Figure 28: Comparing the velocity profiles obtained from inlet of ThoA, using Womersly theory(-), using assumed power law ($\zeta = 9$) profiles (-.), and assuming Pouseille flow (:).

8 Discussion

In this section the results from Sect. 7 are discussed. In Sect. 8.1 the implementations and different methods used in STARFiSh are discussed. The findings here form the basis for the final solutions/methods used in STARFiShs contributions in Comparison1Dscheme. These solutions are then compared with the five other state of the art numerical flow-solversin Sect. 9, and discussed in Sect. 10. Finally the tests run with Womersley theory is discussed in Sect. 8.2.

8.1 STARFiSh

8.1.1 SingleVesselPulse

After fixing the implementation error in the original scheme, there is not a lot of difference between the Flux based method and the Matrix based scheme, however looking at Fig. 13 it seems as though the Flux based scheme is more in accordance with the other state of the art solvers. This case has negligible convective terms dependence, due to the low flow rate (1 ml/s). Both schemes are non diffusive, but comparing with FEM, the Matrix formulation seem to be more dissipative.

8.1.2 CCA, AoBif, BenchMark

All these three tests has low flow rate Q. As a result the nonlinear convective acceleration term in the balance of momentum has a less significant weight relative to the other terms. This is reflected in very small differences when comparing the Flux based scheme and the Matrix based scheme. The non-conservative aspects of the Matrix formulation is not prominent. Thus these test didn't reveal any limitations of the original scheme. Regarding the bifurcation model the nonlinear model does not seem to be a drawback in test 4.4 and 4.5. This is related to the low flow, and small difference in total area from mother vessel to daughter vessel(s). Looking at test 4.4 which has a peak flow of about 70 ml/s and and relative difference in area (diastolic) between mother and daughter vessel equal to $\frac{\pi r_m^2}{\pi r_d^2} = \frac{0.85^2}{0.6^2} \approx 2$. The difference in pressure is:

$$\Delta P = \frac{\rho U_1^2}{2} - \frac{\rho U_2^2}{2} \approx -0.3Pa \tag{66}$$

The difference is thus negligible. Test 4.5 has even lower flow, (low velocities) and correspondingly small differences in dynamic pressure. Also looking at the error-metrics comparing with 3D data in Table 11 for the CCA test, and Tables 13 to 31 for AoBif it is not obvious that the Matrix formulation and linear bifurcation/link model is less correct. It is sort of a paradox that in some of the error-metrics they even seem to be more correct. However this should not be used as proof of their correctness. The 1D models assume fully developed axisymmetric flow, and does not account for boundary layers. Also Vortex flow and recovery length in Bifurcations etc. are not accounted for. All of this likely introduce a lot more errors than the errors due to internal fluxes in the Matrix scheme, and the linearity in the static bifurcation/link model. The difference between using convective correction-factor set to one, or calculated according to Eq. 4 is very small. This may also be explained by the physical problem, and the low relative weight on the convective term.

8.1.3 ThoA

This test is a more demanding test than the CCA test, since it has higher flow and a bigger Reynolds-number. As a result the nonlinear convective acceleration term in the balance of momentum has a more significant weight relative to the other terms. Comparing the Flux based scheme, with the Matix based scheme in Fig. 15 the difference between the Flux and Matrix scheme is more obvious. The Matrix based scheme follow a different curve than the Flux based scheme, and also the other state of the art solvers. The difference is especially prominent in the pressure gradient and the flow waveforms. This is due to internal fluxes introduced by the Matrix scheme. Once again, this is not necessarily represented in the error-metrics in Table 12. The other schemes form a better comparison than the 3-D data. The difference between using convective correction-factor set to one, or calculated according to Eq. 4 is very small. The difference is only a scaling of $\alpha = 1$ and $\alpha = 1.1$ respectively. Thus neglecting the nonlinear effect in this test is justified. This is in accordance with Stergiopulos *et al.* [46].

8.1.4 Adan55

This test proved to be a very good test for figuring out the present state of STARFiSh. The test was constructed to be a demanding test for the methods, which it indeed has proven to be. The test has many bifurcations and links, with big difference in mother and daughter vessel areas, resulting in relative big importance of dynamic pressure changes. Thus the original linear bifurcation model introduced big errors. Fig. 19 show the different behaviour of the bifurcation models in an excellent way. The test also have aortic segments with big Reynoldsnumber. As a result the nonlinear convective acceleration term in the balance of momentum has a more significant weight relative to the other terms. It is very clear from Fig. 17 to Fig. 18 that internal fluxes introduced by the nonconservative Matrix scheme also introduce big errors in this test. The internal flux errors seem to accumulate in the big network and effect the pressure and flow waveforms distinctly. The Parameters for the Tube law should be set with tapering also included in the wall-thickness, like discussed in described in the Gridadaption Sect. 6.6. Thus from the first test, to the final one, submitted in Comparison1Dscheme, three important changes were made:

bifurcations	New nonlinear model implemented.
Scheme	New scheme implemented.
Tube law	Wall-thickness including tapering.

Still there are some unresolved problems regarding the grid-dependence in this test. This is believed to be related to the many bifurcations, and introduction of very short vessels in aortic regions with big flow, and resulting big changes in dynamic pressure. The region is thus highly nonlinear and challenging for the methods. This was discussed in Sect. 6.6 and some thought and possible reasons for the grid-dependance is revisited here:

characteristic variables

The Riemann variables moving toward the bifurcation/link is calculated by interpolation. With few nodes, and in the limit of only having one node at each boundary, no field equations are solved. Thus the solution is only calculated from the bifurcationmodel. The Riemann invariants needed from the vessel with only two boundary nodes is thus interpolated between these two boundary-nodes. The Riemann invariants are based on a linearized inviscid form of the governing equations (18). There might be a big difference in order of accuracy between the linearized Riemann solutions, and the actual scheme solving the 1-D equations. When fewer nodes are used, more weight is put on the linearizion.

Another related question arises when calculating the Riemann invariant coming from the field. For instance for the mother vessel $\omega_1^1(x_1, t^{n+1}) = \omega_1^1(x_1 - \Delta x_1, t^n)$ is considered known. In the current implementation of STARFiSh ω_1^1 is calculated based on information on the distal node of the vessel. However I argue that if CFL numbers are close to one, information should be taken from node -2 rather than -1 to calculate it. The effect of this is likely not very big, since the only information that is needed is λ_1, λ_2, c, and C. See Sect. 2.2.

PQ vs AU characteristics

In Sect. 2.2 a characteristic analysis is performed on both the AU and the PQ systems under assumption of negligible local viscous losses (*i.e.* zero right hand side). However looking at the RHS of these two system, they are not equal. If this constitute a difference, and the magnitude of this difference however is uncertain, but could be tested.

constrained area

This is an area which is highly constrained, and both the field-waveform and Bernoulli equation should be satisfied. This constitute a numerical difficulty.

Initialization

The simulation is initialized with Constant pressure and zero flow. Thus the network is not initilized in equilibrium $P = QR$, where R is the Resistance in the network. The field equations should converge to the equilibrium, however it is not certain that this is the case for the boundaries. The boundaries are calculated with Δ values. Thus if one start outside equilibrium, the solution does not necessarily converge to equilibrium. See also Sect. 8.3.

P, Q system	As described in Sect. 3.5 I argue that the P, Q system have some non-conservative aspects comparing with the A,U system. Thus it would be interesting to solve this test with an implementation of the A,U system, to see if the grid-dependence is in part due to non-conservative P,Q formulation.
Alternating scheme	It has been argued [20] that MacCormack (forward/backward) is better at resolving waves propagating in the positive direction, and opposite for MacCormack (backward/forward). The errors are more prominent in systole when the flow is big. Consequently the difference between velocity of forward and backward traveling waves could be relatively big. A scheme that alternates between forward/backward and backward/forward could maybe resolve the problem better. This would probable also be an advantage when solving vessels with few nodes. In the limit of only having three nodes, only using forward/backward method for instance result in more weight on node 1 and 2, than 3. Alternating thus lead to a solution based more evenly on the domain. See Fig 29

(a) Forward/Backward (b) Backward/Forward

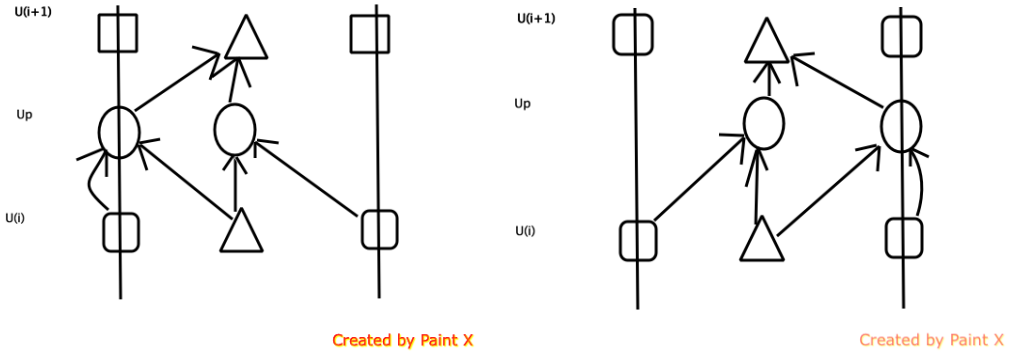

Figure 29: Illustration of the difference between using Forward/Backward (left) and Backward/Forward macCormack scheme. The arrows indicate where information (Fluxes and RHS) are taken from to calculate the field node in a vessel with only three nodes.

8.1.5 Steady Flow in a single vessel with narrowing in the middle

This test was created as a test of the new link model, and a check of the two schemes (Flux and Matrix) ability to regain pressure after the narrowing. It is clear that the new link model follow the Analytic Bernoulli solution. Also the Flux based scheme follow the Analytic Bernoulli solution through the narrowing, and regain the pressure after the narrowing. The Matrix based scheme on the other hand, does not follow the analytic Bernoulli solution through the narrowing. In addition, the pressure is not fully regained after the narrowing. Once again this is related

to the changes in the convective term through the narrowing, and internal fluxes from the non-conservative matrix form introduce noticeable errors.

8.1.6 Constant Flow in symmetric and asymmetric single-bifurcation

The results from the symmetric and asymmetric bifurcations show excellent agreement with analytical Bernoulli and electrical-equivalent solutions. The tests thus show that STARFiSh with the newly implemented nonlinear bifurcation model is able to reach correct steady state solutions for single bifurcations. Errors introduced through the transient part does not accumulate to any noticeable amount. The waves that propagate as a result of the linearly increasing flow from zero to the steady state value of 100 ml/s are very long. Thus these tests are not very challenging for the methods. Any errors introduced by the use of Riemann invariants (linearizing the governing equations) are not prominent. As a result these tests may be seen as a verification of the implemented bifurcation model, but cannot be used to depict the accuracy of the Riemann invariants.

8.1.7 Methods used in STARFiSh's contribution to Comparison1D-scheme

Based on the results/findings presented and discussed in the eight tests above the final solutions used as STARFiSh's solutions in the article were run with the new conservative scheme, and nonlinear link/bifurcation model (where applicable). Moreover the convective correction factor in all tests was set to one, to be compatible with the other schemes. The Δt and spatial discretization used are based on the the results from Sect. 6, Grid-adaption and is summarized in Table 33

8.2 Womersley

A lot more tests should be done on the womersleymodel. However some things can be noted from the few tests made in Sect. 7.2. The flow is regained after the change from time-domain to frequency-domain, and back again. On the test on ThoA the effect off Womersley-aplication on the convective term is almost negligible. Thus assuming a flat profile, or a power-law velocity profile are good estimations in regards to the convective term in this test. This is also in accordance with the findings in Sect. 8.1.3, and Stergiopulos *et al.* [46]. Looking at the velocity profiles comparing womersley and power-law ($\zeta = 9$), they are quite similar and also close to flat in systole (Fig. 28). They differ more in diastole, but this is a period when the Windkessel effect is dominent, and the velocityprofile is not important.

The effect of womersleytheory on the friction-term is noticeable in the test with ThoA. One could argue that the solution for the pressure-gradient with womersley application on the friction term in Fig. 24 follow a path that is more similar to the 3D solution. However looking at the error-metrics in Table 17, the solutions with womersleytheory are all less in accordance with the 3D solution, than the solutions without womersleytheory. Thus all the simplifications and assumptions made in the 1D-solutions, all introduce more errors, and uncertainties in wall models etc. overshadows the effect of womersleytheory. At least in this test.

In bigger networks, in which the velocity profile likely varies from Pouseille flow in small arteries, to almost flat profiles in aortic segments, the womersley application on the convective and friction term is likely more important. For instance looking at the ADAN55 model, the entire

network is assumed to have a Pouseille ($\zeta = 2$) velocity-profile. In aortic regions the velocity-profile will be similar to those obtained in this test (Fig. 28). The effect of using Womersley theory would likely be noticeable. It also reduce the number of uncertain parameters (ζ).

8.3 Future work

All the tests and data that now are available for STARFiSh, through the project Comparison1Dscheme form a brilliant basis for benchmarking future implementations of STARFiSh. The test-case adan55 is in my opinion an especially good test case, being the most demanding test for the numerical methods. As mentioned there are still some unresolved questions regarding the big dependence on grid in this test. More work should be done in figuring out the reason for this. I believe the grid-dependence is more related to the handling of the bifurcations than to the field equations. More tests should be done to validate the methods used in the bifurcation model. Is there a difference between our way of handling the Riemann invariants (discretization of the pressure, flow, and velocity with the Riemann-invariants), and the way the other schemes handle it.

The findings in this Thesis revealed that the original implementation of the MacCormack scheme was non-conservative. The new scheme seem to be much more in accordance with the other schemes, and has not given any signs of being non-conservative. Still I argue that there are some non-Conservative aspect of the governing equations written in terms of the P,Q variables. Most importantly it requires an evaluation of the Compliance C, in the calculations in the mass equation. However where to evaluate this in order to ensure conservation of mass is not obvious. A related, but probably less important evaluation of the Area in the pressure term in the momentum equation is also needed. Looking at the governing equations written in terms of their A,U variables this numerical problem is avoided in both conservation equations. The A, Q system avoids this problem in the mass equation. Of the six schemes compared in this Thesis, only the McC (STARFiSh) and TP scheme use the P, Q variables. Tests should be made to figure out if the P,Q system introduce unnecessary internal flux errors.

Using the current implementations of STARFiSh, one should be aware when initializing the simulations. Quite some time have been spent on strange results due to wrong initialization. The tests; CCA, ThoA, AoBIf and Benchmark test are all based on a prescribed total flow. In addition the flow at time zero is not equal to one $Q(t = 0) \neq 0$. The current implementation of STARFiSh uses Δ values at boundaries If one initialize the network at the wrong value this error is not eliminated, but the next value (in time) is simply the initial value with a Δ value added to it. If one is not aware of this, and initialize the network with a different flow than the prescribed flow at time zero, the input and output will not be the same. Another related problem was encountered in the Single Resistance model. The current implementation assumes that the network is initilized in equilibrium $P = QR$. Thus, it will not converge to the correct solution if it is not initialized in equilibrium (This have likely introduced some unnecessary errors in BenchMark test). In my opinion this model should be reimplemented. This may be the case for other boundary models.
Also some problems was encountered using the Auto initialization. It does not necessarily find the correct equilibrium (in Adan55 it is way of), and it does not necessarily cut the simulation at the correct time (in Benchmark test, Auto initialization was used, but I needed to shift the solution myself in order for it to be in accordance with the inflow).
This is all something one should be aware of when initializing for solutions. In my opinion,

the handling of the Boundary-conditions with using Δ values, and the methods for initializations should be checked more thoroughly. Or one should at least check that the input and output is the same, and that the governing equations are really satisfied ($P = QR$ for instance).

More tests should be done on the new link/bifurcation model. Tests should be done regarding number of iterations needed to satisfy the equations with enough accuracy. More challenging/nonlinear tests could also be performed.

The Womersley model that I have suggested, have not been implemented in STARFiSh. Thus this still remain. Also the model I suggest is very time consuming, and more work could be done to reduce the computational time. The model is based on previous work done by Hallvard Moian Nydal. I would like to point out that I think that his treating of the convective term might be wrong. To calculate the convective term using Womersley theory one need to evaluate the term $\left(\int_A u^2 \mathrm{d}A\right)$, not the term $\frac{Q^2}{A}$.

See also table in Sect. 8.1.4 for a discussion on grid-dependence in ADAN55 model.

9 Results Comparison1Dscheme

We first compare the solutions given by the six numerical schemes described above in a series of simple test cases: a model of blood flow in a reflection-free tube for which a theoretical solution exists in the limit of almost negligible fluid velocity (Section 9.1), and models of blood flow in the human common carotid artery (Section 9.2), upper thoracic aorta (Section 9.3) and aortic bifurcation (Section 9.4), for which 3-D solutions are available from [57]. We then assess the six schemes in two different arterial networks: a 37-artery model of the aorta and its largest branches for which *in vitro* pressure and flow waveforms were acquired in [26] (Section 9.5), and the ADAN55 model by Blanco *et al.* [12], which contains the largest 55 systemic arteries of the human circulation (Section 9.6). For each test case, we provide graphical comparisons supported by tabulated calculations of relative errors. Table 33 shows the time step, characteristic spatial discretization (characteristic length of Ω_e), and space and time accuracies for each scheme.

9.1 Single pulse propagation in a straight reflection-free vessel

Figure 34 shows the dimensionless pressure wave at different times along the length of the tube. The inflow has a width of approximately 0.05 s and an initial wave speed of $c_0 = 6.17$ m s^{-1}, giving a wavelength of about $c_0 T \approx 31$ cm. This is a short wavelength compared with the 10 m long vessel, which enables showing the full shape of the pulse wave as it propagates along the vessel. For the inviscid problem, theoretical pressure and flow waveforms are in phase, have a constant amplitude, and propagate to the right with a wave speed given by Eq. (19) [4]. These theoretical results are well predicted by all six numerical schemes. In particular, the peak magnitude of the pressure wave ($P_{\text{peak,inv}}$) decreases by less than 2.2%, relative to the peak magnitude at the inlet, as it travels the length of the vessel. For the viscous problem, the peak magnitude of the pressure wave ($P_{\text{peak,visc}}$) decreases with distance x from the inlet, with good agreement between numerical results and the asymptotic exponential damping rate given by the theoretical solution

$$P_{\text{peak,visc}}(x) = P_{\text{peak,inv}} \exp\left(\frac{(\zeta+2)\pi\mu x}{\rho\, c_0 A_0}\right), \tag{67}$$

where c_0 is the pulse wave velocity at the initial area A_0. This theoretical solution is indicated by the thick black line in each panel of Fig. 34.

9.2 Common carotid artery

Figure 35 shows the pressure, pressure gradient (difference between inlet and outlet pressures), flow, and variations in luminal radius with time at the midpoint of the vessel obtained by solving the 1-D equations using all six schemes. These waveforms are almost identical to the corresponding waveforms calculated by solving the Navier-Stokes equations in a 3-D domain with compatible geometrical and mechanical properties and identical inflow and outflow boundary conditions [57]. Relative errors were determined with respect to the 3-D solution and are presented in Table 34. Pressure and flow errors are smaller than errors in pressure gradient and variations in radius, with no significant differences between the six schemes. Relative root mean square errors are smaller than 1.0% for pressure, the flow and change in radius, and smaller than 5.0% for the pressure gradient.

9.3 Upper thoracic aorta

Figure 36 presents numerical results for the pressure, pressure gradient, flow rate, and variations in luminal radius with time at the midpoint of the segment. They are calculated for all six numerical schemes and compared with the corresponding 3-D solutions. The 1-D solutions are similar to each other, with the largest differences with respect to the 3-D results observed during the systolic part of the cardiac cycle. The smallest relative errors are for the pressure and the largest for the pressure gradient (Table 35). Relative root mean square errors are all smaller than 3% for the pressure, flow and change in radius, and smaller than 8% for the pressure gradient.

9.4 Aortic bifurcation

Figure 37 displays the waveforms for pressure, flow rate, and variations in luminal radius at three points: the midpoint of the aorta, end point of the aorta and midpoint of either iliac artery. All these waveforms are similar among the six schemes and compare well with the corresponding 3-D model waveforms. Relative errors were determined with respect to the 3-D solution and are shown in Table 36. Relative errors for the pressure and flow rate are consistently smaller than for the change in radius, with no significant differences between the six schemes. Relative root mean square errors are all smaller than 1.2% for the pressure and flow, and smaller than 4.4% for the variation in radius.

9.5 Benchmark (in vitro)

Comparisons between experimental and numerical pressure and flow waveforms are shown in Fig. 38 for the aorta, and in Figs. 39, 40 and 41 for vessels of the first, second and third generation of bifurcations, respectively. All six numerical schemes are able to capture the main features of *in vitro* pressure and flow waveforms at the eight arterial sites investigated. However, numerical predictions overestimate the amplitude of the high-frequency oscillations observed in the *in vitro* pressure and flow waveforms of vessels of the second (Fig. 40) and third (Fig. 41) generation of bifurcations. Table 37 shows relative errors calculated with respect to *in vitro* measurements at the eight arterial vessels studied. Relative errors for the pressure are all consistently smaller than for the flow rate, with no significant differences between the six schemes. Relative root mean square errors are all smaller than 4% for the pressure and smaller than 26% for the flow rate.

9.6 ADAN55 model

Comparisons of pressure and flow rate waveforms obtained using the different numerical techniques are shown in Fig. 42 for three aortic segments, in Fig. 43 for first-generation vessels, in Fig. 44 for second-generation vessels, and in Fig. 45 for third- and fourth-generation vessels. There is an excellent agreement among all waveforms generated by the DG, LCG, FEM, FVM and McC methods; differences cannot be appreciated in the scale of the figures. Some discrepancies, however, can be observed between these waveforms and those provided by the STM scheme. In addition, Fig. 46 presents a comparison of the pressure variation throughout the aorta at several time instants during the cardiac cycle. These results also illustrate how changes in material properties and branching affect the pressure flow waveforms throughout the cardiac period. In the ADAN55 model, the first major branches of the aorta are situated at about 30 cm downstream of the aortic root, affecting the pressure waves as observed in Fig. 46.

Lastly, Fig. 47 shows that all six schemes produce similar diastolic pressures along the aorta. Some discrepancies are observed for systolic and mean pressures for the STM scheme, where it overestimates systolic pressures by about 1% in proximal locations and underestimates them by about 3% in distal locations, relative to the values calculated by the other five methods.

10 Discussion Comparison1Dscheme

We have compared the solution provided by six distinct numerical schemes for nonlinear 1-D blood flow modelling in a set of benchmark test cases. The schemes were chosen to embrace a variety of numerical techniques for the numerical solution of the 1-D formulation: finite element (DG, FEM, LCG, STM), finite volume (FVM) and finite difference (McC) methods. In this study, we have considered the widely used form of the 1-D equations (6) and (8), which accounts for nonlinear effects and is able to provide physiological features of human pulse waveforms.

Our study has been motivated by the scarceness of test cases for benchmarking 1-D numerical schemes, as well as by our desire to provide an accessible reference dataset. To address this gap in the literature, we have chosen six test cases that collectively provide a comprehensive framework for the development and assessment of other numerical schemes. With this aim in mind, we have fully described all test cases in Sections 9.1 to 9.6 and have provided, as supplementary material, all numerical and *in vitro* data used in this study for benchmarking 1-D numerical schemes. The test cases range from a simple, non-physiological, reflection-free, single tube, to more physiological single-vessel models, to network models simulating blood flow in the largest arteries of the human systemic circulation under normal physiological conditions. In Sections 10.1 to 10.3 we discuss the value of each test case for benchmarking 1-D schemes and examine similarities and discrepancies in the solutions computed by the DG, LCG, FEM, FVM, McC and STM methods.

10.1 Single pulse model

In the linear regime (i.e. for small and constant average velocity), a theoretical solution exists for the propagation of a narrow Gaussian-shaped wave in a reflection-free vessel, for both inviscid and viscous flow. This wave, which features a small wavelength compared to the vessel length ($\approx$ 31 cm versus 10 m, Fig. 34), is a continuous approximation to the unit pulse $\delta(t-t_0)$, $t_0 = 0.05$ s (*i.e.* $\delta(t_0) = 1$ and $\delta(t) = 0$ for $t \neq t_0$). Thus, very high frequencies dominate the Gaussian-shaped wave considered here. The single-pulse model, therefore, enables us to assess the ability of numerical schemes to solve the 1-D equations correctly and, in particular, to propagate high-frequency pulse waves. Numerically this is more challenging than the propagation of low-frequency pulse waves. Capturing the correct propagation of high-frequency waves is important for simulating arterial pulse wave hæmodynamics under physiological conditions, since high frequencies are responsible for relevant features of pulse waveforms; *e.g.* the feet of pressure, flow and area waveforms, and the dicrotic notch in the aortic pressure waveform.

Our results have shown the ability of all six schemes to solve correctly Eqs. (6) and (8) in the single-pulse model. For the FEM, FVM, McC and STM schemes, the high frequency and low wavelength of the Gaussian wave require a smaller spatial discretisation, compared to the discretisation employed in the other more physiological cases (Table 33). The DG method needs a higher space accuracy (order 10) than in the other test cases. The LCG approach involves more elements than the DG method (5000 versus 250), since the former has a linear accuracy in space. The FVM presents a compromise between number of elements used to discretize the spatial domain (1000) and time step, since 4-th order accuracy in space and time is used. The time step must be drastically reduced in the FEM, because the method is first order and the wavelength is short with respect to the vessel length. Moreover, CFL numbers must be very

close to one for the McC scheme to avoid dispersive errors.

10.2 Physiological single artery models

We have considered two additional single-vessel test cases under normal physiological conditions and for which 3-D solutions are available from [57]. These have allowed us to show that the six 1-D model schemes are able to capture the main features of 3-D model pressure, flow and area waveforms in two large arteries: the common carotid artery (Fig. 35) and the upper thoracic aorta (Fig. 36). For all six schemes, relative errors were consistently smaller for the carotid (Table 34) than aorta (Table 35) model. This is due to inertial forces playing a larger role in the aorta model; the peak Reynolds number is nearly an order of magnitude greater in the aorta model [57]. As a result, for the aorta model, the nonlinear convective acceleration term in the balance of momentum equation in (1b) has a more significant weight relative to the other terms, making it a more challenging test for 1-D schemes. Larger wall strains ($\Delta r/r_{\mathrm{d}}$) in the aorta model were also identified in [57] as an additional source of discrepancy between 1-D and 3-D modelling. Moreover, relative errors in the aorta model decrease during the diastolic part of the cardiac cycle, since the physics of blood flow becomes increasingly linear and inertia-free with the increasing time in diastole [55].

Compared to the single-pulse test case, pulse wavelengths in the carotid and aorta cases are much longer. These lengths can be approximated by multiplying the period of the systolic part of the inflow wave (T_{s}) with the pulse wave speed at mean pressure (c_{m}); we obtain $T_{\mathrm{s}}c_{\mathrm{m}} = 2.7$ m for the carotid test and $T_{\mathrm{s}}c_{\mathrm{m}} = 1.8$ m for the aorta test. As a result, the numerical parameters of all six numerical schemes can be relaxed (Table 33): the time step can be increased by a factor of 10^3 in the FEM and of 10 in STM, the order of the space accuracy can be dropped for both DG and FVM, and lowering the CFL number does not critically increase dispersive and diffusive errors for the McC scheme. Similarly for the LCG scheme, the solutions for both the carotid and aortic models are obtained with a significantly smaller number of elements than for the single-pulse model.

10.3 Physiological network models

The three additional test cases that we have used to assess 1-D numerical schemes contain arterial bifurcations – a key anatomical feature for blood flow modelling in the arterial tree. These are a single-bifurcation model and the 37- and 55-artery models of blood flow in the systemic arterial network, which contain multiple bifurcations. They allow us to verify the ability of each scheme to deal with multiple reflections generated at a junction, where continuity and compatibility conditions are imposed (Section 3.7.2).

The single-bifurcation model provides a test for benchmarking the connection of three 1-D model vessels through a bifurcation under normal physiological conditions. This test simulates blood flow in the abdominal aorta and its bifurcation into the two iliac arteries that perfuse the legs. For this test, a 3-D solution is available from [57] to assess the accuracy of 1-D schemes. All six 1-D schemes considered here are able to capture the multiple wave reflections generated at the bifurcation, which shape pressure, flow and area waveforms in the aorta and iliac arteries (Fig. 37). All numerical schemes yield comparable relative errors (Table 36), despite the dynamic part of pressure ($1/2\rho U^2$) being neglected in the STM scheme. This is because $1/2\rho U^2$ is small compared to the hydrostatic pressure (P) at the bifurcation. Moreover, relative root

mean square errors are smaller than for the single-aorta test and similar to the common carotid test, since peak Reynolds numbers are of similar order of magnitude for both the carotid and bifurcation cases.

The 37-artery model includes the aorta and its larger branches. For this case, *in vitro* pressure and flow waveforms were acquired in [26], which has allowed us to test the accuracy of the six 1-D schemes. These are all able to reproduce the main features of pressure and flow waveforms measured *in vitro* (see Figs. 38 to 41), with relative errors smaller than 4% for pressure and 26% for the flow (Table 37). Discrepancies between experimental and numerical results arise from the uncertainties in the experimental measurements and the assumptions and simplifications of the 1-D formulation. According to [26], the larger relative errors in the flow predictions compared to their pressure counterparts can be explained because experimental flow measurements were less precise than experimental pressure measurements. Moreover, the greater amplitude of high-frequency oscillations in the peripheral vessels predicted by the numerical schemes, but not seen in the *in vitro* measurements, can be reduced by adding a visco-elastic component to the tube law defined by Eq. (8), as described in [1]. These oscillations, whose frequency is well predicted by all six methods, are produced by the resistive outflow boundary conditions used in the experimental set-up, which are non-physiological since they lack any peripheral compliance. Similarly to the single-bifurcation model discussed above, the dynamic part of pressure ($1/2\rho U^2$) was neglected in the STM. Given that the STM produces similar results to the other five methods we conclude that ($1/2\rho U^2$) does not play an important role in the 37-artery model.

The ADAN55 model simulates blood flow in the 55 larger arteries of the human systemic circulation. Arterial anatomy and mechanical properties, and inflow and outflow boundary conditions are all based on physiological human data. ADAN55, therefore, enables verification of numerical methods to solve 1-D haemodynamics under normal physiological conditions. For the ADAN55 model the six numerical schemes deliver pretty consistent solutions. Noticeable discrepancies are obtained with the STM in comparison to the rest of the numerical schemes (see Figs. (42) to (45)). Such larger differences are explained by the anatomical configuration of the ADAN55 model, which makes the model more sensitive to the coupling strategy at junctions. Recall that in the STM strategy the dynamic pressure is neglected when coupling vessels at junctions. Furtheremos, differences between models are more visible when zooming in the pressure along the aorta (see Fig. (46)). Except for the coupling strategy in the STM discussed above, the rest of the differences can be explained by discretization errors, just as occurred with the high frequency oscillations in the 37-artery model.

Using the 37-artery and ADAN55 test cases we have shown the ability of all six numerical methods to solve the nonlinear 1-D equations accurately and to capture the main features of pulse wave propagation in networks made up of large arterial segments. This is consistent with the outcome of previous studies [47, 37, 33, 32, 45, 56, 41, 8, 1, 39, 21, 57].

11 Conclusions

The results from the eight tests performed in this Thesis revealed that the original solving-scheme in STARFiSH is non-conservative. The non-conservative aspects are only prominent in tests with big relative weight on the convective term. The original Matrix formulation should not form the basis of the solving scheme, but is only needed to perform the characteristic analysis used in handling of boundary-conditions. Adan55 test also revealed that the bifurcation model based on continuity of static pressure can deviate a lot from the model based on continuity of total pressure. As a result a new solving-scheme and bifurcation model have been implemented. The models have been validated in cases where analytical solutions exist. Moreover the new scheme have showed to conserve flow-rate and pressure in all tests.

The findings from the grid-adaption show that for physiological cases with corresponding long wavelengths, relatively low CFL numbers can be tolerated. Dispersive and Diffusive errors introduced by low CFL numbers are small comparing with 3D and experimental data.

With the new implementations we have shown that arterial pulse wave haemodynamics can be accurately simulated using finite element, finite volume or finite difference methods. All six schemes considered in this study have been assessed in a series of benchmark test cases with increasing degree of complexity, for which theoretical, numerical 3-D or *in vitro* pulse waveforms are available. Results have shown a good agreement among all numerical schemes and their ability to capture the main features of pressure, flow and area waveforms in large arteries. This study have provided additional support for the use of 1-D reduced modeling to accurately simulate arterial pulse wave haemodynamics with a reasonable computational cost. The test cases used in this study can be applied to facilitate the development and assessment of future numerical schemes for the correct solution of the 1-D equations of blood flow in networks of compliant arteries.

The model which integrates Womersley theory with 1-D compliant vessel flow did not yield a better solution than the standard model based on assumed velocity-profiles, comparing with 3-D data in a test replicating blood flow in the thoracic aorta. The effect of Womersley theory is likely more noticeable in bigger networks, which has regions with high and low Reynolds-number.

Bibliography

[1] J. Alastruey, A.W. Khir, K.S. Matthys, P. Segers, S.J. Sherwin, P. Verdonck, K.H. Parker, and J. Peiró. Pulse wave propagation in a model human arterial network: Assessment of 1-D visco-elastic simulations against *in vitro* measurements. *J. Biomech.*, 44:2250–2258, 2011.

[2] J. Alastruey, S.M. Moore, K.H. Parker, T. David, J. Peiró, and S.J. Sherwin. Reduced modelling of blood flow in the cerebral circulation: Coupling 1-D, 0-D and cerebral auto-regulation models. *Int. J. Numer. Meth. Fluids*, 56:1061–1067, 2008.

[3] J. Alastruey, K.H. Parker, and S.J. Sherwin. *Arterial pulse wave haemodynamics. In Anderson (Ed.) 11th International Conference on Pressure Surges*, chapter 7, pages 401–442. Virtual PiE Led t/a BHR Group (ISBN: 978 1 85598 133 1), 2012.

[4] J. Alastruey, T. Passerini, L. Formaggia, and J. Peiró. Physical determining factors of the arterial pulse waveform: theoretical analysis and estimation using the 1-D formulation. *J. Eng. Math.*, 77:19–37, 2012.

[5] A.P. Avolio. Multi-branched model of the human arterial system. *Med. and Biol. Engng. and Comput.*, 18:709–718, 1980.

[6] K. Azer and C.S. Peskin. A one-dimensional model of blood flow in arteries with friction and convection based on the Womersley velocity profile. *Cardiov. Eng.*, 7:51–73, 2007.

[7] Karim Azer and Charles S Peskin. A one-dimensional model of blood flow in arteries with friction and convection based on the womersley velocity profile. *Cardiovascular Engineering*, 2007.

[8] D. Bessems, C.G. Giannopapa, M.C.M. Rutten, and F.N. van de Vosse. Experimental validation of a time-domain-based wave propagation model of blood flow in viscoelastic vessels. *J. Biomech.*, 41:284–291, 2008.

[9] D. Bessems, M. Rutten, and F. van de Vosse. A wave propagation model of blood flow in large vessels using an approximate velocity profile function. *J. Fluid Mech.*, 580:145–168, 2007.

[10] P.J. Blanco, S.M. Watanabe, E.A. Dari, M.A.R.F. Passos, and R.A. Feijóo. Blood flow distribution in an anatomically detailed arterial network model: criteria and algorithms. *Biomech. Model. Mechanobiol.*, 13:1303–1330, 2014.

[11] PJ Blanco, SM Watanabe, and RA Feijóo. Identification of vascular territory resistances in one-dimensional hemodynamics simulations. *Journal of biomechanics*, 45(12):2066–2073, 2012.

[12] P.J. Blanco, S.M. Watanabe, M.A.R.F. Passos, P.A. Lemos, and R.A. Feijóo. An anatomically detailed arterial network model for one-dimensional computational hemodynamics. *IEEE Transactions on Biomedical Engineering*, 62:736–753, 2015.

[13] j Bramwell and A Hill. Comparison of numerical schemes for nonlinear 1-d blood flow modeling. *Proceedings of the royal society of London*, 45:298–306, 1922.

[14] D.J. Brown. Input impedance and reflection coefficient in fractal-like models of asymmetrically branching compliant tubes. *IEEE Trans. Biomed. Eng.*, 43:715–722, 1996.

[15] V. Eck, J. Feinberg, H.P. Langtangen, and L.R. Hellevik. Stochastic sensitivity analysis for timing and amplitude of pressure waves in the arterial system. *Int J Numer Method Biomed Eng*, 31(4), 2015. Epub.

[16] M.A. Fernández, V. Milišić, and A. Quarteroni. Analysis of a geometrical multiscale blood flow model based on the coupling of ODE's and hyperbolic PDE's. *SIAM J. Multiscale Mod. Sim.*, 4:215–236, 2005.

[17] L. Formaggia, D. Lamponi, and A. Quarteroni. One-dimensional models for blood flow in arteries. *J. Eng. Math.*, 47:251–276, 2003.

[18] Leif Rune Hellevik. Blood flow in compliant vessels.

[19] Leif Rune Hellevik, J. Vierendeels, T. Kiserud, N. Stergiopulos, F. Irgens, and E. Dick. An assessment of ductus venosus tapering and wave transmission from the fetal heart. *Biomech. Model. Mechanobiol.*, 8(6):509–517, 2009.

[20] Charles Hirsch. *Numerical Computation of Internal and External Flows, Volume 1: Fundamentals of Numerical Discretization.* Wiley, Brussel, 1989.

[21] W. Huberts, K. Van Canneyt, P. Segers, S. Eloot, J.H.M. Tordoir, P. Verdonck, F.N. van de Vosse, and E.M.H. Bosboom. Experimental validation of a pulse wave propagation model for predicting hemodynamics after vascular access surgery. *J. Biomech.*, 45:1684–1691, 2012.

[22] T.J.R. Hughes and J. Lubliner. On the one-dimensional theory of blood flow in the larger vessels. *Math. Biosciences*, 18:161–170, 1973.

[23] G.E. Karniadakis and S.J. Sherwin. *Spectral/hp Element Methods for Computational Fluid Dynamics.* Oxford University Press, 2005.

[24] Wilco Kroon, Wouter Huberts, Marielle Bosboom, and Frans van de Vosse. A Numerical Method of Reduced Complexity for Simulating Vascular Hemodynamics Using Coupled 0D Lumped and 1D Wave Propagation Models. *Computational and Mathematical Methods in Medicine*, 2012(Article ID: 156094), 2012.

[25] F.Y. Liang, S. Takagi, R. Himeno, and H. Liu. Biomechanical characterization of ventricular–arterial coupling during aging: A multi-scale model study. *J. Biomech.*, 42:692–704, 2009.

[26] K.S. Matthys, J. Alastruey, J. Peiró, A.W. Khir, P. Segers, P.R. Verdonck, K.H. Parker, and S.J. Sherwin. Pulse wave propagation in a model human arterial network: Assessment of 1-D numerical simulations against *in vitro* measurements. *J. Biomech.*, 40:3476–3486, 2007.

[27] LO Müller and EF Toro. Well balanced high order solver for blood flow in networks of vessels with variable properties. *International Journal for Numerical ...*, 29:1388–1411, 2013.

[28] LO Müller and EF Toro. A global multiscale mathematical model for the human circulation with emphasis on the venous system. *Int. J. Numer. Meth. Biomed. Engng.*, 30:681–725, 2014.

[29] LO Müller and EF Toro. An enhanced closed-loop model for the study of cerebral venous blood flow. *J. Biomech.*, 47:3361–3372, 2014.

[30] Lucas O Müller and Pablo J Blanco. A high order approximation of hyperbolic conservation laws in networks: application to one-dimensional blood flow. *Comp. Meths. Biomech. Biomed. Eng.*, 13:1704, 2013. submitted to the Journal of Computational Physics in January 2015.

[31] Lucas O Müller, Carlos Parés, and Eleuterio F Toro. Well-balanced high-order numerical schemes for one-dimensional blood flow in vessels with varying mechanical properties. *Journal of Computational Physics*, 242:53–85, 2013.

[32] J.P. Mynard and P. Nithiarasu. A 1D arterial blood flow model incorporating ventricular pressure, aortic valve and regional coronary flow using the locally conservative Galerkin (LCG) method. *Commun. Numer. Meth. Eng.*, 24:367–417, 2008.

[33] M.S. Olufsen, C.S. Peskin, W.Y. Kim, E.M. Pedersen, A. Nadim, and J. Larsen. Numerical simulation and experimental validation of blood flow in arteries with structured-tree outflow conditions. *Ann. Biomed. Eng.*, 28:1281–1299, 2000.

[34] K.H. Parker. A brief history of arterial wave mechanics. *Med. & Biol. Eng. & Comput.*, 47:111–118, 2009.

[35] K.H. Parker. An introduction to wave intensity analysis. *Med. Bio. Eng. Comput.*, 47:175–188, 2009.

[36] A. Quarteroni, S. Ragni, and A. Veneziani. Coupling between lumped and distributed models for blood flow problems. *Comput. Visual. Sci.*, 4:111–124, 2001.

[37] P. Reymond, Y. Bohraus, F. Perren, F. Lazeyras, and N. Stergiopulos. Validation of a patient-specific one-dimensional model of the systemic arterial tree. *Am. J. Physiol. Heart Circ. Physiol.*, 301:H1173–H1182, 2011.

[38] Philippe Reymond, Fabrice Merenda, Fabienne Perren, Daniel Rufenacht, and Nikos Stergiopulos. Validation of one-dimensional model of the systemic arterial tree. *AJP- Heart and Circulatory Physiology*, 2011.

[39] M. Saito, Y. Ikenaga, M. Matsukawa, Y. Watanabe, T. Asada, and P.-Y. Lagrée. One-dimensional model for propagation of a pressure wave in a model of the human arterial network: Comparison of theoretical and experimental results. *J. Biomech. Eng.*, 133:121005, 2011.

[40] B.W. Schaaf and P.H. Abbrecht. Digital computer simulation of human systemic arterial pulse wave transmission: a nonlinear model. *J. Biomech.*, 5:345–364, 1972.

[41] P. Segers, F. Dubois, D. De Wachter, and P. Verdonck. Role and relevancy of a cardiovascular simulator. *Cardiov. Eng.*, 3:48–56, 1998.

[42] S.J. Sherwin, L. Formaggia, J. Peiró, and V. Franke. Computational modelling of 1D blood flow with variable mechanical properties and its application to the simulation of wave propagation in the human arterial system. *Int. J. Numer. Meth. Fluids*, 43:673–700, 2003.

[43] S.J. Sherwin, V.E. Franke, J. Peiró, and K.H. Parker. One-dimensional modelling of a vascular network in space-time variables. *J. Eng. Maths.*, 47:217–250, 2003.

[44] N.P. Smith, A.J. Pullan, and P.J. Hunter. An anatomically based model of transient coronary blood flow in the heart. *SIAM J. Appl. Math.*, 62:990–1018, 2001.

[45] B.N. Steele, J. Wan, J.P. Ku, T.J.R. Hughes, and C.A. Taylor. *In vivo* validation of a one-dimensional finite-element method for predicting blood flow in cardiovascular bypass grafts. *IEEE Trans. Biomed. Eng.*, 50:649–656, 2003.

[46] N. Stergiopulos, D.F. Young, and T.R. Rogge. Computer simulation of arterial flow with applications to arterial and aortic stenoses. *J. Biomech.*, 25:1477–1488, 1992.

[47] J.C. Stettler, P. Niederer, and M. Anliker. Theoretical analysis of arterial hemodynamics including the influence of bifurcations. Part II: Critical evaluation of theoretical model and comparison with noninvasive measurements of flow patterns in normal and pathological cases. *Ann. Biomed. Eng.*, 9:165–175, 1981.

[48] C.G. Thomas, P. Nithiarasu, and R.L.T. Bevan. The locally conservative Galerkin (LCG) method for solving the incompressible Navier-Stokes equations. *Int. J. Numer. Meth. Fl.*, 57:1771–1792, 2008.

[49] EF Toro and A. Siviglia. Flow in collapsible tubes with discontinuous mechanical properties: mathematical model and exact solutions. *Communications in Computational Physics*, 13:361–385, 2013.

[50] F.N. van de Vosse and N. Stergiopulos. Pulse wave propagation in the arterial tree. *Annu. Rev. Fluid Mech.*, 43:467–499, 2011.

[51] J.J. Wang and K.H. Parker. Wave propagation in a model of the arterial circulation. *J. Biomech.*, 37:457–470, 2004.

[52] X. Wang, J.M. Fullana, and P.Y. Lagrée. Verification and comparison of four numerical schemes for a 1d viscoelastic blood flow model. *Comp. Meths. Biomech. Biomed. Eng.*, 18:1704, 2015.

[53] S.M. Watanabe, P.J. Blanco, and R.A. Feijóo. Mathematical model of blood flow in an anatomically detailed arterial network of the arm. *ESAIM: Mathematical Modelling and Numerical Analysis*, 47:961–985, 2013.

[54] N. Westerhof, P. Sipkema, G. Van Den Bos, and G. Elzinga. Forward and backward waves in the arterial system. *Cardiov. Res.*, 6:648–656, 1972.

[55] M. Willemet and J. Alastruey. Arterial Pressure and Flow Wave Analysis Using Time-Domain 1-D Hemodynamics. *Ann. Biomed. Eng. (EPub ahead of print)*, pages 1–17, 2014.

[56] M. Willemet, V. Lacroix, and E. Marchandise. Validation of a 1D patient-specific model of the arterial hemodynamics in bypassed lower-limbs: Simulations against in vivo measurements. *Med. Eng. Phys.*, 35:1573–1583, 2013.

[57] N. Xiao, J. Alastruey, and C.A. Figueroa. A systematic comparison between 1-D and 3-D hemodynamics in compliant arterial models. *Int. J. Numer. Meth. Biomed. Eng.*, 30:204–231, 2014.

A Tests

A.1 Benchmark (in vitro)

ID	LD	RD	l [cm]	r_p [cm]	r_d [cm]	R [Pa s/m^3]	name
1	2	8	3.6	1.44	1.3	-	Ascending aorta
2	4	3	2.8	1.1	0.73	-	Innominate
3	-	-	14.5	0.54	0.39	$2.67 \cdot 10^9$	R. carotid
4	5	-	21.8	0.44	0.33	-	R. subclavian 1
5	7	6	16.5	0.33	0.28	-	R. subclavian 2
6	-	-	23.5	0.21	0.21	$3.92 \cdot 10^9$	R. radial
7	-	-	17.7	0.21	0.21	$3.24 \cdot 10^9$	R. ulnar
8	9	10	2.1	1.3	1.25	-	Aortic arch 1
9	-	-	17.8	0.56	0.37	$3.11 \cdot 10^9$	L. carotid
10	11	15	2.9	1.25	1.18	-	Aortic arch 2
11	12	-	22.7	0.44	0.34	-	L. subclavian 1
12	13	14	17.5	0.34	0.28	-	L. subclavian 2
13	-	-	24.5	0.21	0.21	$3.74 \cdot 10^9$	L. radial
14	-	-	19.1	0.21	0.21	$3.77 \cdot 10^9$	L. ulnar
15	16	17	5.6	1.18	1.1	-	Thoracic aorta 1
16	-	-	19.5	0.41	0.32	$2.59 \cdot 10^9$	Intercostals
17	23	18	7.2	1.1	0.93	-	Thoracic aorta 2
18	19	20	3.8	0.4	0.4	-	Celiac 1
19	22	21	1.3	0.43	0.43	-	celiac 2
20	-	-	19.1	0.18	0.18	$3.54 \cdot 10^9$	Splenic
21	-	-	19.8	0.19	0.19	$4.24 \cdot 10^9$	Gastric
22	-	-	18.6	0.33	0.29	$3.75 \cdot 10^9$	hepatic
23	24	25	6.2	0.93	0.8	-	Abdominal aorta 1
24	-	-	12.0	0.26	0.26	$3.46 \cdot 10^9$	L. renal
25	27	26	0.7	0.79	0.79	-	Abdominal aorta 2
26	-	-	11.8	0.25	0.25	$3.45 \cdot 10^9$	R.renal
27	31	28	10.4	0.78	0.59	-	Abdominal aorta 3
28	29	-	20.5	0.39	0.34	-	R. iliac-femoral 1
29	30	-	21.6	0.34	0.23	-	R. iliac-femoral 2
30	35	34	20.6	0.23	0.21	-	R. iliac-femoral 3

31	32	-	20.1	0.4	0.33	-	L.iliac-femoral
32	33	-	19.5	0.33	0.23	-	L. iliac-femoral 2
33	37	36	20.7	0.23	0.21	-	L. iliac-femoral 3
34	-	-	16.3	0.16	0.16	$5.16 \cdot 10^9$	R.anterior tibial
35	-	-	15.1	0.15	0.15	$5.65 \cdot 10^9$	R. posterior tibial
36	-	-	14.9	0.16	0.16	$4.59 \cdot 10^9$	L. posterior tibial
37	-	-	12.6	0.16	0.16	$3.16 \cdot 10^9$	L. anterior tibial

Table 18: Parameters for BenchMark test model described in 4.5. It should be noted that the metrics in this table have been rounded to the second integer of the used units.

A.2 Benchmark (ADAN55 model)

N°	Artery name	Length [cm]	p. Radius [cm]	d. Radius [cm]	R_1 $[\frac{\text{dyn.s}}{\text{cm}^5}]$	R_2 $[\frac{\text{dyn.s}}{\text{cm}^5}]$	C $[\frac{\text{cm}^5}{\text{dyn}}]$
1	aortic arch I	7.441	1.595	1.295			
2	brachiocephalic trunk	4.735	0.673	0.616			
3	aortic arch II	0.960	1.295	1.257			
4	subclavian R I	1.574	0.490	0.418			
5	common carotid R	8.122	0.448	0.333			
6	vertebral R	20.445	0.134	0.134	18104	72417	3.129E-06
7	subclavian R II	4.112	0.418	0.230			
8	axillary R	12.000	0.230	0.208			
9	brachial R	22.311	0.208	0.183			
10	radial R	30.089	0.138	0.138	11539	46155	4.909E-06
11	ulnar R I	2.976	0.141	0.141			
12	common interosseous R	1.627	0.096	0.096			
13	ulnar R II	23.926	0.141	0.141	11749	46995	4.821E-06
14	posterior interosseous R	23.056	0.068	0.068	47813	191252	1.185E-06
15	external carotid R	6.090	0.227	0.227	9391	37563	6.032E-06
16	internal carotid R	13.211	0.277	0.277	5760	23041	9.833E-06
17	common carotid L	12.132	0.448	0.333			
18	aortic arch III	0.698	1.257	1.228			
19	external carotid L	6.090	0.227	0.227	9424	37696	6.011E-06
20	internal carotid L	13.211	0.277	0.277	5779	23118	9.801E-06
21	subclavian L I	4.938	0.490	0.348			
22	aortic arch IV	4.306	1.228	1.055			
23	vertebral L	20.415	0.134	0.134	19243	76972	2.944E-06
24	subclavian L II	4.112	0.348	0.230			
25	axillary L	12.000	0.230	0.208			
26	brachial L	22.311	0.208	0.183			
27	radial L	31.088	0.138	0.138	11332	45329	4.998E-06
28	ulnar L I	2.976	0.141	0.141			
29	common interosseous L	1.627	0.096	0.096			
30	ulnar L II	23.926	0.141	0.141	11976	47905	4.730E-06
31	posterior interosseous L	23.056	0.068	0.068	47986	191945	1.180E-06
32	thoracic aorta I	0.990	1.055	1.036			
33	posterior intercostal R	19.688	0.140	0.140	249127	996508	2.274E-07
34	thoracic aorta II	0.788	1.036	1.022			
35	posterior intercostal L	17.803	0.140	0.140	255583	1022333	2.216E-07
36	thoracic aorta III	1.556	1.022	0.992			
37	posterior intercostal R	20.156	0.155	0.155	232434	929735	2.437E-07
38	thoracic aorta IV	0.533	0.992	0.982			
39	posterior intercostal L	18.518	0.155	0.155	234425	937702	2.416E-07
40	thoracic aorta V	12.156	0.982	0.754			
41	thoracic aorta VI	0.325	0.754	0.749			

Table 19: Parameter dataset for the ADAN55 model (see Fig. 4). Data is rounded to an adequate number of decimal digits. See Supplementary Material for data in full detail.

N°	Artery name	Length [cm]	p. Radius [cm]	d. Radius [cm]	R_1 $[\frac{\text{dyn.s}}{\text{cm}^5}]$	R_2 $[\frac{\text{dyn.s}}{\text{cm}^5}]$	C $[\frac{\text{cm}^5}{\text{dyn}}]$
42	celiac trunk	1.682	0.335	0.321			
43	abdominal aorta I	1.399	0.749	0.732			
44	common hepatic	6.655	0.269	0.269	3349	13394	1.692E-05
45	splenic I	0.395	0.217	0.217			
46	left gastric	9.287	0.151	0.151	343394	1373574	1.650E-07
47	splenic II	6.440	0.217	0.217	4733	18933	1.197E-05
48	superior mesenteric	21.640	0.393	0.393	2182	8728	2.596E-05
49	abdominal aorta II	0.432	0.732	0.726			
50	renal L	2.184	0.271	0.271	2263	9051	2.503E-05
51	abdominal aorta III	1.198	0.726	0.711			
52	renal R	3.772	0.310	0.310	2270	9082	2.495E-05
53	abdominal aorta IV	5.409	0.711	0.643			
54	inferior mesenteric	9.024	0.208	0.208	23913	95652	2.369E-06
55	abdominal aorta V	4.222	0.643	0.590			
56	common iliac R	7.643	0.450	0.409			
57	common iliac L	7.404	0.450	0.409			
58	external iliac R	10.221	0.338	0.319			
59	internal iliac R	7.251	0.282	0.282	4146	16582	1.366E-05
60	femoral R I	3.159	0.319	0.314			
61	profunda femoris R	23.839	0.214	0.214	3427	13707	1.653E-05
62	femoral R II	31.929	0.314	0.269			
63	popliteal R I	13.203	0.269	0.237			
64	anterior tibial R	38.622	0.117	0.117	24525	98100	2.310E-06
65	popliteal R II	0.880	0.237	0.235			
66	tibiofibular trunk R	3.616	0.235	0.235			
67	posterior tibial R	38.288	0.123	0.123	21156	84625	2.677E-06
68	external iliac L	10.221	0.338	0.319			
69	internal iliac L	7.251	0.282	0.282	4158	16632	1.362E-05
70	femoral L I	3.159	0.319	0.314			
71	profunda femoris L	23.839	0.214	0.214	3429	13715	1.652E-05
72	femoral L II	31.929	0.314	0.269			
73	popliteal L I	13.203	0.269	0.237			
74	anterior tibial L	38.622	0.117	0.117	24533	98131	2.309E-06
75	popliteal L II	0.880	0.237	0.235			
76	tibiofibular trunk L	3.616	0.235	0.235			
77	posterior tibial L	38.288	0.123	0.123	21166	84662	2.676E-06

Table 20: Continuation of Table 19. Parameter dataset for the ADAN55 model (see Fig. 4). p.: proximal, d.: distal. Data is rounded to an adequate number of decimal digits. See Supplementary Material for data in full detail.

B Grid-adaption

B.0.1 CCA, ThoA and AoBif

table 23 to 29 are table showing error metrics for different CFL numbers and Δt performed on tests 4.2 to 4.4.

CFL	0.87	0.43	0.22	0.11	0.05
$\mathcal{E}_P^{RMS}$	0.2	0.2	0.2	0.2	0.19
$\mathcal{E}_{\Delta P}^{RMS}$	2.84	2.86	2.9	2.99	3.06
$\mathcal{E}_Q^{RMS}$	0.21	0.21	0.21	0.22	0.27
$\mathcal{E}_{\Delta r}^{RMS}$	0.82	0.82	0.82	0.83	0.81
$\mathcal{E}_P^{MAX}$	0.42	0.42	0.43	0.44	0.42
$\mathcal{E}_{\Delta P}^{MAX}$	15.78	15.88	16.06	16.4	16.69
$\mathcal{E}_Q^{MAX}$	1.03	1.04	1.06	1.08	1.37
$\mathcal{E}_{\Delta r}^{MAX}$	1.84	1.84	1.85	1.86	1.82
$\mathcal{E}_P^{SYS}$	-0.28	-0.28	-0.28	-0.29	-0.28
$\mathcal{E}_{\Delta P}^{SYS}$	-13.28	-13.36	-13.52	-13.83	-14.190
$\mathcal{E}_Q^{SYS}$	-0.56	-0.57	-0.59	-0.62	-0.95
$\mathcal{E}_{\Delta r}^{SYS}$	-1.71	-1.71	-1.72	-1.73	-1.7
$\mathcal{E}_P^{DIAS}$	0.26	0.26	0.26	0.25	0.25
$\mathcal{E}_{\Delta P}^{DIAS}$	5.08	5.02	4.89	4.65	
$\mathcal{E}_Q^{DIAS}$	0.24	0.24	0.24	0.23	0.11
$\mathcal{E}_{\Delta r}^{DIAS}$	0.0	0.0	0.0	0.0	0.0

Table 21: CCA. Calculated relative root mean square, maximum, systolic and diastolic errors for different maximum CFL numbers. All calculations are calculated according to equation 19. Δt for all the simulations is 0.1 ms, and the number of nodes is 161, 81, 41, 21 and 11, respectively

CFL	0.87	0.43	0.22	0.11	0.04
$\mathcal{E}_P^{RMS}$	0.2	0.2	0.2	0.2	0.2
$\mathcal{E}_{\Delta P}^{RMS}$	2.86	2.9	2.99	3.13	3.14
$\mathcal{E}_Q^{RMS}$	0.21	0.21	0.21	0.24	0.22
$\mathcal{E}_R^{RMS}$	0.84	0.85	0.85	0.85	0.83
$\mathcal{E}_P^{MAX}$	0.43	0.44	0.44	0.43	0.45
$\mathcal{E}_{\Delta P}^{MAX}$	16.32	16.5	16.86	17.4	17.22
$\mathcal{E}_Q^{MAX}$	1.04	1.06	1.09	1.27	1.03
$\mathcal{E}_R^{MAX}$	1.89	1.9	1.92	1.9	1.86
$\mathcal{E}_P^{SYS}$	-0.29	-0.3	-0.3	-0.3	-0.27
$\mathcal{E}_{\Delta P}^{SYS}$	-13.64	-13.8	-14.11	-14.62	-14.98
$\mathcal{E}_Q^{SYS}$	-0.58	-0.6	-0.64	-0.85	-0.55
$\mathcal{E}_R^{SYS}$	-1.77	-1.77	-1.79	-1.78	-1.69
$\mathcal{E}_P^{DIAS}$	0.26	0.26	0.26	0.25	0.26
$\mathcal{E}_{\Delta P}^{DIAS}$	4.89	4.77	4.52	4.17	4.52
$\mathcal{E}_Q^{DIAS}$	0.24	0.23	0.22	0.14	0.3
$\mathcal{E}_R^{DIAS}$	0.0	0.0	0.0	0.0	0.0

Table 22: CCA. Calculated relative root mean square, maximum, systolic and diastolic errors for different maximum CFL numbers. All calculations are calculated according to equation 19. Δt for all the simulations is 0.2 ms, and the number of nodes is 81, 41, 21, 11 and 5, respectively

CFL	0.87	0.43	0.22	0.11	0.05
$\mathcal{E}_P^{RMS}$	0.21	0.22	0.22	0.21	0.17
$\mathcal{E}_{\Delta P}^{RMS}$	2.94	3.06	3.29	3.36	3.32
$\mathcal{E}_Q^{RMS}$	0.22	0.22	0.23	0.23	1.47
$\mathcal{E}_R^{RMS}$	0.91	0.92	0.93	0.88	0.74
$\mathcal{E}_P^{MAX}$	0.45	0.46	0.48	0.46	0.31
$\mathcal{E}_{\Delta P}^{MAX}$	18.11	18.54	19.32	19.65	18.28
$\mathcal{E}_Q^{MAX}$	1.06	1.11	1.15	1.05	3.57
$\mathcal{E}_R^{MAX}$	2.05	2.06	2.09	1.95	1.57
$\mathcal{E}_P^{SYS}$	-0.35	-0.35	-0.36	-0.31	-0.23
$\mathcal{E}_{\Delta P}^{SYS}$	-14.71	-15.09	-15.79	-16.31	-16.12
$\mathcal{E}_Q^{SYS}$	-0.62	-0.67	-0.72	-0.63	-3.02
$\mathcal{E}_R^{SYS}$	-1.93	-1.94	-1.96	-1.81	-1.51
$\mathcal{E}_P^{DIAS}$	0.26	0.26	0.26	0.26	0.22
$\mathcal{E}_{\Delta P}^{DIAS}$	4.33	4.01	3.44	3.5	4.69
$\mathcal{E}_Q^{DIAS}$	0.22	0.2	0.21	0.28	-0.67
$\mathcal{E}_R^{DIAS}$	0.0	0.0	0.0	0.0	0.0

Table 23: CCA. Calculated relative root mean square, maximum, systolic and diastolic errors for different maximum CFL numbers. All calculations are calculated according to equation 19. Δt for all the simulations is 0.5 ms, and the number of nodes is 33, 17, 9 5 and 3 respectively

$CFLnumber$	0.72	0.35	0.18	0.09	0.04
$\mathcal{E}_P^{RMS}$	1.04	1.04	1.04	1.04	1.04
$\mathcal{E}_{\Delta P}^{RMS}$	4.03	4.03	4.03	4.02	4.02
$\mathcal{E}_Q^{RMS}$	1.04	1.03	1.03	1.03	1.03
$\mathcal{E}_{\Delta r}^{RMS}$	1.96	1.96	1.96	1.98	1.98
$\mathcal{E}_P^{MAX}$	3.94	3.94	3.95	3.96	3.96
$\mathcal{E}_{\Delta P}^{MAX}$	28.6	28.6	28.6	28.61	28.61
$\mathcal{E}_Q^{MAX}$	5.22	5.21	5.19	5.11	5.11
$\mathcal{E}_{\Delta r}^{MAX}$	10.55	10.55	10.56	10.61	10.61
$\mathcal{E}_P^{SYS}$	-0.79	-0.79	-0.79	-0.79	-0.79
$\mathcal{E}_{\Delta P}^{SYS}$	-8.34	-8.34	-8.33	-8.32	-8.323
$\mathcal{E}_Q^{SYS}$	-3.05	-3.05	-3.04	-3.01	-3.01
$\mathcal{E}_{\Delta r}^{SYS}$	-4.81	-4.81	-4.82	-4.84	-4.84
$\mathcal{E}_P^{DIAS}$	0.82	0.82	0.83	0.84	0.84
$\mathcal{E}_{\Delta P}^{DIAS}$	5.83	5.83	5.84	5.88	5.88
$\mathcal{E}_Q^{DIAS}$	2.55	2.55	2.54	2.51	2.51
$\mathcal{E}_{\Delta r}^{DIAS}$	0.05	0.05	0.05	0.05	

Table 24: Thoa. Calculated relative root mean square, maximum, systolic and diastolic errors for different maximum CFL numbers. All calculations are calculated according to equation 19. Δt for all the simulations is 0.1 ms, and the number of nodes is 327, 163, 81, 41 and 21, respectively

$CFLnumber$	0.71	0.35	0.18	0.09	0.04
$\mathcal{E}_P^{RMS}$	1.04	1.04	1.04	1.03	1.02
$\mathcal{E}_{\Delta P}^{RMS}$	4.05	4.05	4.04	4.02	3.94
$\mathcal{E}_Q^{RMS}$	1.05	1.04	1.04	1.03	0.96
$\mathcal{E}_R^{RMS}$	1.96	1.97	1.98	2.04	2.22
$\mathcal{E}_P^{MAX}$	3.93	3.93	3.94	3.98	3.76
$\mathcal{E}_{\Delta P}^{MAX}$	29.01	29.01	29.03	29.13	28.05
$\mathcal{E}_Q^{MAX}$	5.3	5.28	5.2	4.92	5.96
$\mathcal{E}_R^{MAX}$	10.53	10.54	10.58	10.71	10.58
$\mathcal{E}_P^{SYS}$	-0.79	-0.79	-0.8	-0.83	-0.95
$\mathcal{E}_{\Delta P}^{SYS}$	-8.37	-8.36	-8.36	-8.35	-8.91
$\mathcal{E}_Q^{SYS}$	-3.03	-3.02	-2.99	-2.97	-2.16
$\mathcal{E}_R^{SYS}$	-4.83	-4.84	-4.86	-5.0	-5.43
$\mathcal{E}_P^{DIAS}$	0.83	0.83	0.84	0.89	0.97
$\mathcal{E}_{\Delta P}^{DIAS}$	5.84	5.85	5.88	6.1	6.59
$\mathcal{E}_Q^{DIAS}$	2.53	2.53	2.5	2.43	2.62
$\mathcal{E}_R^{DIAS}$	0.05	0.05	0.05	0.04	0.0

Table 25: ThoA. Calculated relative root mean square, maximum, systolic and diastolic errors for different maximum CFL numbers. All calculations are calculated according to equation 19. Δt for all the simulations is 0.2 ms, and the number of nodes is 160, 80, 40, 20 and 10, respectively

$CFLnumber$	0.71	0.35	0.18	0.09	0.04
$\mathcal{E}_P^{RMS}$	1.04	1.04	1.04	1.03	1.06
$\mathcal{E}_{\Delta P}^{RMS}$	4.09	4.08	4.05	3.92	3.9
$\mathcal{E}_Q^{RMS}$	1.04	1.03	1.01	1.03	1.36
$\mathcal{E}_R^{RMS}$	1.99	2.01	2.11	2.33	2.78
$\mathcal{E}_P^{MAX}$	3.95	3.96	3.99	4.22	5.5
$\mathcal{E}_{\Delta P}^{MAX}$	29.47	29.52	29.41	27.43	18.98
$\mathcal{E}_Q^{MAX}$	5.27	5.14	4.83	6.07	9.61
$\mathcal{E}_R^{MAX}$	10.59	10.65	10.81	11.67	14.86
$\mathcal{E}_P^{SYS}$	-0.81	-0.82	-0.85	-1.03	-1.0
$\mathcal{E}_{\Delta P}^{SYS}$	-8.49	-8.47	-8.47	-9.52	-14.01
$\mathcal{E}_Q^{SYS}$	-2.97	-2.93	-2.89	-3.64	-2.56
$\mathcal{E}_R^{SYS}$	-4.91	-4.95	-5.11	-5.72	-5.93
$\mathcal{E}_P^{DIAS}$	0.85	0.87	0.93	1.03	1.25
$\mathcal{E}_{\Delta P}^{DIAS}$	5.91	5.97	6.23	7.03	10.05
$\mathcal{E}_Q^{DIAS}$	2.52	2.48	2.52	3.62	7.72
$\mathcal{E}_R^{DIAS}$	0.05	0.05	0.03	0.0	0.01

Table 26: ThoA. Calculated relative root mean square, maximum, systolic and diastolic errors for different maximum CFL numbers. All calculations are calculated according to equation 19. Δt for all the simulations is 0.5 ms, and the number of nodes is 64, 34, 16, 8 and 4, respectively

$CFLnumber$	0.81	0.41	0.19	0.09	0.04
$\mathcal{E}_P^{RMS}$	0.39	0.39	0.39	0.38	0.38
$\mathcal{E}_Q^{RMS}$	0.81	0.81	0.81	0.81	0.8
$\mathcal{E}_R^{RMS}$	1.84	1.85	1.85	1.85	1.83
$\mathcal{E}_P^{MAX}$	0.92	0.92	0.93	0.92	0.9
$\mathcal{E}_Q^{MAX}$	3.57	3.56	3.56	3.55	3.58
$\mathcal{E}_R^{MAX}$	5.04	5.05	5.05	5.04	5.0
$\mathcal{E}_P^{SYS}$	-0.79	-0.79	-0.8	-0.79	-0.77
$\mathcal{E}_Q^{SYS}$	-3.45	-3.45	-3.44	-3.43	-3.35
$\mathcal{E}_R^{SYS}$	-4.94	-4.95	-4.95	-4.94	-4.89
$\mathcal{E}_P^{DIAS}$	0.42	0.43	0.42	0.41	0.42
$\mathcal{E}_Q^{DIAS}$	1.78	1.78	1.78	1.77	1.77
$\mathcal{E}_R^{DIAS}$	0.01	0.01	0.01	0.01	0.0

Table 27: AoBif. Calculated relative root mean square, maximum, systolic and diastolic errors for different maximum CFL numbers. All calculations are calculated according to equation 19. Δt for all the simulations is 0.1 ms, and with 93, 47, 23, 11 and 5, nodes in the Aorta and both Iliac arteries, respectively

$CFLnumber$	0.71	0.35	0.18	0.11	0.07
$\mathcal{E}_P^{RMS}$	0.42	0.42	0.42	0.41	0.41
$\mathcal{E}_Q^{RMS}$	0.81	0.81	0.81	0.8	0.8
$\mathcal{E}_R^{RMS}$	1.92	1.92	1.93	1.9	1.9
$\mathcal{E}_P^{MAX}$	0.88	0.89	0.89	0.87	0.87
$\mathcal{E}_Q^{MAX}$	3.55	3.55	3.54	3.51	3.51
$\mathcal{E}_R^{MAX}$	5.17	5.17	5.18	5.11	5.11
$\mathcal{E}_P^{SYS}$	-0.76	-0.77	-0.78	-0.76	-0.76
$\mathcal{E}_Q^{SYS}$	-3.45	-3.45	-3.44	-3.39	-3.39
$\mathcal{E}_R^{SYS}$	-5.08	-5.09	-5.09	-5.02	-5.02
$\mathcal{E}_P^{DIAS}$	0.59	0.58	0.57	0.56	0.56
$\mathcal{E}_Q^{DIAS}$	1.79	1.79	1.79	1.78	1.78
$\mathcal{E}_R^{DIAS}$	0.01	0.01	0.01	0.01	0.01

Table 28: AoBif. Calculated relative root mean square, maximum, systolic and diastolic errors for different maximum CFL numbers. All calculations are calculated according to equation 19. Δt for all the simulations is 0.2 ms, and with 41, 21, 11, 7 and 5, nodes in the Aorta and both Iliac arteries, respectively

$CFLnumber$	0.88	0.71	0.53	0.35	0.18
$\mathcal{E}_P^{RMS}$	0.45	0.45	0.45	0.45	0.42
$\mathcal{E}_Q^{RMS}$	0.82	0.82	0.81	0.81	0.79
$\mathcal{E}_R^{RMS}$	2.06	2.06	2.06	2.07	2.0
$\mathcal{E}_P^{MAX}$	0.98	0.98	0.99	1.0	0.93
$\mathcal{E}_Q^{MAX}$	3.51	3.51	3.51	3.49	3.39
$\mathcal{E}_R^{MAX}$	5.48	5.48	5.49	5.5	5.31
$\mathcal{E}_P^{SYS}$	-0.89	-0.89	-0.9	-0.91	-0.85
$\mathcal{E}_Q^{SYS}$	-3.47	-3.47	-3.47	-3.45	-3.32
$\mathcal{E}_R^{SYS}$	-5.42	-5.42	-5.43	-5.43	-5.25
$\mathcal{E}_P^{DIAS}$	0.65	0.65	0.64	0.63	0.58
$\mathcal{E}_Q^{DIAS}$	1.81	1.81	1.81	1.81	1.79
$\mathcal{E}_R^{DIAS}$	0.0	0.0	0.0	0.0	0.0

Table 29: AoBif. Calculated relative root mean square, maximum, systolic and diastolic errors for different maximum CFL numbers. All calculations are calculated according to equation 19. Δt for all the simulations is 0.5 ms, and with 21, 16, 12, 8 and 5, nodes in the Aorta and both Iliac arteries, respectively

C Results STARFiSh

This Appendix contain additional Tables and figures that correspond to Sect. 7

C.1 AoBif

Tables showing errormetrics corresponding to Sect. 7.1.4.

	Aortamid					
	DCG	LCG	STM	McCMatrix1N	McCFlux1N	McCMatrix1L
$\mathcal{E}_P^{RMS}$	0.36	0.37	0.38	0.39	0.37	0.38
$\mathcal{E}_Q^{RMS}$	0.89	0.84	0.83	0.71	0.84	0.82
$\mathcal{E}_{\Delta r}^{RMS}$	2.47	2.45	2.51	2.43	2.47	2.45
$\mathcal{E}_P^{MAX}$	0.60	0.66	0.66	0.67	0.65	0.66
$\mathcal{E}_Q^{MAX}$	2.55	2.56	2.58	2.24	2.55	2.52
$\mathcal{E}_{\Delta r}^{MAX}$	4.03	3.99	3.98	3.90	4.00	3.94
$\mathcal{E}_P^{SYS}$	-0.51	-0.53	-0.53	-0.54	-0.53	-0.51
$\mathcal{E}_Q^{SYS}$	-2.51	-2.54	-2.56	-2.23	-2.53	-2.52
$\mathcal{E}_P^{DIAS}$	0.48	0.48	0.49	0.51	0.47	0.48
$\mathcal{E}_Q^{DIAS}$	1.16	1.16	1.17	1.03	1.16	1.17

Table 30: Calculated relative root mean square, maximum, systolic and diastolic errors (%), as defined in Eq. (56), for test cases corresponding to Fig. 16 or the aortic bifurcation (AoBif). Errors are determined at the midpoint of each segment.

	Iliacamid					
	DCG	LCG	STM	McCMatrix1N	McCFlux1N	McCMatrix1L
$\mathcal{E}_P^{RMS}$	0.45	0.44	0.47	0.45	0.44	0.44
$\mathcal{E}_Q^{RMS}$	0.89	0.65	0.68	0.66	0.62	0.66
$\mathcal{E}_{\Delta r}^{RMS}$	4.29	4.35	4.31	4.30	4.32	4.26
$\mathcal{E}_P^{MAX}$	0.82	0.84	0.92	0.86	0.85	0.85
$\mathcal{E}_Q^{MAX}$	2.25	2.01	1.80	2.00	1.94	2.02
$\mathcal{E}_{\Delta r}^{MAX}$	7.25	7.37	7.48	7.36	7.34	7.34
$\mathcal{E}_P^{SYS}$	-0.81	-0.81	-0.85	-0.83	-0.82	-0.81
$\mathcal{E}_Q^{SYS}$	-1.80	-1.81	-1.58	-1.84	-1.77	-1.79
$\mathcal{E}_P^{DIAS}$	0.53	0.54	0.57	0.55	0.53	0.54
$\mathcal{E}_Q^{DIAS}$	1.17	1.17	1.18	1.19	1.19	1.18

Table 31: Calculated relative root mean square, maximum, systolic and diastolic errors (%), as defined in Eq. (56), for test cases corresponding to Fig. 16 or the aortic bifurcation (AoBif). Errors are determined at the midpoint of each segment.

C.2 Benchmark test

	$\mathcal{E}_P^{RMS}$	$\mathcal{E}_Q^{RMS}$	$\mathcal{E}_P^{MAX}$	$\mathcal{E}_Q^{MAX}$	$\mathcal{E}_P^{SYS}$	$\mathcal{E}_Q^{SYS}$	$\mathcal{E}_P^{DIAS}$	$\mathcal{E}_Q^{DIAS}$
Aortic arch II								
DCG	1.78	3.59	-1.40	-0.42	12.32	29.58	8.78	-17.95
LCG	1.68	3.21	-1.02	-0.93	12.34	31.83	10.02	-16.93
STM	1.84	3.76	-1.39	-0.36	12.19	29.45	8.75	-17.99
McCMatrix1N	1.90	3.82	-1.68	-0.27	12.09	28.99	8.85	-17.94
McCFlux1N	1.94	3.97	-1.60	-0.12	12.11	29.40	8.81	-17.74
McCMatrixaL	1.88	3.84	-1.64	-0.24	12.09	28.96	8.60	-17.91
Thoracic aorta II								
DCG	2.36	5.29	-0.96	1.66	25.59	67.52	60.70	-39.65
LCG	2.17	5.03	-0.79	1.13	25.36	70.75	61.59	-35.47
STM	2.42	5.58	-0.98	1.69	25.37	65.32	61.16	-38.77
McCMatrix1N	2.44	5.54	-1.19	1.86	25.65	65.28	61.99	-40.00
McCFlux1N	2.53	5.70	-1.13	1.98	25.62	66.22	62.24	-38.74
McCMatrixaL	2.46	5.59	-1.17	1.83	25.51	64.82	61.31	-39.76
Left subclavian I								
DCG	3.09	6.13	-3.92	-3.97	14.31	38.39	-2.11	-11.57
LCG	3.12	6.06	-3.38	-4.63	13.87	34.76	-2.92	-11.33
STM	3.11	6.13	-3.80	-3.97	14.45	38.96	-1.18	-10.83
McCMatrix1N	3.17	6.42	-4.19	-3.82	14.24	38.14	-2.28	-10.68
McCFlux1N	3.11	6.35	-4.09	-3.69	14.31	38.25	-2.08	-10.92
McCMatrixaL	3.14	6.27	-4.12	-3.79	14.39	39.03	-1.57	-10.85
Right iliac-femoral II								
DCG	3.82	9.00	-2.20	-4.13	24.49	59.63	50.20	-39.72
LCG	3.97	9.69	-2.19	-5.57	24.17	61.14	49.23	-36.92
STM	3.75	9.32	-2.37	-4.17	24.12	60.41	51.29	-38.26
McCMatrix1N	3.82	9.03	-2.33	-4.15	25.21	60.01	52.22	-45.05
McCFlux1N	3.65	8.95	-2.33	-3.73	24.80	61.61	52.41	-40.21
McCMatrixaL	3.79	9.10	-2.46	-4.16	25.06	59.45	51.56	-45.97

Table 32: Calculated relative root mean square, maximum, systolic and diastolic errors (%), as defined in Eq. (56), for the aortic arch II and thoracic aorta II (Fig. 30), the left subclavian I and right iliac-femoral II (Fig. 31)

(a) Aortic Arch

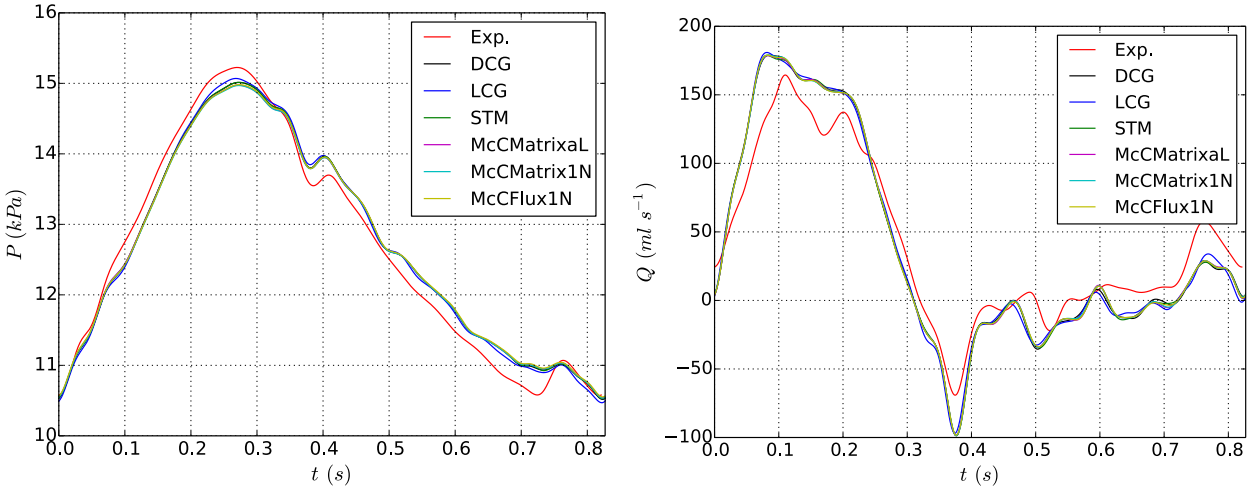

(b) Thoracic Aorta

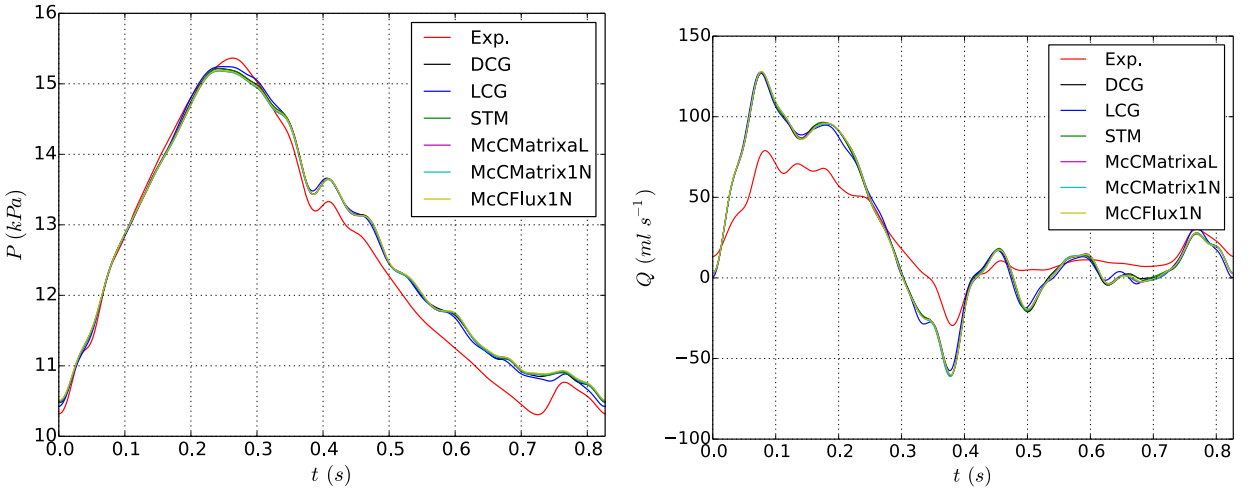

Figure 30: 37-artery network. Pressure (left) and flow (right) waveforms in the midpoint of two aortic segments: (a) aortic arch II and (b) thoracic aorta II. MacCCormack is STARFiSh with Matrix based scheme with linear bifurcation model, and convective correction factor calculated according to Eq. 4 (combination 6), McC is STARFiSh with Matrix based scheme with nonlinear bifurcation model, and convective correction factor set to one (combination 5), McCFlux is STARFiSh with Flux based scheme with nonlinear bifurcation model, and convective correction factor set to one (combination 3). *in vitro* data data (Exp.) measured in [26].

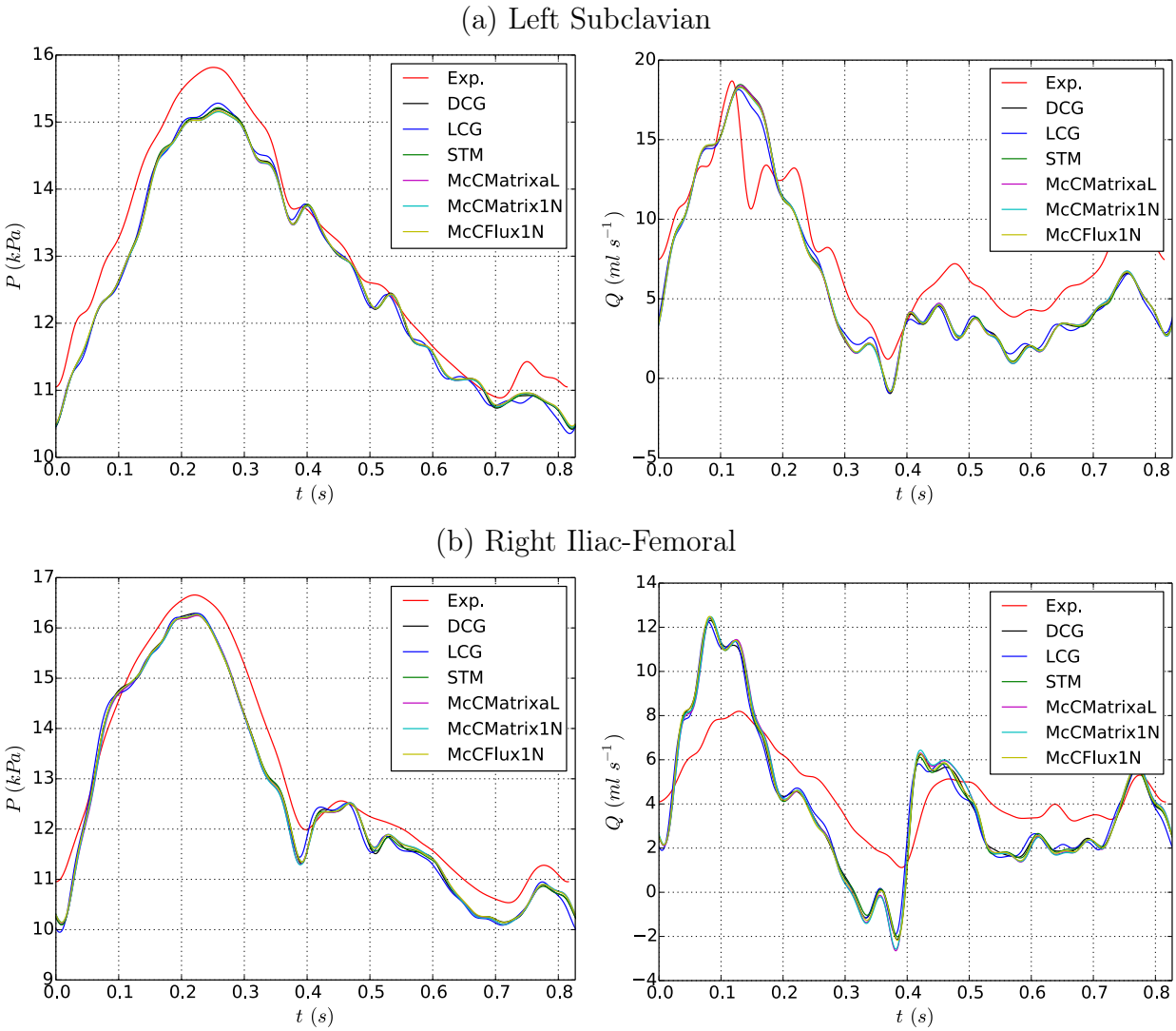

Figure 31: 37-artery network. Pressure (left) and flow (right) waveforms in the midpoint of two vessels from the first generation of bifurcations: (a) left subclavian I and (b) right iliac-femoral II. MacCCormack is STARFiSh with Matrix based scheme with linear bifurcation model, and convective correction factor calculated according to Eq. 4 (combination 6), McC is STARFiSh with Matrix based scheme with nonlinear bifurcation model, and convective correction factor set to one (combination 5), McCFlux is STARFiSh with Flux based scheme with nonlinear bifurcation model, and convective correction factor set to one (combination 3). *in vitro* data data (Exp.) measured in [26].

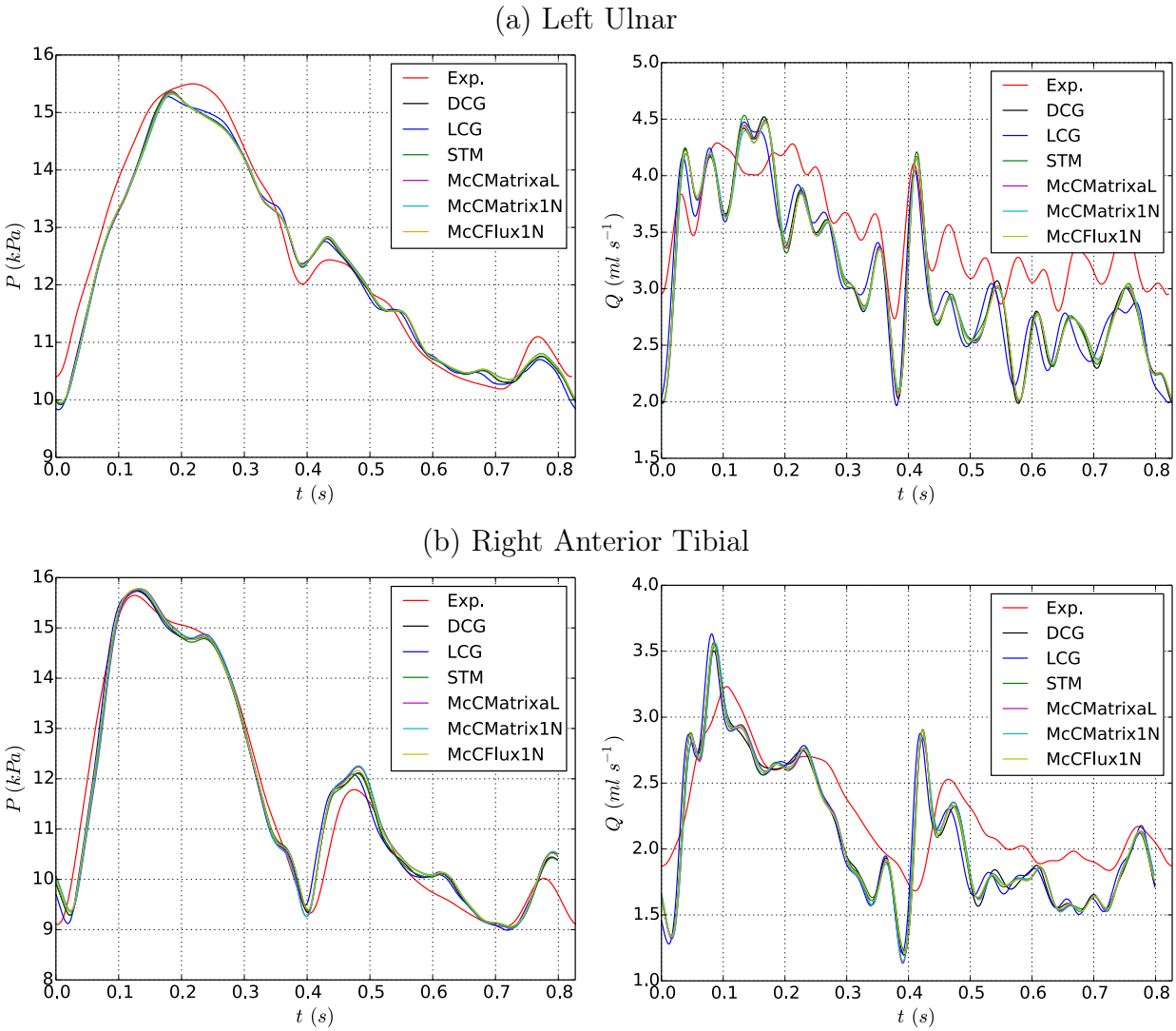

Figure 32: 37-artery network. Pressure (left) and flow (right) waveforms in the midpoint of two vessels from the second generation of bifurcations: (a) left ulnar and (b) right anterior tibial. MacCCormack is STARFiSh with Matrix based scheme with linear bifurcation model, and convective correction factor calculated according to Eq. 4 (combination 6), McC is STARFiSh with Matrix based scheme with nonlinear bifurcation model, and convective correction factor set to one (combination 5), McCFlux is STARFiSh with Flux based scheme with nonlinear bifurcation model, and convective correction factor set to one (combination 3). *in vitro* data data (Exp.) measured in [26].

(a) Right Ulnar

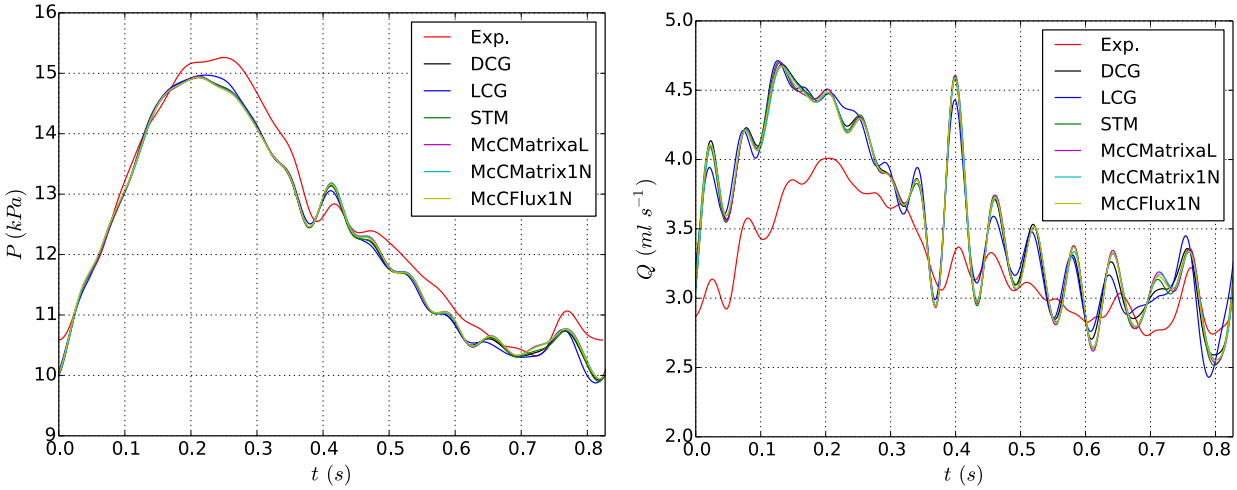

(b) Splenic

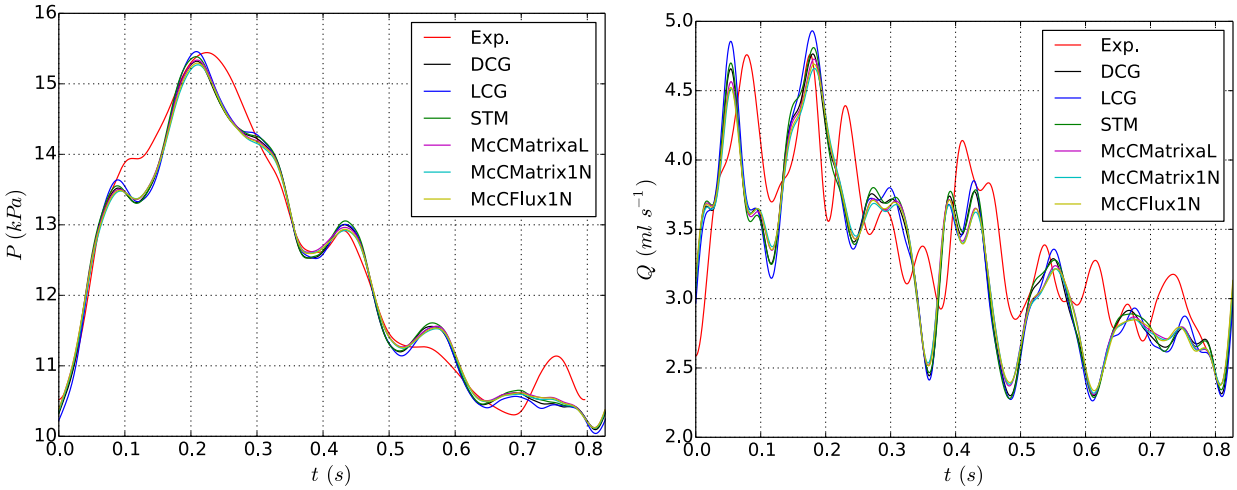

Figure 33: 37-artery network. Pressure (left) and flow (right) waveforms in the midpoint of two vessels from the third generation of bifurcations: (a) right ulnar and (b) splenic. MacCCormack is STARFiSh with Matrix based scheme with linear bifurcation model, and convective correction factor calculated according to Eq. 4 (combination 6), McC is STARFiSh with Matrix based scheme with nonlinear bifurcation model, and convective correction factor set to one (combination 5), McCFlux is STARFiSh with Flux based scheme with nonlinear bifurcation model, and convective correction factor set to one (combination 3). *in vitro* data data (Exp.) measured in [26].

D Comparison1Dscheme

D.1 tables

				Accuracy	
Case	Scheme	Δt	Ω_e	Space	Time
Single pulse	DG	0.1	4.00	10^{th}	2^{nd}
	LCG	0.01	0.20	1^{st}	2^{nd}
	FEM	0.0001	0.25	1^{st}	1^{st}
	FVM	1.457	1.00	4^{th}	4^{th}
	McC	0.25	0.156	2^{nd}	2^{nd}
	STM	0.1	0.10	1^{st}	2^{nd}
Carotid	DG	0.1	2.00	5^{th}	2^{nd}
	LCG	0.2	0.17	1^{st}	2^{nd}
	FEM	0.1	1.26	1^{st}	1^{st}
	FVM	3.27	2.00	2^{nd}	2^{nd}
	McC	0.5	0.39	2^{nd}	2^{nd}
	STM	1.0	1.00	1^{st}	2^{nd}
Aorta	DG	0.1	2.00	5^{th}	2^{nd}
	LCG	0.2	0.48	1^{st}	2^{nd}
	FEM	0.1	1.20	1^{st}	1^{st}
	FVM	3.31	2.00	2^{nd}	2^{nd}
	McC	0.5	0.71	2^{nd}	2^{nd}
	STM	1.0	1.00	1^{st}	2^{nd}
Ao. bifurcation	DG	0.1	2.00	5^{th}	2^{nd}
	LCG	0.2	0.17	1^{st}	2^{nd}
	FEM	1.0	0.86	1^{st}	1^{st}
	FVM	1.99	2.00	2^{nd}	2^{nd}
	McC	0.5	0.71	2^{nd}	2^{nd}
	STM	1.0	1.00	1^{st}	2^{nd}
37-Artery	DG	0.1	2.00	3^{rd}	2^{nd}
	LCG	0.1	0.175	1^{st}	2^{nd}
	FEM	0.1	1.00	1^{st}	1^{st}
	FVM	0.76	2.00	3^{rd}	3^{rd}
	McC	0.25	0.18	2^{nd}	2^{nd}
	STM	1.0	0.20	1^{st}	2^{nd}
ADAN55	DG	0.1	2.00	3^{rd}	2^{nd}
	LCG	0.01	0.065	1^{st}	2^{nd}
	FEM	1.0	0.50	1^{st}	1^{st}
	FVM	0.59	1.00	3^{rd}	3^{rd}
	McC	0.5	0.45	2^{nd}	2^{nd}
	STM	0.5	0.50	1^{st}	2^{nd}

Table 33: Numerical parameters for all six numerical schemes in the test cases considered in this study. The time step is Δt, and the characteristic spatial discretization is Ω_e.

Error	DG	LCG	FEM	FVM	McC	STM
$\mathcal{E}_P^{RMS}$	0.19	0.24	0.23	0.28	0.24	0.24
$\mathcal{E}_Q^{RMS}$	0.39	0.26	0.28	0.29	0.30	0.29
$\mathcal{E}_{\Delta r}^{RMS}$	0.94	1.00	1.00	1.07	1.01	0.98
$\mathcal{E}_{\Delta P}^{RMS}$	4.43	4.35	4.27	4.21	4.47	4.47
$\mathcal{E}_P^{MAX}$	0.30	0.52	0.50	0.66	0.52	0.53
$\mathcal{E}_Q^{MAX}$	1.21	1.02	1.12	1.07	1.20	1.13
$\mathcal{E}_{\Delta r}^{MAX}$	1.68	1.93	1.88	2.28	1.93	1.96
$\mathcal{E}_{\Delta P}^{MAX}$	16.69	16.17	15.88	15.60	16.58	16.90
$\mathcal{E}_P^{SYS}$	-0.26	-0.27	-0.26	-0.29	-0.27	-0.26
$\mathcal{E}_Q^{SYS}$	-0.54	-0.46	-0.54	-0.58	-0.62	-0.55
$\mathcal{E}_{\Delta r}^{SYS}$	-1.62	-1.63	-1.61	-1.68	-1.63	-1.63
$\mathcal{E}_{\Delta P}^{SYS}$	-15.11	-15.37	-15.16	-14.83	-15.73	-15.76
$\mathcal{E}_P^{DIAS}$	0.28	0.28	0.27	0.29	0.28	0.27
$\mathcal{E}_Q^{DIAS}$	0.26	0.22	0.26	0.24	0.23	0.27
$\mathcal{E}_{\Delta r}^{DIAS}$	0.07	0.11	0.08	0.12	0.09	0.08
$\mathcal{E}_{\Delta P}^{DIAS}$	4.98	4.76	5.03	4.91	4.45	4.85

Table 34: Relative errors (in %) as defined in Section 3.8 for the six numerical schemes at the midpoint of the common carotid artery.

Error	DG	LCG	FEM	FVM	McC	STM
$\mathcal{E}_P^{RMS}$	1.08	1.21	1.09	1.14	1.08	1.12
$\mathcal{E}_Q^{RMS}$	2.55	2.19	2.23	2.17	2.22	2.28
$\mathcal{E}_{\Delta r}^{RMS}$	2.30	2.41	2.33	2.44	2.33	2.90
$\mathcal{E}_{\Delta P}^{RMS}$	7.71	7.23	7.23	7.14	7.23	7.52
$\mathcal{E}_P^{MAX}$	3.55	3.55	3.26	3.18	3.27	3.30
$\mathcal{E}_Q^{MAX}$	9.12	7.20	7.04	7.07	7.04	7.40
$\mathcal{E}_{\Delta r}^{MAX}$	7.77	7.67	7.32	7.20	7.09	8.04
$\mathcal{E}_{\Delta P}^{MAX}$	31.86	29.31	29.15	29.13	29.31	31.19
$\mathcal{E}_P^{SYS}$	-0.55	-0.32	-0.56	-0.71	-0.55	-0.59
$\mathcal{E}_Q^{SYS}$	-5.57	-5.36	-5.63	-5.29	-5.58	-5.56
$\mathcal{E}_{\Delta r}^{SYS}$	-2.48	-1.93	-2.50	-2.86	-2.49	-4.48
$\mathcal{E}_{\Delta P}^{SYS}$	-8.97	-8.89	-9.29	-8.53	-9.04	-9.70
$\mathcal{E}_P^{DIAS}$	0.85	1.12	0.88	0.99	0.87	0.85
$\mathcal{E}_Q^{DIAS}$	2.70	2.67	3.09	3.48	2.67	2.95
$\mathcal{E}_{\Delta r}^{DIAS}$	1.86	2.24	1.89	2.05	1.89	0.00
$\mathcal{E}_{\Delta P}^{DIAS}$	7.28	7.24	7.60	6.37	7.32	7.47

Table 35: Relative errors (in %) as defined in Section 3.8 for the six numerical schemes at the midpoint of the upper thoracic aorta.

Site	Error	DG	LCG	FEM	FVM	McC	STM
Midpoint aorta	$\mathcal{E}_P^{RMS}$	0.36	0.39	0.37	0.40	0.38	0.38
	$\mathcal{E}_Q^{RMS}$	0.89	0.71	0.82	0.81	0.83	0.82
	$\mathcal{E}_{\Delta r}^{RMS}$	2.47	2.43	2.55	2.49	2.48	2.45
	$\mathcal{E}_P^{MAX}$	0.60	0.67	0.65	0.68	0.66	0.66
	$\mathcal{E}_Q^{MAX}$	2.55	2.24	2.53	2.44	2.56	2.52
	$\mathcal{E}_{\Delta r}^{MAX}$	4.03	3.90	4.03	4.01	3.98	3.94
	$\mathcal{E}_P^{SYS}$	-0.51	-0.54	-0.51	-0.55	-0.53	-0.51
	$\mathcal{E}_Q^{SYS}$	-2.51	-2.23	-2.52	-2.44	-2.55	-2.52
	$\mathcal{E}_{\Delta r}^{SYS}$	-3.92	-3.86	-3.99	-4.00	-3.94	-3.93
	$\mathcal{E}_P^{DIAS}$	0.48	0.51	0.47	0.53	0.49	0.48
	$\mathcal{E}_Q^{DIAS}$	1.16	1.03	1.16	1.16	1.17	1.17
	$\mathcal{E}_{\Delta r}^{DIAS}$	-1.41	-1.37	-1.49	-1.35	-1.40	-1.41
End point aorta	$\mathcal{E}_P^{RMS}$	0.42	0.43	0.41	0.44	0.42	0.42
	$\mathcal{E}_Q^{RMS}$	1.19	1.13	1.12	1.08	1.12	0.46
	$\mathcal{E}_{\Delta r}^{RMS}$	4.07	4.02	4.14	4.08	4.08	4.05
	$\mathcal{E}_P^{MAX}$	0.75	0.75	0.72	0.80	0.74	0.73
	$\mathcal{E}_Q^{MAX}$	3.58	3.54	3.53	3.28	3.53	1.48
	$\mathcal{E}_{\Delta r}^{MAX}$	6.86	6.76	6.89	6.95	6.85	6.98
	$\mathcal{E}_P^{SYS}$	-0.69	-0.70	-0.69	-0.72	-0.70	-0.69
	$\mathcal{E}_Q^{SYS}$	-3.52	-3.53	-3.52	-3.26	-3.52	-1.08
	$\mathcal{E}_{\Delta r}^{SYS}$	-6.81	-6.73	-6.87	-6.88	-6.83	-6.90
	$\mathcal{E}_P^{DIAS}$	0.53	0.55	0.53	0.57	0.54	0.53
	$\mathcal{E}_Q^{DIAS}$	1.76	1.78	1.76	1.74	1.77	0.69
	$\mathcal{E}_{\Delta r}^{DIAS}$	-1.95	-1.92	-2.02	-1.89	-1.94	-1.88
Midpoint iliac	$\mathcal{E}_P^{RMS}$	0.45	0.45	0.44	0.47	0.45	0.44
	$\mathcal{E}_Q^{RMS}$	0.89	0.66	0.65	0.68	0.67	0.66
	$\mathcal{E}_{\Delta r}^{RMS}$	4.29	4.30	4.35	4.31	4.31	4.26
	$\mathcal{E}_P^{MAX}$	0.82	0.86	0.84	0.92	0.86	0.85
	$\mathcal{E}_Q^{MAX}$	2.25	2.00	2.01	1.80	2.01	2.02
	$\mathcal{E}_{\Delta r}^{MAX}$	7.25	7.36	7.37	7.48	7.35	7.34
	$\mathcal{E}_P^{SYS}$	-0.81	-0.83	-0.81	-0.85	-0.82	-0.81
	$\mathcal{E}_Q^{SYS}$	-1.80	-1.84	-1.81	-1.58	-1.89	-1.79
	$\mathcal{E}_{\Delta r}^{SYS}$	-7.22	-7.26	-7.27	-7.31	-7.25	-7.22
	$\mathcal{E}_P^{DIAS}$	0.53	0.55	0.54	0.57	0.54	0.54
	$\mathcal{E}_Q^{DIAS}$	1.17	1.19	1.17	1.18	1.19	1.18
	$\mathcal{E}_{\Delta r}^{DIAS}$	-2.38	-2.37	-2.45	-2.35	-2.38	-2.41

Table 36: Relative errors (in %) as defined in Section 3.8 for the six numerical schemes at three points of the aortic bifurcation: midpoint of the aorta (top), end point of the aorta (middle), and midpoint of either iliac artery (bottom).

Arterial segment	Numerical scheme	$\mathcal{E}_P^{RMS}$ (%)	$\mathcal{E}_P^{MAX}$ (%)	$\mathcal{E}_P^{SYS}$ (%)	$\mathcal{E}_P^{DIAS}$ (%)	$\mathcal{E}_Q^{RMS}$ (%)	$\mathcal{E}_Q^{MAX}$ (%)	$\mathcal{E}_Q^{SYS}$ (%)	$\mathcal{E}_Q^{DIAS}$ (%)
Aortic arch II	DG	1.78	3.59	-1.40	-0.42	12.32	29.58	8.78	-17.95
	LCG	1.68	3.21	-1.02	-0.93	12.34	31.83	10.02	-16.93
	FEM	1.89	3.78	-1.40	-0.17	12.02	29.00	8.81	-17.08
	FVM	1.87	3.72	-1.46	-0.30	12.11	29.13	8.75	-17.93
	McC	1.94	3.97	-1.60	-0.12	12.11	29.40	8.81	-17.74
	STM	1.84	3.76	-1.39	-0.36	12.19	29.45	8.75	-17.99
Thoracic aorta II	DG	2.36	5.29	-0.96	1.66	25.59	67.52	60.70	-39.65
	LCG	2.17	5.03	-0.79	1.13	25.36	70.75	61.59	-35.47
	FEM	2.49	5.66	-0.97	1.97	25.26	64.93	60.39	-38.29
	FVM	2.44	5.57	-1.03	1.81	25.43	65.69	61.59	-39.26
	McC	2.53	5.70	-1.13	1.98	25.62	66.22	62.24	-38.74
	STM	2.42	5.58	-0.98	1.69	25.37	65.32	61.16	-38.77
Left subclavian I	DG	3.09	6.13	-3.92	-3.97	14.31	38.39	-2.11	-11.57
	LCG	3.12	6.06	-3.38	-4.63	13.87	34.76	-2.92	-11.33
	FEM	3.05	6.10	-3.91	-3.72	14.17	37.89	-2.53	-10.86
	FVM	3.12	6.29	-3.96	-3.93	14.24	38.12	-2.25	-11.05
	McC	3.11	6.35	-4.09	-3.69	14.31	38.25	-2.08	-10.92
	STM	3.11	6.13	-3.80	-3.97	14.45	38.96	-1.18	-10.83
R. iliac-femoral II	DG	3.82	9.00	-2.20	-4.13	24.49	59.63	50.20	-39.72
	LCG	3.97	9.69	-2.19	-5.57	24.17	61.14	49.23	-36.92
	FEM	3.69	8.66	-2.32	-3.67	23.90	59.28	49.99	-37.18
	FVM	3.75	9.09	-2.26	-4.04	24.19	60.61	51.42	-39.06
	McC	3.65	8.95	-2.33	-3.73	24.80	61.61	52.41	-40.21
	STM	3.75	9.32	-2.37	-4.17	24.12	60.41	51.29	-38.26
Left ulnar	DG	2.65	7.19	-0.99	-2.68	12.74	30.14	5.37	-17.48
	LCG	2.57	6.51	-1.45	-3.54	12.42	25.91	4.30	-17.93
	FEM	2.70	7.29	-1.13	-2.34	12.43	27.75	3.63	-16.14
	FVM	2.74	7.51	-1.09	-2.54	12.70	29.30	4.60	-17.15
	McC	2.75	7.42	-1.07	-2.27	12.78	29.19	4.43	-16.80
	STM	2.74	7.46	-0.81	-2.63	12.91	29.55	5.68	-17.02
R. anterior tibial	DG	3.25	9.87	0.57	-0.13	10.49	35.07	8.37	-15.09
	LCG	3.43	12.24	0.57	-0.80	11.05	35.80	12.37	-14.59
	FEM	3.21	9.12	0.55	0.04	9.88	31.16	8.40	-13.25
	FVM	3.30	9.42	0.66	-0.14	10.22	33.57	9.79	-14.75
	McC	3.41	10.33	0.89	0.03	10.24	34.38	9.76	-14.43
	STM	3.27	9.22	0.72	-0.15	10.24	34.54	10.32	-14.07
Right ulnar	DG	2.54	6.32	-2.18	-3.91	11.67	31.30	16.89	-3.47
	LCG	2.58	6.88	-1.92	-4.33	11.47	28.19	17.56	-7.48
	FEM	2.66	6.36	-2.55	-3.96	11.22	29.28	15.77	-4.08
	FVM	2.49	6.32	-2.20	-3.92	11.62	30.93	16.50	-4.60
	McC	2.42	6.06	-2.15	-3.66	11.63	31.09	16.58	-4.39
	STM	2.50	6.50	-2.06	-4.09	11.73	31.58	17.40	-5.34

Table 37: Relative pressure and flow errors (in %) in the 37-artery network with available *in vitro* data.

D.2 figures

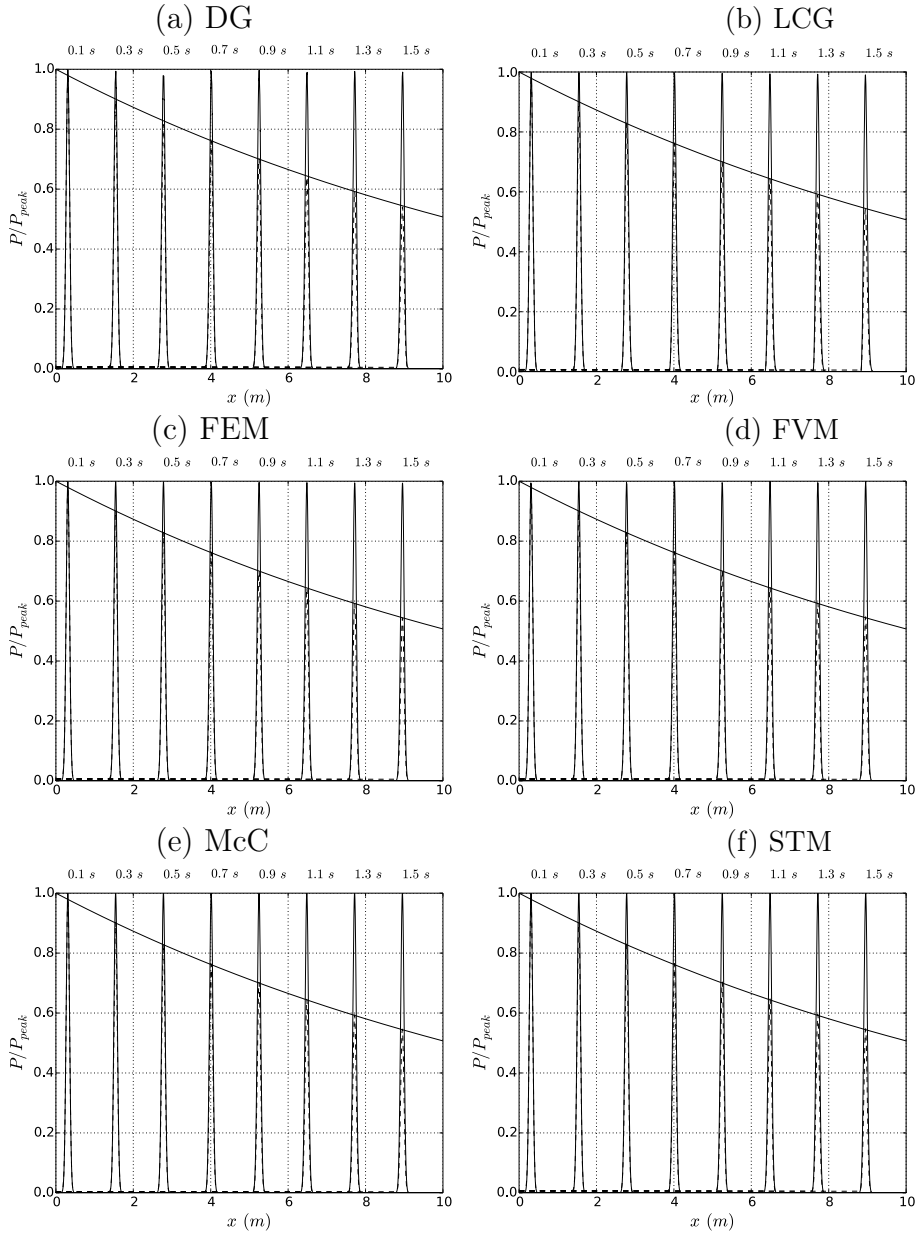

Figure 34: Single pulse. Pressure (P) with distance for the six numerical schemes at the times indicated by the labels in a 10 m long vessel with a completely absorbent outlet. They are produced by a narrow Gaussian-shaped wave propagating from the inlet of the vessel with a peak volume inflow rate of 1 ml s^{-1}. The model parameters are shown in Table 1. Two cases are shown: inviscid blood (thin solid lines) and viscous blood (dashed lines). For the viscous case, the theoretical solution given by Eq. (67) corresponds to the thick black line. Pressures are non-dimensionalised by the peak value of the inflow pressure (P_{peak}).

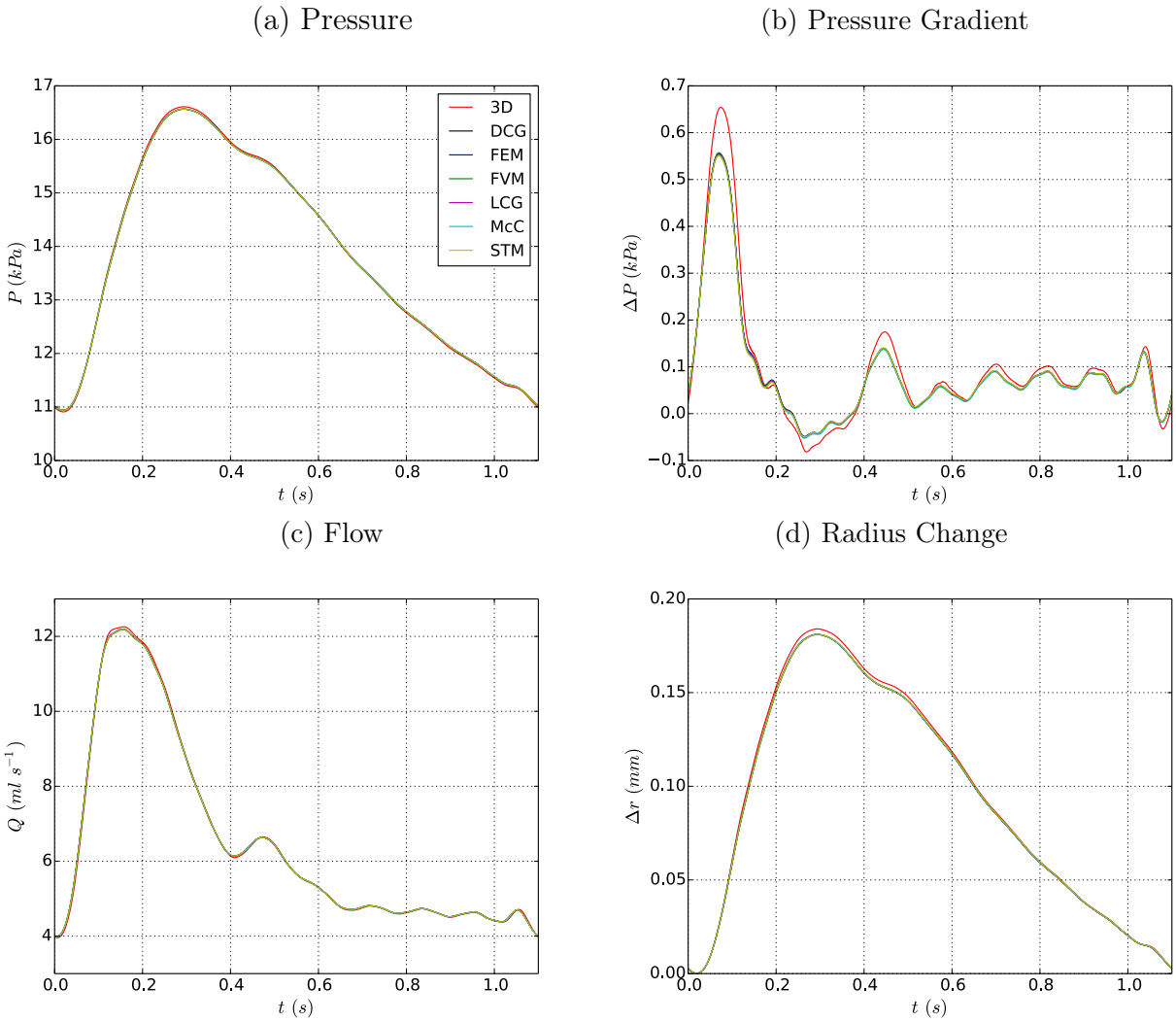

Figure 35: Common carotid artery. Pressure (a), pressure gradient between inlet and outlet (b), flow rate (c), and change in radius from diastole (d) with time at the midpoint of the vessel. Results are shown for the six 1-D numerical schemes and the 3-D model from [57]. The model parameters are shown in Table 2 and the error calculations in Table 34.

(a) Pressure

(b) Pressure Gradient

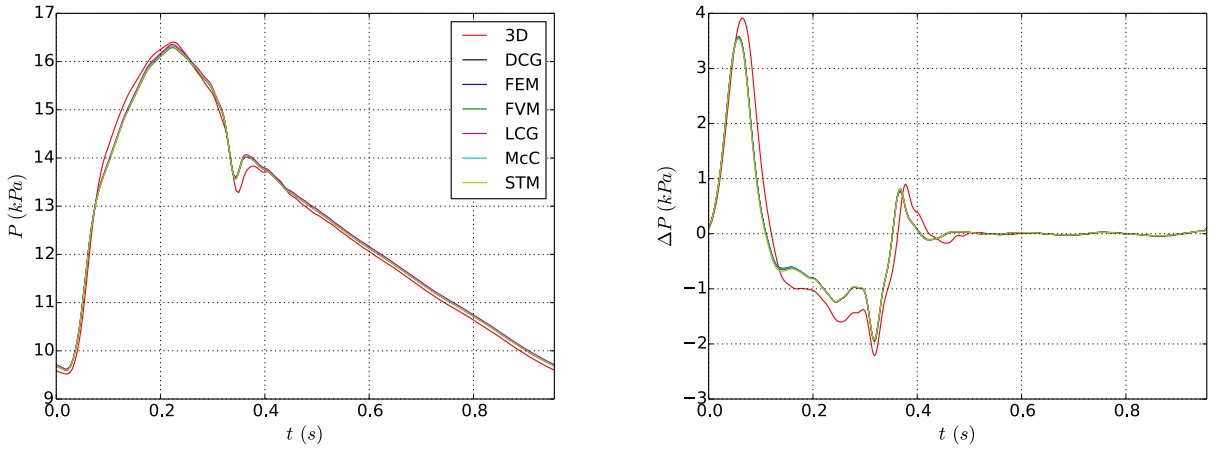

(c) Flow

(d) Radius Change

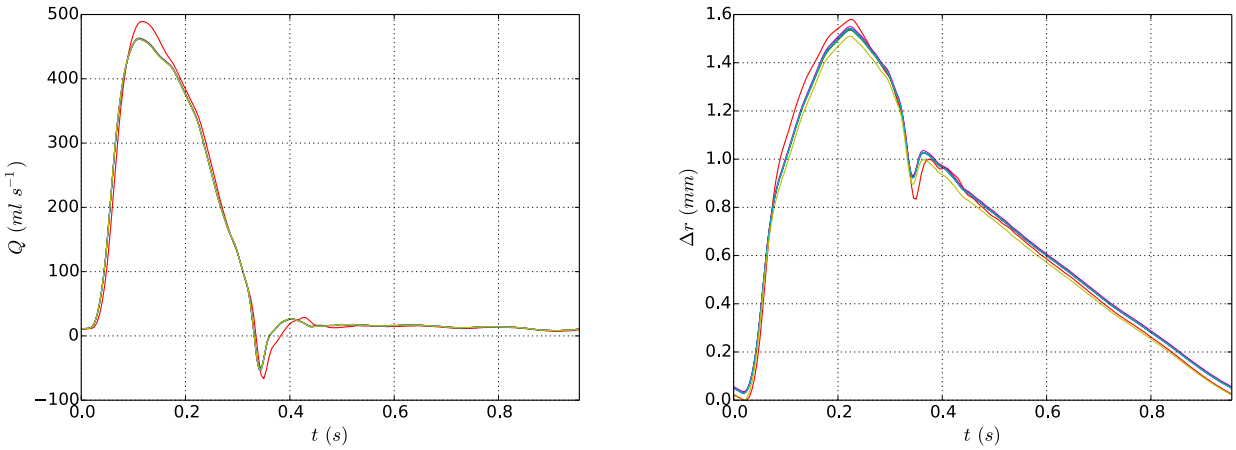

Figure 36: Upper thoracic aorta. Pressure (a), pressure gradient between inlet and outlet (b), flow rate (c), and change in radius from diastole (d) with time at the midpoint of the vessel. Results are shown for the six 1-D numerical schemes and the 3-D model from [57]. The model parameters are shown in Table 3 and the error calculations in Table 35.

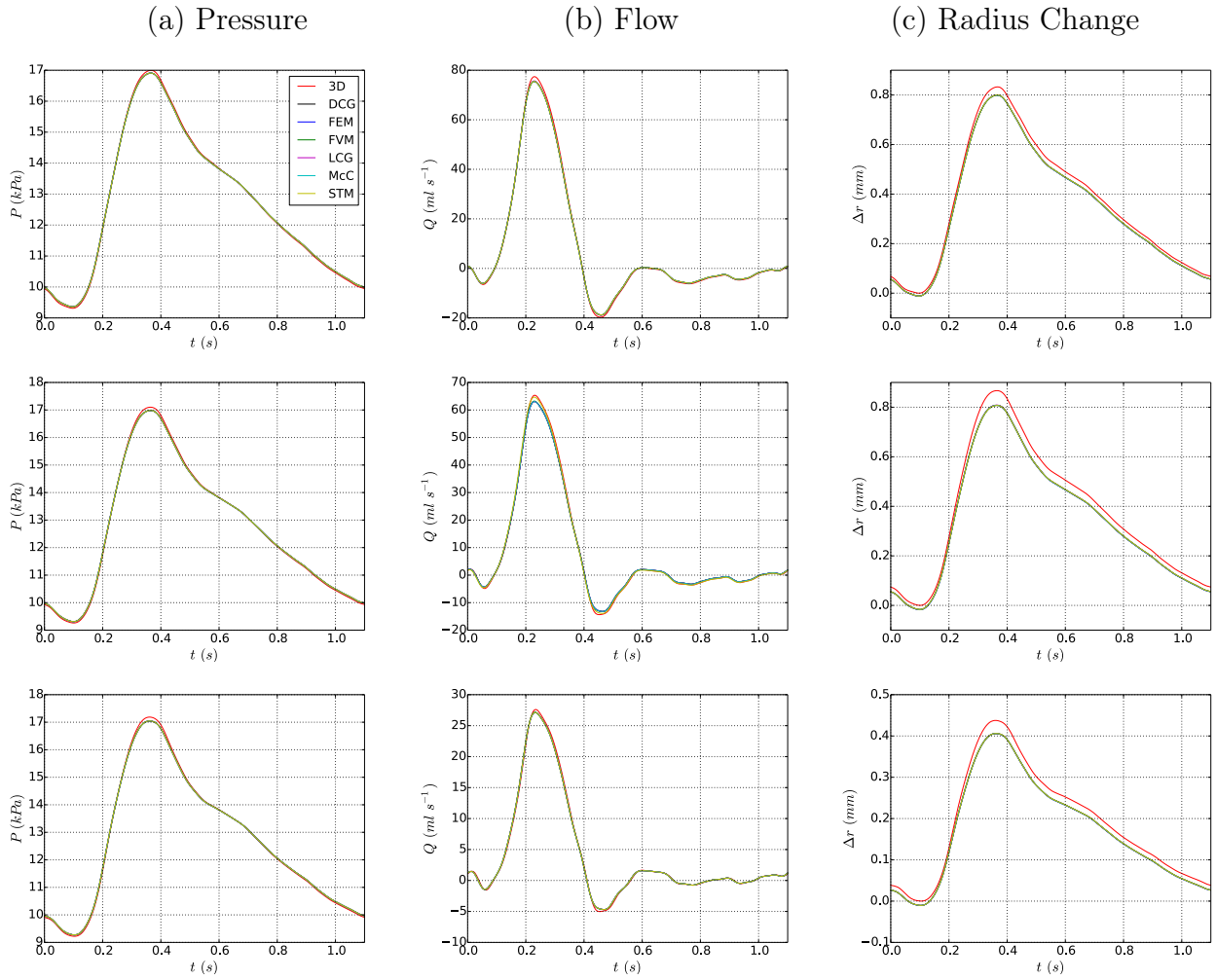

Figure 37: Aortic bifurcation. Pressure (a), flow rate (b), and change in radius from diastole (c) at the midpoint of the aorta (top), end point of the aorta (middle) and midpoint of either iliac artery (bottom). Results are shown for the six 1-D numerical schemes and the 3-D model from [57]. The model parameters are shown in Table 4 and the error calculations in Table 5.

(a) Aortic Arch

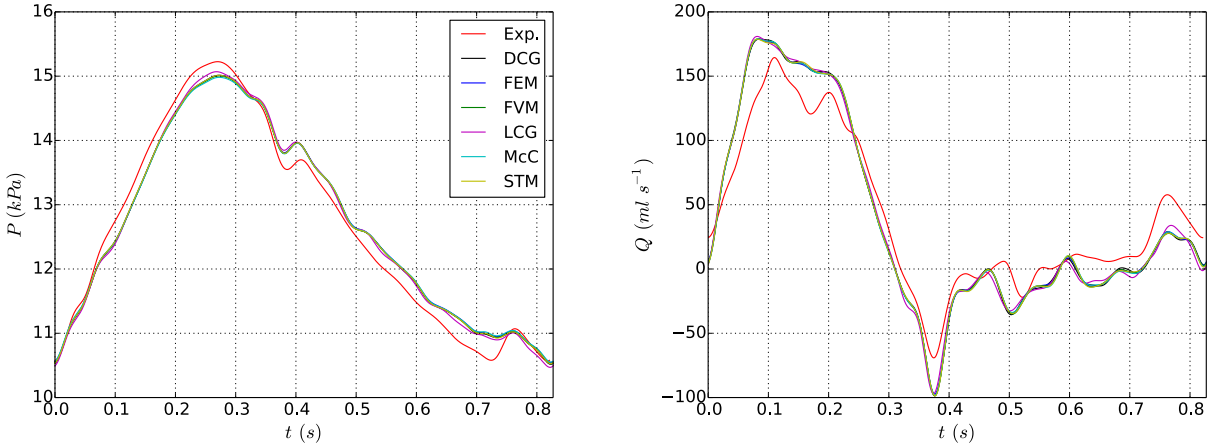

(b) Thoracic Aorta

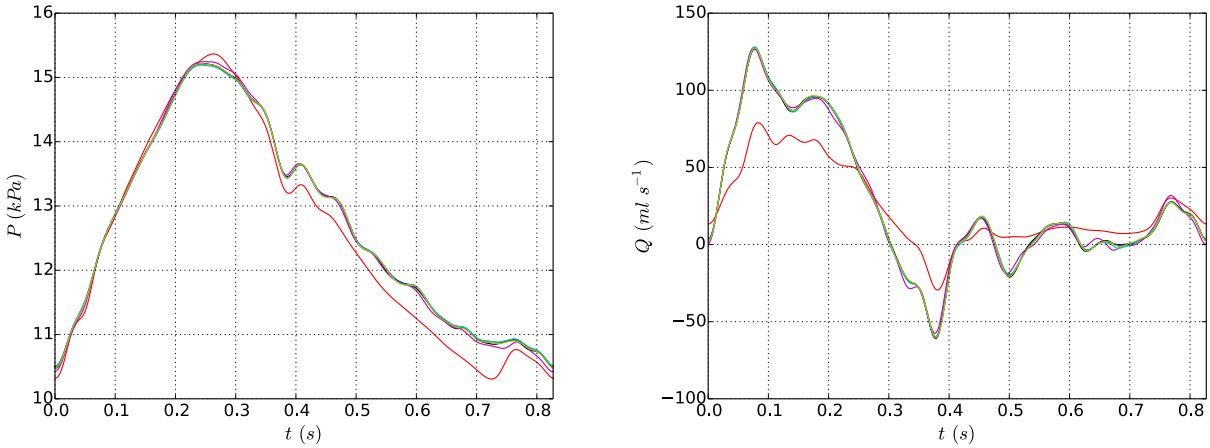

Figure 38: 37-artery network. Pressure (left) and flow (right) waveforms in the midpoint of two aortic segments: (a) aortic arch II and (b) thoracic aorta II. Results are shown for the six 1-D numerical schemes and the *in vitro* data (Exp.) measured in [26]. General model parameters are shown in Table 5.

(a) Left Subclavian

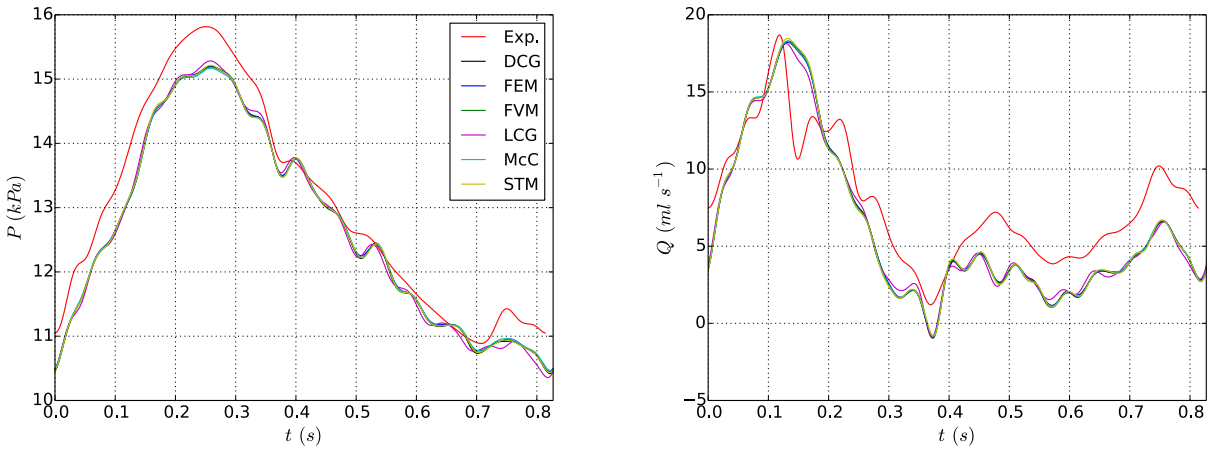

(b) Right Iliac-Femoral

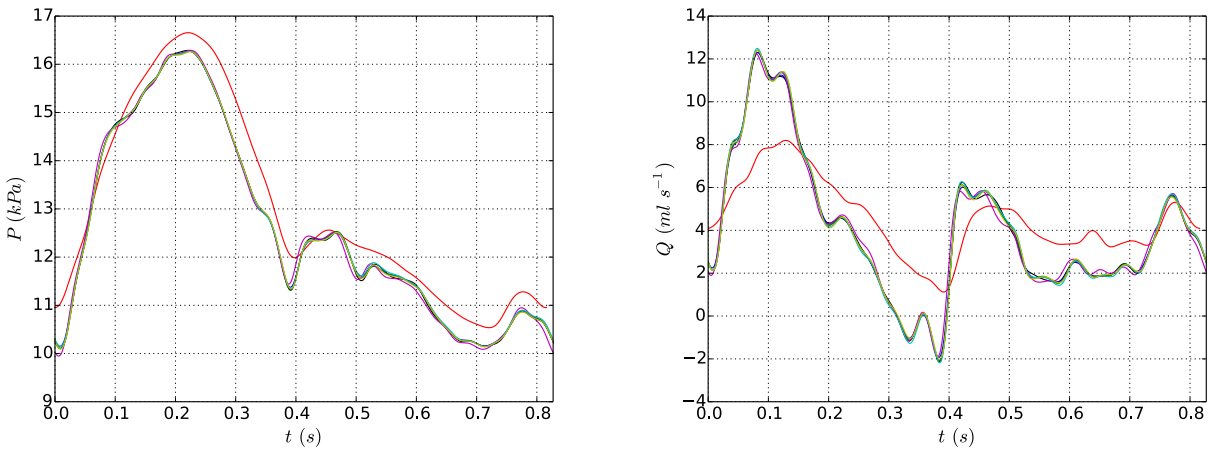

Figure 39: 37-artery network. Pressure (left) and flow (right) waveforms in the midpoint of two vessels from the first generation of bifurcations: (a) left subclavian I and (b) right iliac-femoral II. Results are shown for the six 1-D numerical schemes and the *in vitro* data (Exp.) measured in [26]. General model parameters are shown in Table 5.

(a) Left Ulnar

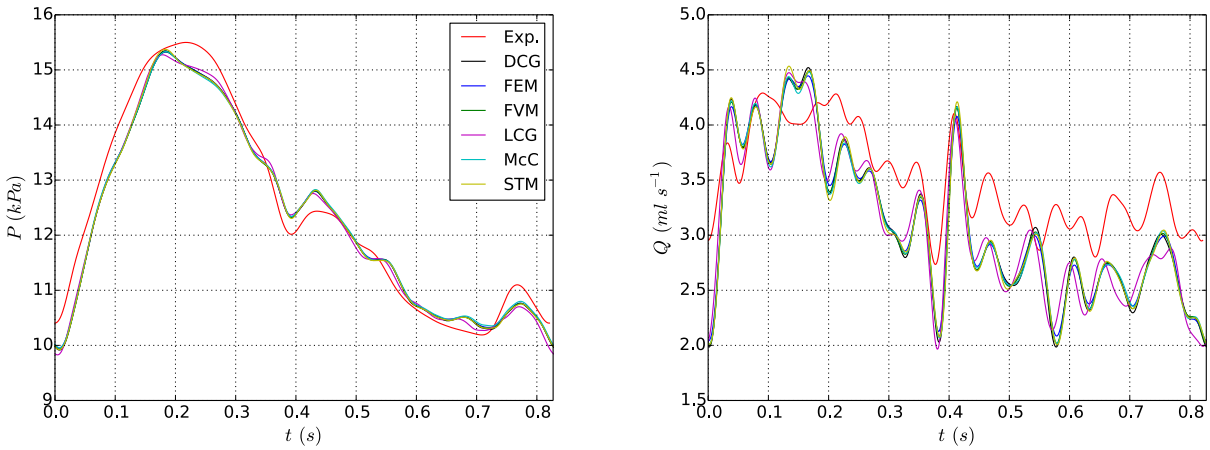

(b) Right Anterior Tibial

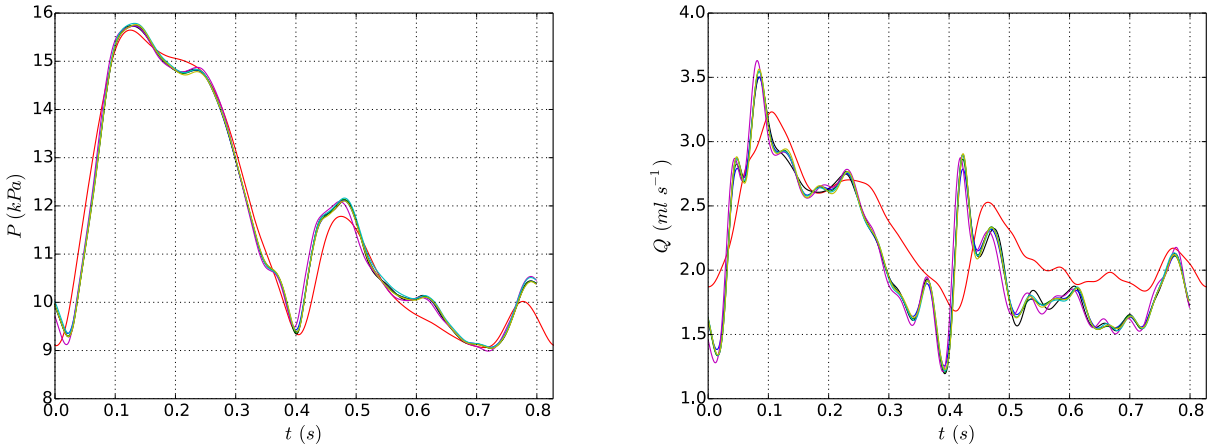

Figure 40: 37-artery network. Pressure (left) and flow (right) waveforms in the midpoint of two vessels from the second generation of bifurcations: (a) left ulnar and (b) right anterior tibial. Results are shown for the six 1-D numerical schemes and the *in vitro* data (Exp.) measured in [26]. General model parameters are shown in Table 5.

(a) Right Ulnar

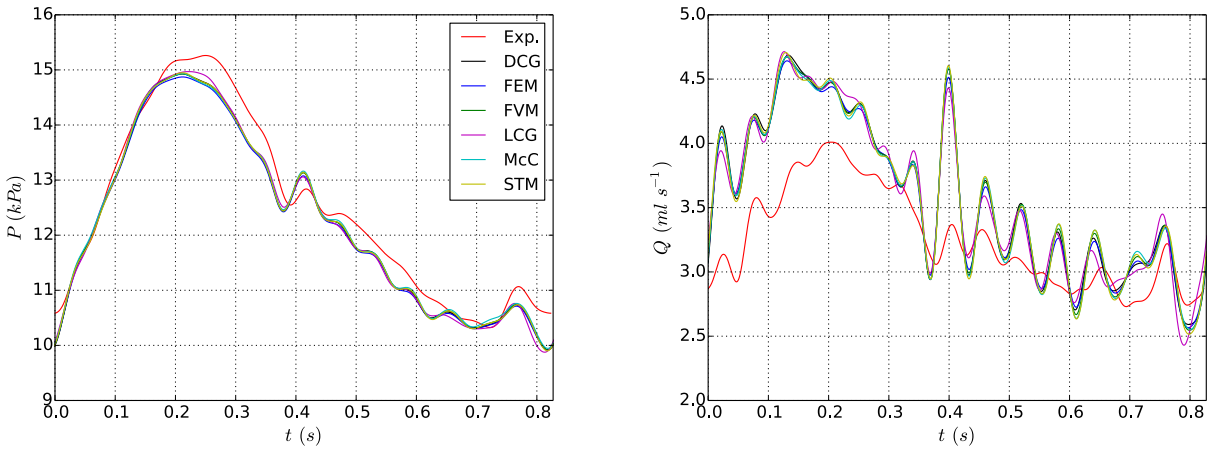

(b) Splenic

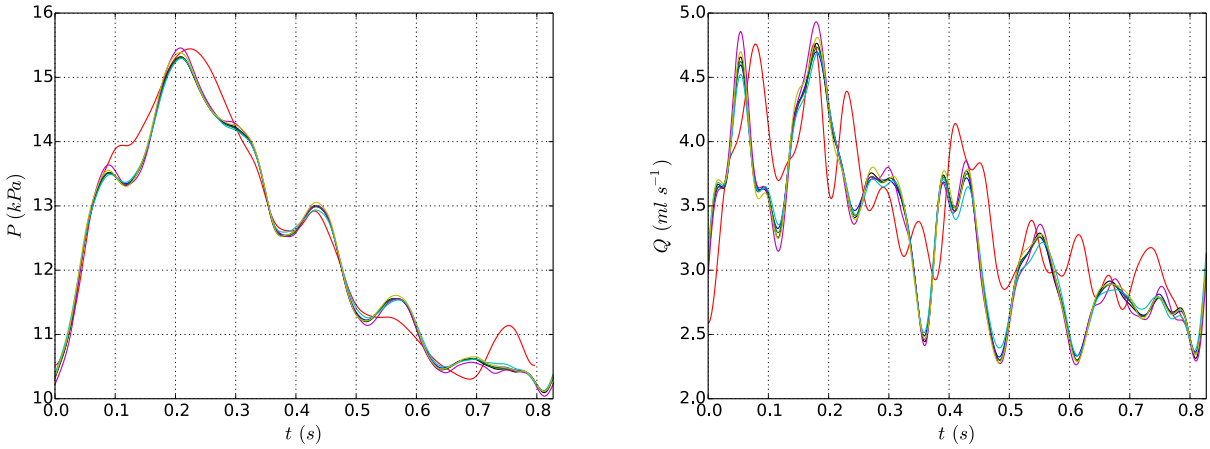

Figure 41: 37-artery network. Pressure (left) and flow (right) waveforms in the midpoint of two vessels from the third generation of bifurcations: (a) right ulnar and (b) splenic. Results are shown for the six 1-D numerical schemes and the *in vitro* data (Exp.) measured in [26]. General model parameters are shown in Table 5.

(a) Aortic Arch

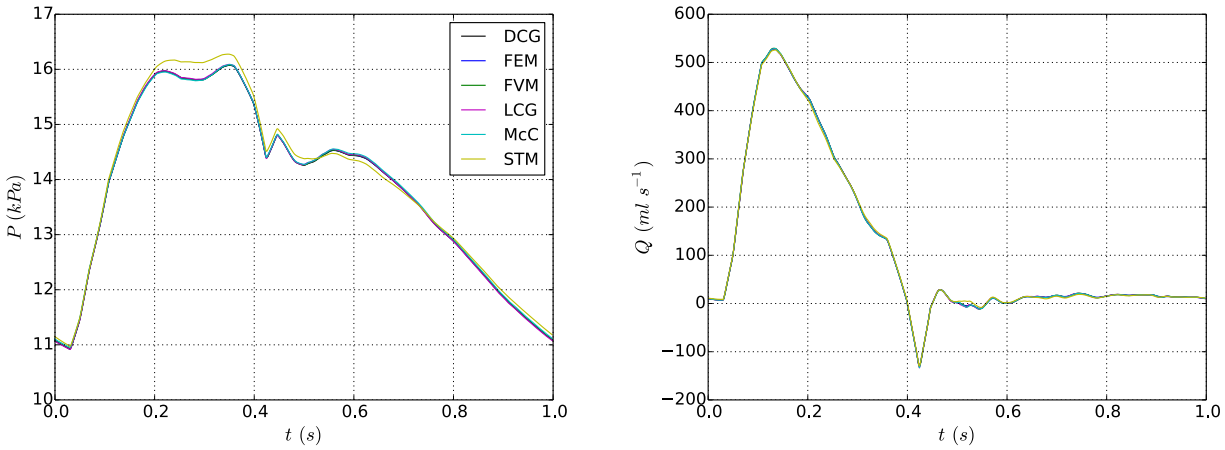

(b) Thoracic Aorta

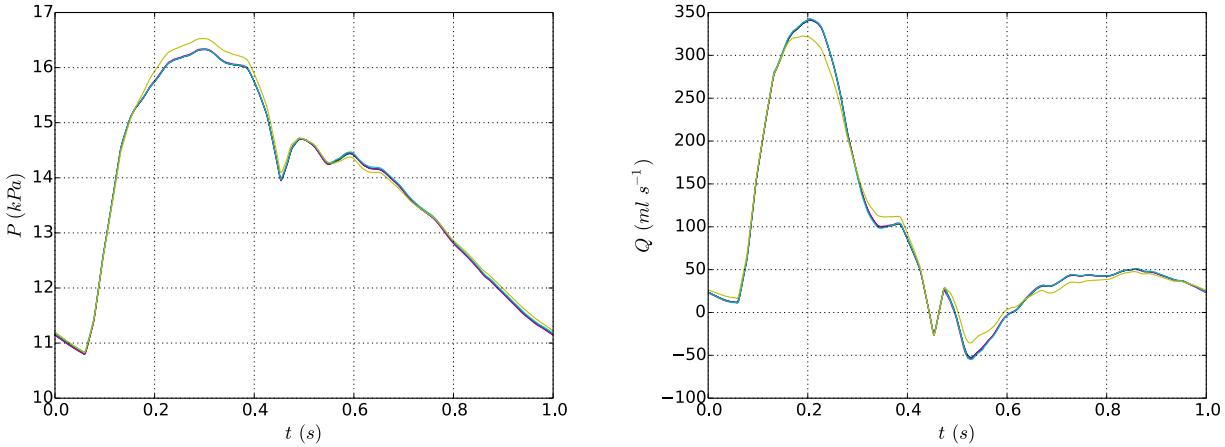

(c) Abdominal Aorta

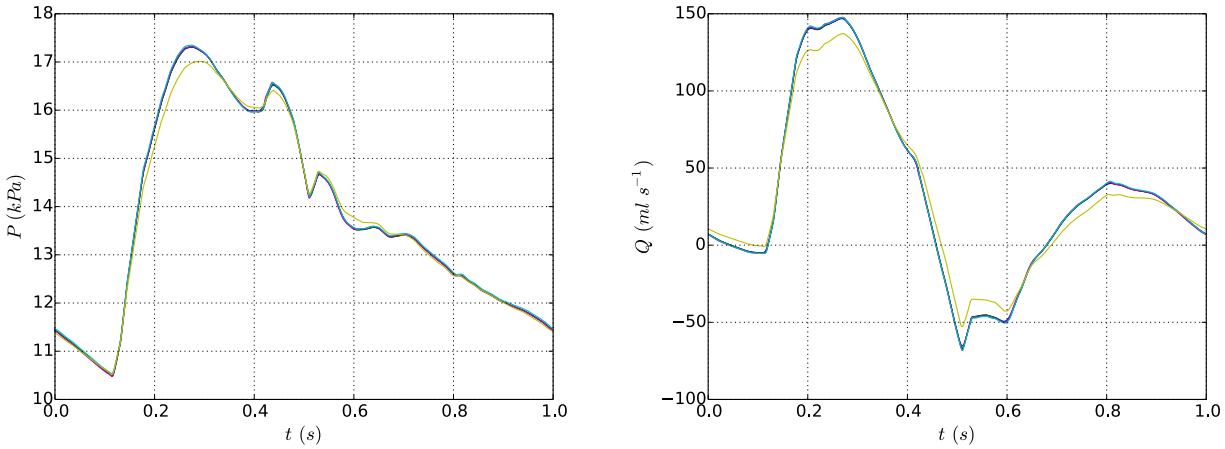

Figure 42: ADAN55 model. Pressure (left) and flow (right) waveforms in the midpoint of three aortic segments: (a) aortic arch I, (b) thoracic aorta III and (c) abdominal aorta V. Results are shown for the six 1-D numerical schemes. General model parameters are shown in Table 6.

(a) Right Common Carotid

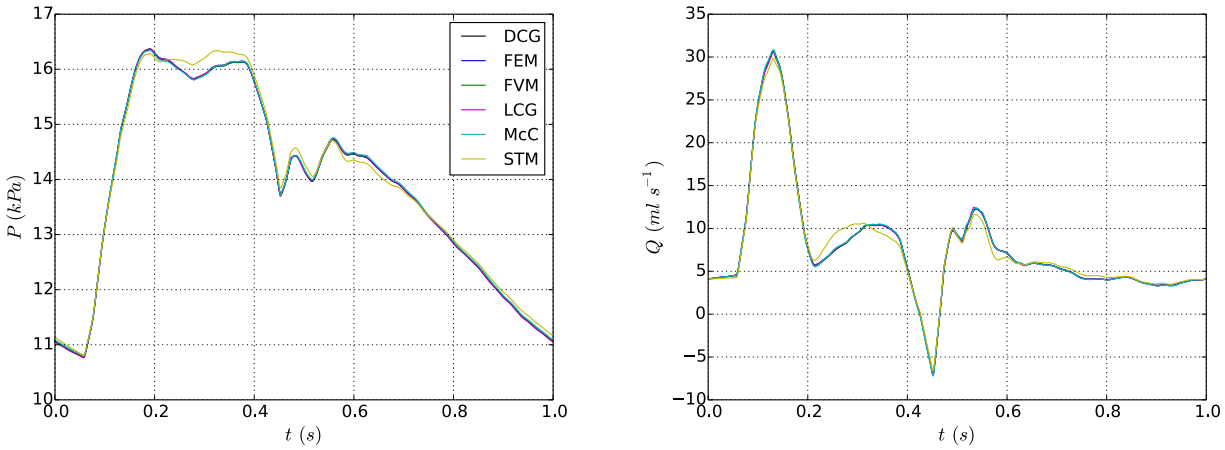

(b) Right Renal

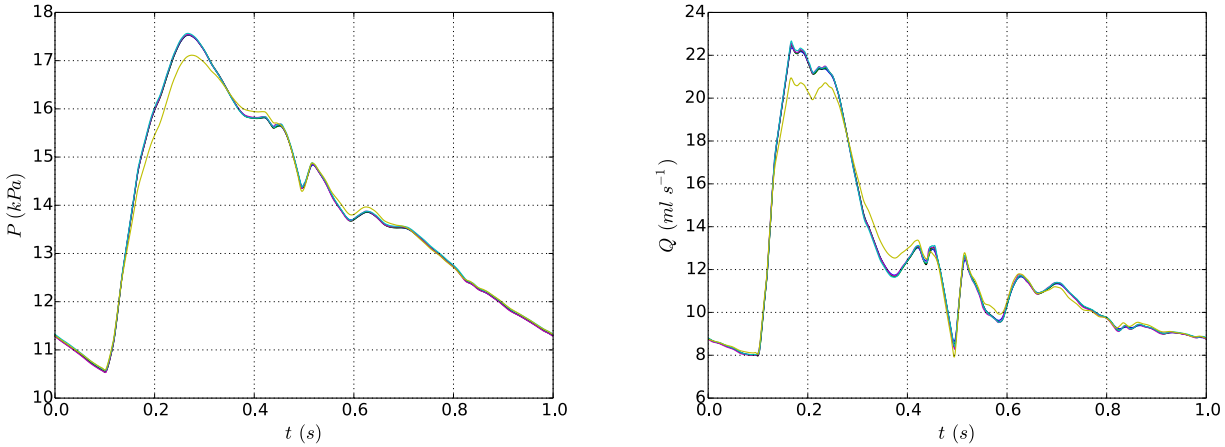

(c) Right Common Iliac

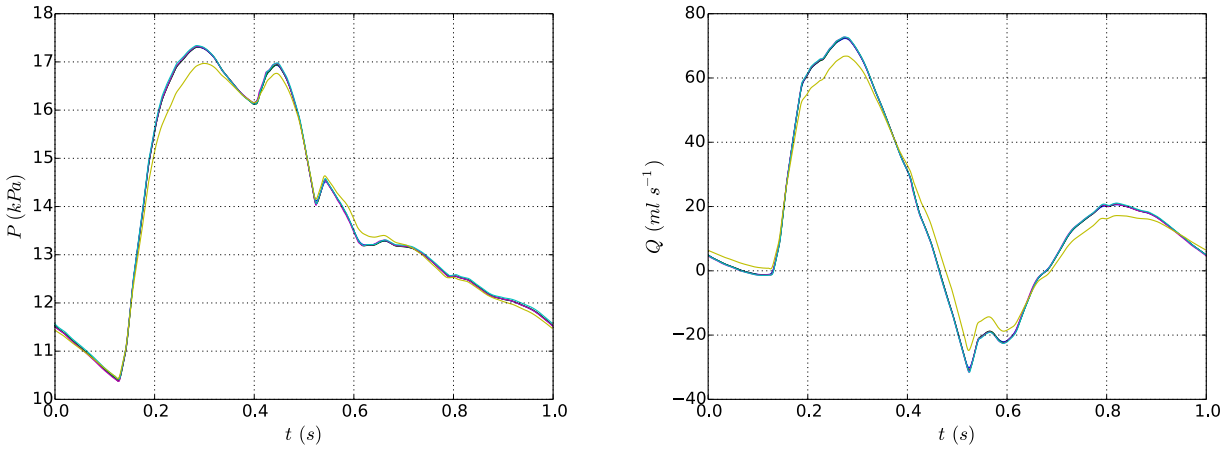

Figure 43: ADAN55 model. Pressure (left) and flow (right) waveforms in the midpoint of three vessels from the first generation of bifurcations: (a) right common carotid, (b) right renal and (c) right common iliac. Results are shown for the six 1-D numerical schemes. General model parameters are shown in Table 6.

(a) Right Internal Carotid

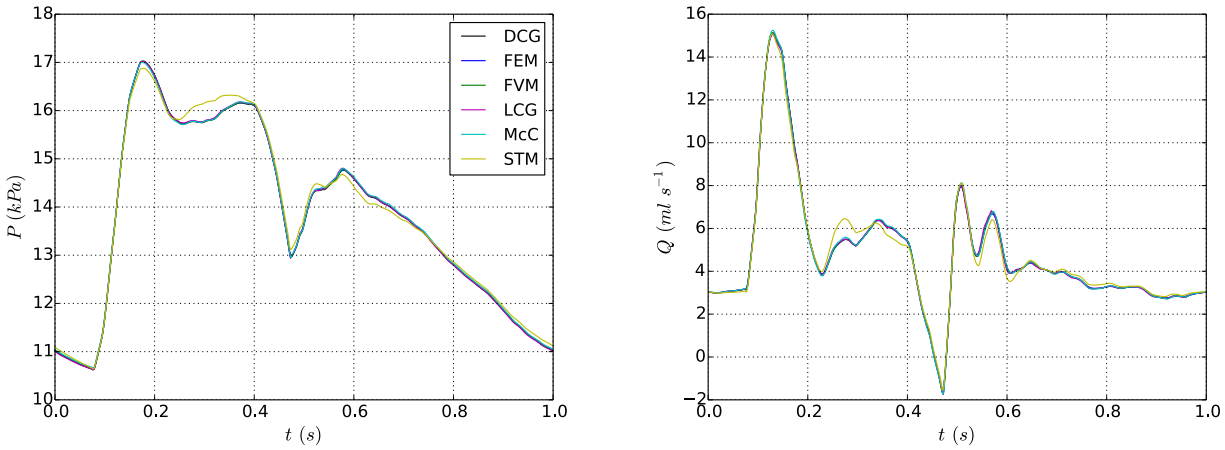

(b) Right Radial

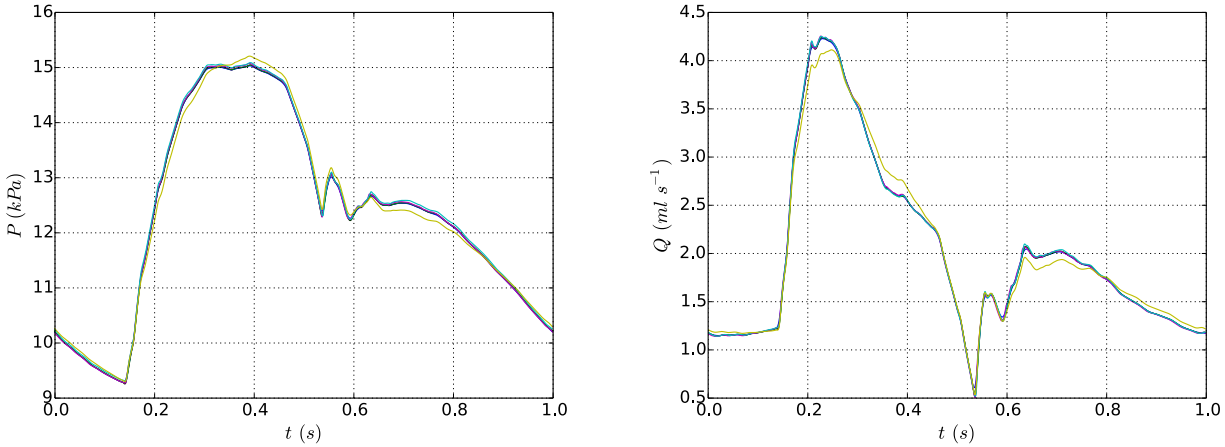

(c) Right Internal Iliac

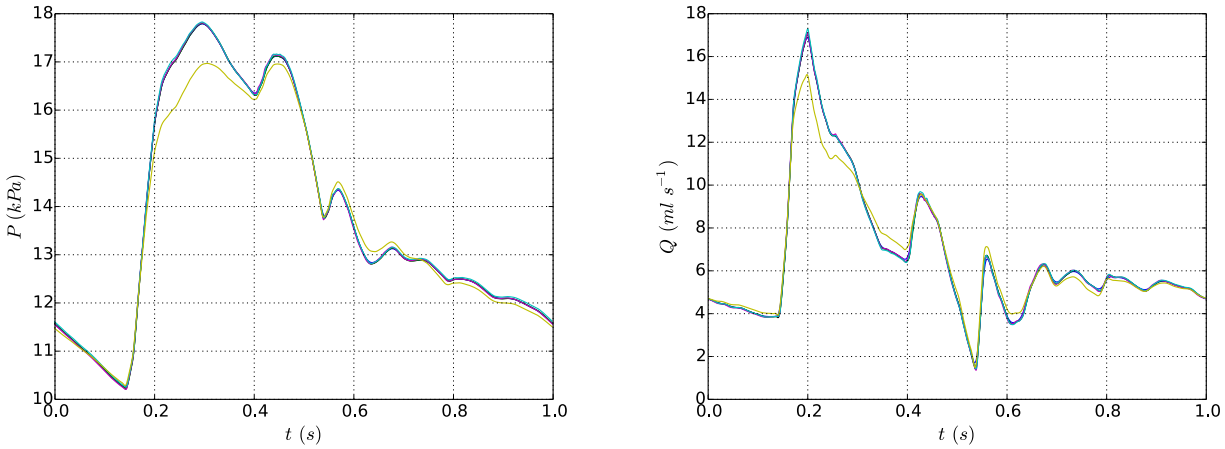

Figure 44: ADAN55 model. Pressure (left) and flow (right) waveforms in the midpoint of three vessels from the second generation of bifurcations: (a) right internal carotid, (b) right radial and (c) right internal iliac. Results are shown for the six 1-D numerical schemes. General model parameters are shown in Table 6.

(a) Right Posterior Interosseous

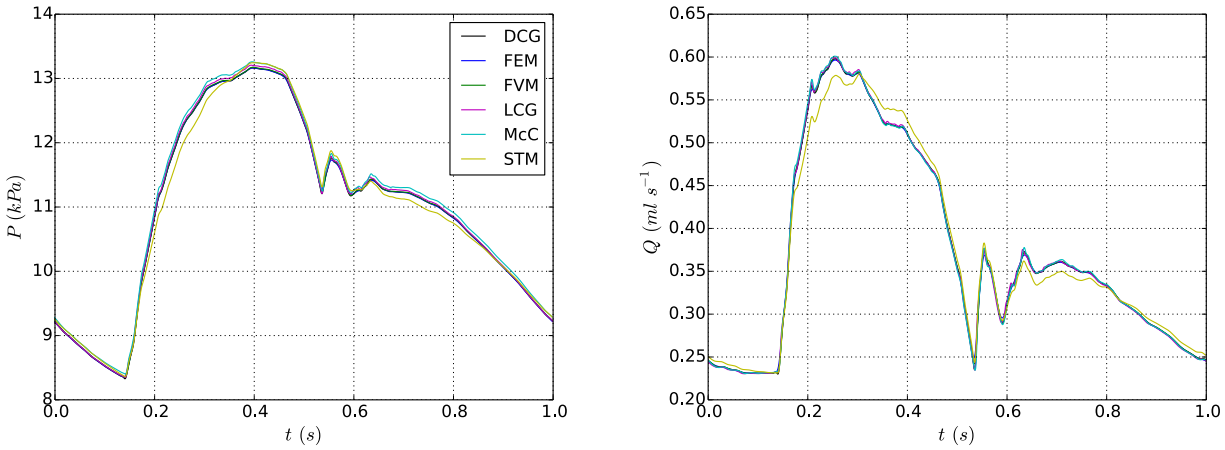

(b) Right Femoral

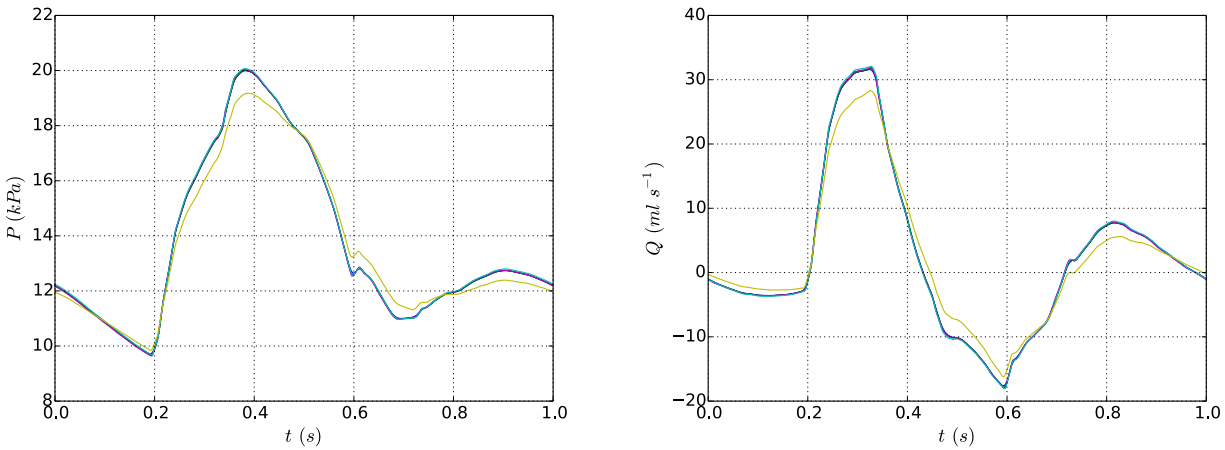

(c) Right Anterior Tibial

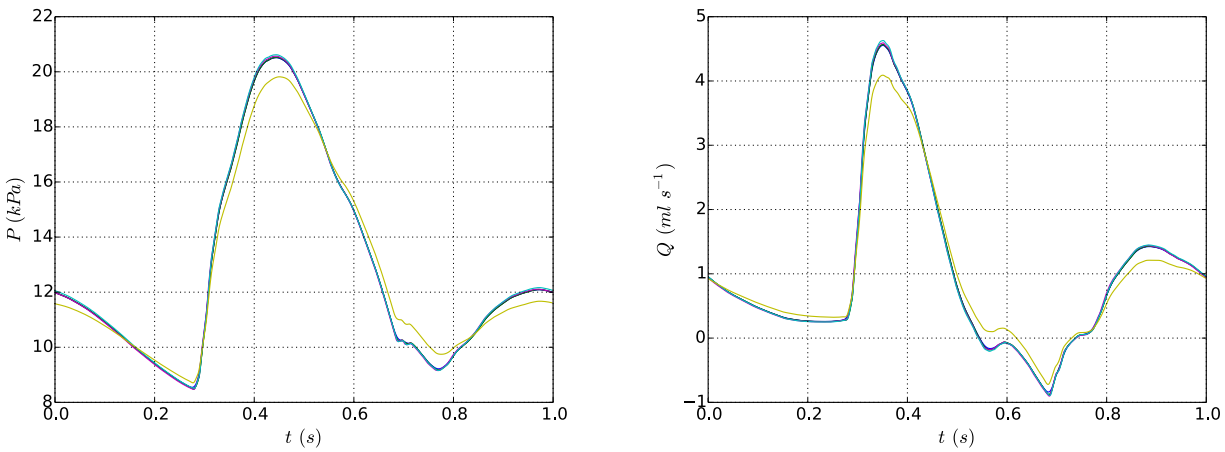

Figure 45: ADAN55 model. Pressure (left) and flow (right) waveforms in the midpoint of three vessels from the third and fourth generation of bifurcations: (a) right posterior interosseous, (b) right femoral and (c) right anterior tibial. Results are shown for the six 1-D numerical schemes. General model parameters are shown in Table 6.

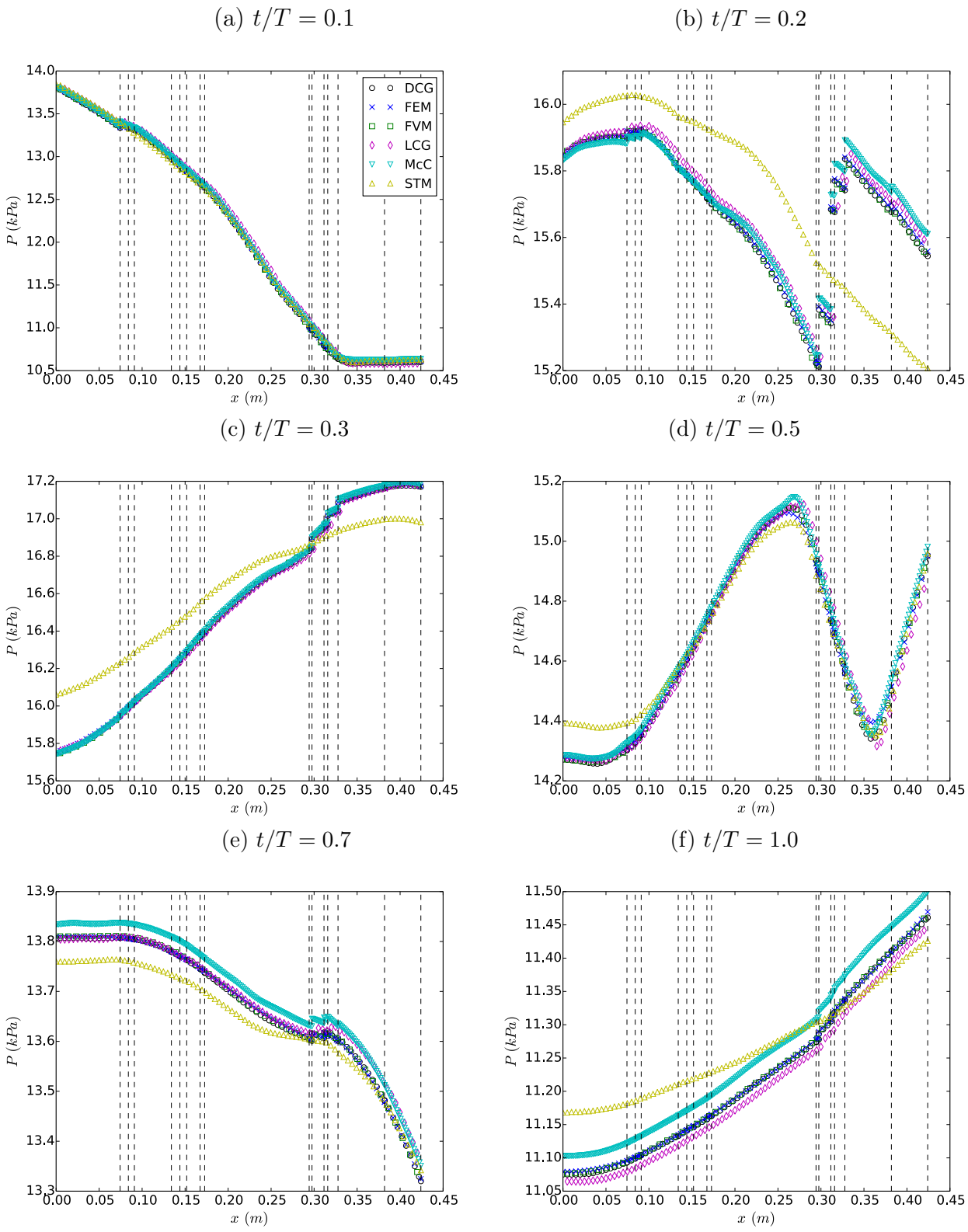

Figure 46: ADAN55 model. Pressure contour along the aorta at several time instants during the cardiac cycle, relative to the cardiac period T.

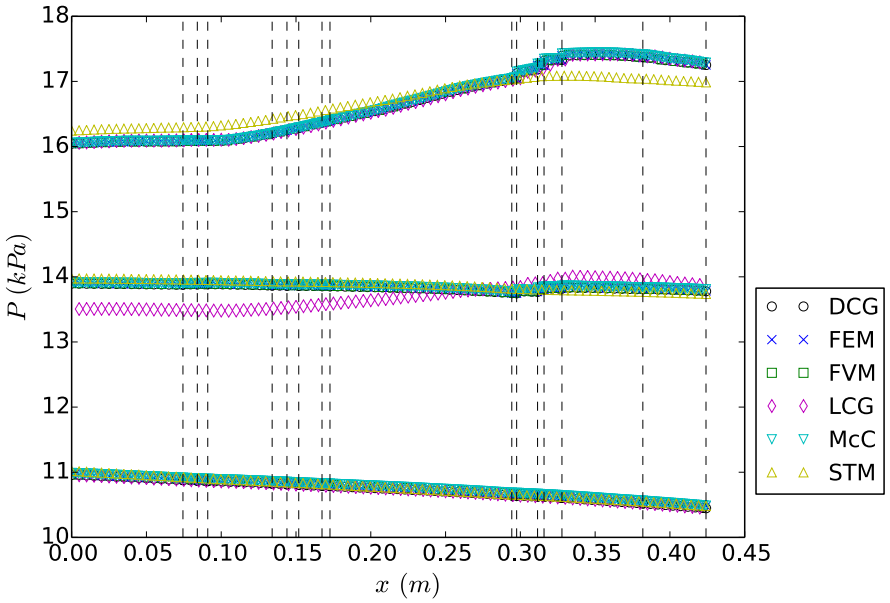

Figure 47: ADAN55 model. Systolic, mean and diastolic pressure along the aorta.

E Additional mathematics

E.1 Analytical solution for steady flow through Bifurcation with Resistance BC

Here I present the Analytical solution used in Sect. 7.1.8. The governing equations of the Bifurcation with constant flow, and distal single Resistance boundary conditions are repeated below:

$$\begin{aligned} f_1 &= Q_m - Q_r - Q_l = 0 \\ f_2 &= P_l - P_m + \frac{\rho}{2}\left(U_l^2 - U_m^2\right) \\ f_3 &= P_r - P_m + \frac{\rho}{2}\left(U_r^2 - U_m^2\right) \\ f_4 &= P_l - Q_l R_l \\ f_5 &= P_r - Q_r R_r \end{aligned}$$

The Nonlinear equations were solved for each time step by the Newton-Raphson method given by:

$$\boldsymbol{x_{i+1}} = \boldsymbol{x_i} - (\boldsymbol{J_i})^{-1} f_i$$

where J is the Jacobi Matrix:

$$J_{jk} = \frac{\partial f_j}{\partial x_k}$$

where $\boldsymbol{x} = [x_1, x_2, x_3, x_4, x_4] = [P_m, P_l, Q_l, P_r, Q_r]$, $\boldsymbol{f} = [f_1, f_2, f_3, f_4, , f_5]$, $J_{jk} = \frac{\partial f_j}{\partial x_k}$, $j = 1, 2, 3, 4, 5, k = 1, 2, 3, 4, 5$. Performing the differentiations lead to the following Jacobi, and inverse Jacobi matrices:

$$\mathbf{J} = \begin{bmatrix} 0 & 0 & -1 & 0 & -1 \\ 1 & -1 & a & 0 & 0 \\ 1 & 0 & 0 & -1 & b \\ 0 & 1 & c & 0 & 0 \\ 0 & 0 & 0 & 1 & d \end{bmatrix}, \quad \mathbf{J^{-1}} = \begin{bmatrix} (a+c)(b+c) & (d+c) & (c+a) & (b+d) & (c+a) \\ c(d+b) & -c & c & (a+b+d) & c \\ -(d+b) & 1 & -1 & 1 & -1 \\ d(c+a) & d & -d & d & (c+a+b) \\ -(a+c) & -1 & 1 & -1 & 1 \end{bmatrix} \frac{1}{Det}.$$

where

$$a = \frac{-\rho Q_l}{A_l^2}$$
$$b = \frac{-\rho Q_l}{A_r^l}$$
$$c = -R_l$$
$$d = -R_l$$
$$Det = a + b + c + d$$